AN EXPERIMENTAL AND NUMERICAL INVESTIGATION OF IMMERSION COOLED BLUE LED COMBINED WITH YAG:Ce PHOSPHOR FOR THERMAL, ELECTRICAL AND OPTICAL PERFORMANCE

A Thesis

by

Ceren Cengiz

Submitted to the

Graduate School of Sciences and Engineering
In Partial Fulfillment of the Requirements for
the Degree of

Master of Science

in the
Department of Mechanical Engineering

Özyeğin University
May 2022

AN EXPERIMENTAL AND NUMERICAL INVESTIGATION OF IMMERSION COOLED BLUE LED COMBINED WITH YAG:Ce PHOSPHOR FOR THERMAL, ELECTRICAL AND OPTICAL PERFORMANCE

Approved by:

Professor Mehmet Arık, Advisor,
Department of Mechanical Engineering
Özyeğin University

Professor Murat Uysal
Department of Electrical and Electronics Engineering
Özyeğin University

Assistant Professor Altuğ Başol
Department of Mechanical Engineering
Özyeğin University

Associate Professor Sedat Nizamoğlu
Department of Electrical and Electronics Engineering
Koç University

Assistant Professor Ramazan Ünal
Department of Mechanical Engineering
Özyeğin University

Date Approved: 31 May 2022

To my beloved family, and my dearest friends

Thank you for your endless love, trust, and support.

ABSTRACT

At the new age of illumination, light emitting diodes (LEDs) have been proven to be the most efficient alternative to conventional light sources. Yet, in comparison to the other lighting systems, LEDs can withstand a lower maximum operating temperature while junction temperature (T_j) is among the main factors dictating their lifespan, reliability, and luminance performance. Thermal concerns in high power LEDs are important not only because of the dramatic failure of the chip, but also lowered performance in terms of light characteristics. Generated heat and increased device temperatures are direct indicators of poor performance. In fact, heat generation in LED packages occurs mainly on the chip and phosphor layers, both of which lead to a decrease in light output due to the reduction in internal and external quantum efficiencies. In addition to the heat losses over an LED die due to the losses in combination of carrier charges, optical losses are also significant. Moreover, with the increase in T_j during the operation of an LED, the transparency of optical components in the package is disrupted and leads to absorption losses. This eventually results in degradation of components in the package and performance losses. However, the highest absorption losses are observed in the LED die due to internal reflections of a portion of emitted light over the chip surface and eventually loss as heat. Although phosphor coating over LED die is a common practice, absorption losses and increased temperature of a phosphor coated layer over the die negatively affect the optical performance. Therefore, removing the phosphor layer from the die and coming up with a novel thermal package design will enhance the optical efficiency of an emission process. In addition to absorptive and reflective losses, certain losses are related to down conversion or Stokes loss of the phosphor layer in the package. During the

conversion from blue to white light, a part of light emission is lost as heat, and it affects the amount of light emission and light characteristics. Since the optical performance of LEDs is thermally limited, novel cooling techniques that also favor optical behavior are continuously investigated. Air cooling is very effective in cooling low power LEDs due to availability, low cost, and reliability, although its performance is very limited due to the low thermal capacity of air. On the other hand, the efficiency of indirect liquid cooling is an order of magnitude higher compared to air cooling; however, the cooling performance is negatively affected by additional interfaces between LED to heat sink and heat sink to air.

Direct immersion cooling of an LED chip with natural convection is found to be a promising and cost-effective solution for high power LEDs subjected to high heat fluxes. In addition, temperature uniformity of package components is achieved especially at higher driving currents that cause local temperature gradients. Moreover, in recent years, the interaction of unrestricted particles with the dispersed multi-phase flow has been linked to a number of important engineering applications. Among these applications, the novel idea of immersion cooled phosphor particles, which has the potential of significantly increasing the thermal limits of phosphor converted white LEDs (Pc-LEDs), has yet to be thoroughly investigated.

Thus, considering the above-mentioned thermal, optical, and electrical concerns with current LED devices, this thesis focused on the accurate thermal characterization of LEDs through experimental and computational measurements and proposed a novel immersion cooling technique combined with YAG:Ce to improve the performance of Pc-LED while light systems.

With this objective, first, an extensive literature review was conducted on experimental junction temperature (T_j) measurement of LEDs. For the purpose of attempting to address the governing phenomena, benefits, drawbacks, possibilities, and applications, a wide range of measurement techniques and systems are covered. The literature review section included a large number of published measurement approaches such as Temperature Sensitive Optical Parameters (TSOPs), Optical Temperature Probing, Temperature Sensitive Electrical Parameters (TSEPs), and a few other methods. Some of the corrections noted in non-ideal thermal calibration processes are discussed and presented. In addition, a summary of the experimental parameters employed in the literature is given as a reference.

Secondly, based on the outcomes of the literature review, a more accurate and time efficient forward voltage method (FVM) was studied for experimental characterization of transient and opto-thermal behavior of bare and coated LED chips under operation. For pulse duration smaller than 50 ms, pulse currents ranging from 1 to 10 mA were found to be causing an acceptable temperature rise in all short pulse durations. On the contrary, pulse currents as high as 100 mA were suggested to be avoided unless they performed in the 1 ms range. Moreover, according to the bare chip thermal characterizations and reported interrelations between output and input powers, T_j and input currents, efficiency higher than 35% cannot be achieved in useful emission power losses due to the Auger losses that significantly reduce internal quantum efficiency and interfacial thermal resistance in thermal design. Correspondingly, an immersion cooling technique that directly targets heat generation zones was suggested to increase extraction efficiency and further reduce the junction temperature.

In the experimental study, a preparation method for an immersion cooled LED package with dispersed phosphor particles was introduced. Details of the package design, step-by-step preparation, and material property specifications were explained in detail. Following that, an experimental setup that enables thermal characterization of immersion cooled LED package simultaneous to the particle velocity measurements was demonstrated. As a result, T_j and fluid temperature near the dome surface were measured to be 100 °C and 40 °C when LED has driven at 1 A current. The effectiveness of the immersion cooling technique was acknowledged by reaching lower junction temperature at higher driving currents.

In addition, image processing of particle-based investigation of phosphor has revealed that in the presence of blue light, a 10-fold increase in particle velocity can be observed. This variation was mainly attributed to the photopheresis force acting on the particle when optical effects were incorporated. The origins of this force were discussed, and alterations in particle and fluid motion due to the intense photopheresis effect were reported. The findings presented in that part aim to shed light on future studies for particle trapping and the light attraction of photoluminescence particles.

Thirdly, two-phase flow analyzes were conducted computationally by utilizing a discrete phase modeling approach in ANSYS Fluent environment. The impact of different heat generation rates of an LED package was investigated by considering natural convection currents and corresponding phosphor particle trajectories inside a fluid domain. Phosphor location and movement within a buoyancy-driven flow were further analyzed by including the self-heating effect. For that purpose, heat transfer, fluid flow, and energy paths of self-heating phosphor particles were extracted, and the influence of particle sizes was analyzed in detail. The results have shown that with immersion liquid cooling, the highest phosphor particle temperature was recorded to be under 147 °C, while larger size particles introduced higher heat transfer rates to the Pc-LED package for the same number of particles. Moreover, depending on the particle size and position, individual phosphor particles can follow a different trajectory that can affect the probability of obtaining white light emission.

ÖZETÇE

Aydınlatmanın yeni çağında, ışık yayan diyotların (LED) geleneksel ışık kaynaklarına en verimli alternatif olduğunu kanıtlamıştır. Bununla birlikte, diğer aydınlatma sistemleri ile karşılaştırıldığında, LED'ler daha düşük maksimum çalışma sıcaklığına dayanabilirken, jonksiyon sıcaklığı (T_j) LED'lerin ömrünü, güvenirliğini ve parlaklık performansını belirleyen ana faktörler arasında yer alır. Yüksek güçlü LED'lerdeki termal kaygılar, yalnızca çipin dramatik arızası nedeniyle değil, aynı zamanda ışık performansında yol açtığı düşüşler nedeniyle de kritik önem taşımaktadır. Üretilen ısı ve artan cihaz sıcaklıkları, LED'lerde düşük performansın doğrudan göstergesidir.

Isı üretimi esas olarak çip ve fosfor tabakasında meydana gelir ve her iki sıcaklık üretim noktası da iç ve dış kuantum verimliliğindeki azalma nedeniyle ışık çıkışında azalmaya neden olur. Taşıyıcı yüklerin kombinasyonu sırasında oluşan çipteki ısı kayıplarına ek olarak, optik kayıplar da önemlidir. Bir LED'in çalışması sırasında T_j'lığındaki artış ile sistem içerisindeki optik bileşenlerin şeffaflığı bozulur ve ışık soğurma kayıplarına yol açar. Bu da paketteki bileşenlerin bozulmasına ve performans kayıplarına neden olur. Bununla birlikte, yayılan ışığın bir kısmının çip yüzeyinde tekrar yansıması ile oluşan ısı, en yüksek soğurma kayıplarının LED çipinde gözlemlenmesine neden olmaktadır. Dahası, beyaz ışık elde etmek için LED kalıbı üzerine fosfor kaplama yaygın bir uygulama olmasına rağmen, kalıp üzerindeki fosfor kaplı tabakanın soğurma kayıpları ve artan sıcaklığı optik performansı ayrıca olumsuz yönde etkiler. Bu nedenle, fosfor tabakasının kalıptan çıkarılmasının ve yeni bir termal paket tasarımının geliştirilmesinin, optik verimliliği arttıracağı ön görülmektedir. Soğurucu ve yansıtıcı kayıplara ek olarak, paketteki fosfor tabakasının aşağı dönüşümü

(down conversion) ve Stokes kaybı da verimlilik düşürücü etkiye sahiptir. Maviden beyaz ışığa dönüşüm sırasında, ışık emisyonun bir kısmı ısı olarak kaybolur ve bu durum ışık emisyon miktarını ve ışık özelliklerini olumsuz etkiler.

Yukarıda da özetlendiği gibi, LED'lerin optik performansı termal olarak sınırlı olduğundan, optik verimliliği arttıracak yeni soğutma teknikleri sürekli olarak araştırılmaktadır. Hava soğutma, düşük termal kapasitesi nedeniyle performansı sınırlı olmasına rağmen, kullanılabilirlik, düşük maliyet ve güvenilirlik nedeniyle düşük güçlü LED'lerin soğutulmasında sık tercih edilmektedir. Öte yandan, dolaylı sıvı soğutmanın verimliliği, hava soğutmasına kıyasla çok daha yüksektir; fakat, soğutma performansı, LED'den ısı emiciye ve ısı emiciden hava arasındaki ek arabirimlerden ve ısıl dirençlerden olumsuz etkilenir.

Doğal konveksiyonlu bir LED çipinin doğrudan sıvı ile soğutulması, yüksek ısı akışlarına maruz kalan yüksek güçlü LED'ler için umut verici ve uygun maliyetli bir çözüm olarak bulunmuştur. Ek olarak, bu uygulama, bölgesel sıcaklık artışlarına sebep olan yüksek çalışma akımlarında bile termal homojenlik sağlanmasına olanak sağlamaktadır. Bunlara ek olarak, son yıllarda, parçacıkların akış içerisindeki dağınık etkileşimi, bir dizi önemli mühendislik uygulaması ile ilişkilendirilmiştir. Bu uygulamalar arasında, fosforla dönüştürülmüş beyaz LED'lerin (Pc-LED) termal sınırlarını önemli ölçüde artıma potansiyeline sahip olan fosfor parçacıklarının doğrudan sıvı soğutulması fikri henüz tam olarak araştırılmamıştır.

Bu nedenle, mevcut LED cihazlarıyla ilgili yukarıda bahsedilen termal, optik ve elektriksel kaygılar göz önüne alındığında, bu tez, deneysel ve hesaplamalı ölçümler yoluyla LED’lerin doğru termal karakterizasyonuna ve Pc-LED’lerin performansını artırmak için YAG:Ce ile birleştirilmiş yeni bir soğutma tekniğine odaklanmıştır.

Bu amaçla, öncelikle LED’lerin jonksiyon sıcaklığı ölçümü hakkında kapsamlı bir literatür taraması yapılmıştır. Çalışma mekanizmaları, faydaları, negatif yanları, olasılıkları ve uygulama yöntemlerini ele almak amacıyla çeşitli ölçüm teknikleri ve sistemler incelenmiştir. Literatür taraması bölümü, bu alanda yayımlanmış birçok makaleyi içermekte ve Sıcaklığa Duyarlı Optik Parametreler (TSOP’ler), Optik Yöntemlerle Sıcaklık İzlenimi, Sıcaklığa Duyarlı Elektrik Parametreler (TSEP’ler), ve diğer birkaç yöntemi kapsamaktadır. İdeal olmayan termal kalibrasyon işlemlerinde not edilen bazı düzeltmeler bu bölümde tartışılan konular arasındadır. Ayrıca literatürde kullanılan deneysel parametrelerin özetleri referans olarak verilmiştir.

İkinci olarak, literatür taraması çıkarımlarına dayanarak, çalışma altındaki kaplamasız ve kaplamalı LED çiplerinin zamana bağlı optik ve termal davranışlarının deneysel karakterizasyonu için daha doğru ve zaman açısından verimli bir ileri gerilim jonksiyon sıçaklık yöntemi geliştirilmiş ve sunulmuştur. 50 ms’den küçük sinyal süresi için, 1 ile 10 mA aralığındaki sinyal akımlarının, kabul edilebilir bir sıcaklık artışına neden olduğu bulunmuştur. Aksine, 100 mA kadar yükek sinyal akımlarından, 1 ms aralığında uygulanmadığı sürece, kaçınılması gerektiğini önerilmiştir. Ayrıca, kaplamasız LED çiplerin termal sonuçları ve giriş-çıkış güçleri, T_j ve giriş akımı arasındaki ilişkiler ele alındığında, Auger kayıplarının ve termal tasarımdaki ısıl dirençlerinin %35’ten daha yüksek verim elde edimini mümkün kılmadığı gözlemlenmiştir. Buna uygun olarak, optik verimliliği arttırmak ve jonksiyon sıcaklıklarını azaltmak için doğrudan ısı üretim bölgelerini hedef alan doğrudan sıvı soğutma tekniği önerilmiştir.

Devamında yapılan deneysel çalışmada, dağılmış fosfor parçacıkları içeren doğrudan sıvı soğutmalı LED paketi hazırlama yöntemi tanıtılmıştır. Paket tasarımının detayları, hazırlanma adımları ve malzeme özellikleri detaylı olarak anlatılmıştır. Bunu takiben, doğrudan sıvı soğutmalı LED paketinin parçacık hızı ölçümleri ile eş zamanlı olarak termal ölçümlere imkân sağlayan bir deney düzeneği kurulmuştur. Sonuç olarak, LED'in 1 A akımda sürüldüğünde T_j ve lens yüzeyine yakın sıcaklıkları 100 °C ve 40 °C olarak ölçülmüştür. Doğrudan sıvı soğutma tekniğini ile daha yüksek sürüş akımlarında daha düşük jonksiyon sıcaklıklara ulaşılarak, yöntemin etkinliği kabul edilmiştir.

Ek olarak, fosforun parçacık bazlı incelenmesi sonucunda, mavi ışık ile etkileşimi sonucu parçacıkların 10 kat daha yüksek hızlara ulaştığı gözlemlenmiştir. Bu değişim, optik etkiler dahil edildiğinde parçacık üzerinde etkili olan fotoferez kuvvetine bağlanmıştır. Bu kuvvetin ana sebepleri tartışılmış ve yoğun fotoferez etkisi nedeniyle parçacık ve sıvı hareketindeki değişiklikler not edilmiştir. Bu bölümde sunulan bulguların, parçacık takibi ve ışık yayan parçacıkların kontrolü için gelecekteki çalışmalara öncü olması amaçlanmıştır.

Üçüncü olarak, ANSYS Fluent ortamında ayrık faz modelleme yaklaşımı kullanılarak hesaplamalı olarak iki fazlı akış analizleri yapılmıştır. LED paketinin farklı ısı üretim oranlarının etkisi, doğal konveksiyon akımları ve karşılık gelen fosfor parçacık hareketleri dikkate alınarak araştırılmıştır. Doğal konveksiyon akışı içindeki fosforun konumu ve hareketi, kendi kendine ısınma etkisi dahil edilerek ayrıca analiz edilmiştir. Bu amaçla, kendiliğinden ısınan fosfor parçacıklarının ısı transferi, sıvı akışı ve enerji yolları çıkarılmış ve parçacık boyutlarının etkisi ayrıntılı olarak analiz edilmiştir. Sonuçlar, doğrudan sıvı soğutması ile en yüksek fosfor partikül sıcaklığının

147 °C'nin altında kaydedildiğini, daha büyük çaplı parçacıkların aynı sayıda parçacık sayısı için Pc-LED paketine daha yüksek ısı aktarımı yaptığı gösterilmiştir. Ayrıca, parçacıkların boyut ve konuma bağlı olarak farklı yörüngelerde hareket edebildiği ve bunun beyaz ışık etkisi üzerinde etkisi olabileceği tartışılmıştır.

ACKNOWLEDGMENTS

I would first like to express my sincere appreciation to my advisor Prof. Dr. Mehmet Arik, for giving me the opportunity to carry out my master's study under his supervision. His dedicated involvement, guidance, and continuous support, even during the pandemic, helped me a lot in the completion of this work. It has been a privilege to be one of his students. His motivation, enthusiasm, perspective, and things that I learned while working at EVATEG Center will stay with me as an inspiration for a lifetime.

My appreciation also extends to Assistant Prof. Altuğ Başol, Dr. Mehmet Barış Doğruoz, and Assistant Prof. Mete Budaklı for their valuable discussions and suggestions to accomplish this study. I would also like to thank Ozyegin University and EVATEG Center for the financial aid and utilization of great resources. I thankfully acknowledge the Scientific and Technological Research Council of Turkey (TÜBİTAK) for the partial support during my research.

I would like to thank my colleagues Mohammad Azarifar and Ahmet Mete Muslu for being excellent team members to share and develop ideas with. I feel very fortunate to have had the opportunity to work with you. I would also like to thank the rest of the members of the EVATEG Center for their contributions and support. A special thanks go to my dearest friends for their warm presence in every aspect of my life. Days spent with you made everything easier for me.

Most importantly, none of this could have happened without my family. I am eternally grateful for their love, trust, and support. Thank you for encouraging me to pursue my interests and allowing me to follow my dreams.

TABLE OF CONTENTS

LIST OF TABLES

LIST OF FIGURES

NOMENCLATURE

A	Area (m^2)
a	Model constant
b	Model constant
C_D	Drag coefficient
c_p	Heat capacity (J/kg-K)
D	Diameter (m)
F	Force (N)
g	Gravitational acceleration (m/s^2)
Gr	Grashof number, $\left(\frac{g\beta\Delta T D^3 \rho}{\mu}\right)$
h	Heat transfer coefficient (W/m^2-K)
I	Current (mA)
k	Thermal conductivity (W/m-K)
L	Length (mm)
m	Mass (kg)
n	Number of particles
Nu	Nusselt number, $\left(\frac{h d_p}{k_f}\right)$
P	Power (W)
Pr	Prandtl number, $\left(\frac{\mu c_p}{k}\right)$
Q	Heat generation (W)
R	Resistance (K/W)
Ra	Rayleigh number, $(\mathbf{Gr\ Pr})$

Re	Reynolds number, $\left(\frac{\rho d_p \lvert v_p - v_f \rvert}{\mu}\right)$
S	Source term
St	Stokes number, $\left(\frac{\rho_p d_p^2 v_f}{18 \mu_f L}\right)$
T	Temperature (°C or K)
t	Time (s)
v	Velocity (m/s)
V	Volume (m^3)
δV	Cell Volume (m^3)
β	Thermal expansion coefficient (1/K)
Δδ	Uncertainty
ε	Emissivity
κ	Thermal diffusivity (m^2/s)
λ	Wavelength (nm)
μ	Viscosity (Pa.s)
ρ	Density (kg/m^3)
τ	Relaxation time (s)
φ	Volume fraction
Ψ	Streamline

ABBREVIATIONS

AC	Alternative Current
Al	Aluminum
AlGaInP	Aluminum Gallium Indium Phosphide
CCD	Charge Couple Device

CCT	Correlated Color Temperature
CFD	Computational Fluid Dynamics
COB	Chip on Board
CRI	Color Rendering Index
DC	Direct Current
DPM	Discrete Phase Model
FE	Finite Element
FOM	Figure of Merit
FVM	Forward Voltage Method
FWHM	Full Width at Half Maximum
GaAs	Gallium Arsenide
GaAsP	Gallium Arsenide Phosphide
GaN	Gallium Nitride
HFE	Dielectric Fluid (Hydrofluoroether)
HID	High Intensity Discharge
ID	Identification Number
InGaN	Indium Gallium Nitride
IR	Infrared
KE	Kinetic Energy
LED	Light Emitting Diode
LC	Liquid Crystal
MIH	Microscopic Hyperspectral Imaging
MNPT	Magnetic Nanoparticle Thermometry
OLED	Organic Light Emitting Diode

Pc	Phosphor Converted
PCB	Printed Circuit Board
PCE	Power Conversion Efficiency
RGB	Red-green-blue
RHS	Right-hand-side
SDM	Source Delay Measurement
Si	Silicone
SiC	Silicone Carbide
SMD	Surface Mounted Device
SPD	Spectral Power Distribution
SSE	Sum of Square Errors
TiO_2	Titanium (IV) Oxide
TSEP	Temperature Sensitive Electrical Parameter
TSOP	Temperature Sensitive Optical Parameter
UV	Ultraviolet
YAG:Ce	Cerium Doped Yttrium Aluminum Garnate
ZiO	Zinc Oxide

CHAPTER I

INTRODUCTION

1.1 Brief History of Lighting

Historical evolution of lighting dates back to 164,000-125,000 years ago [1,2] as modern humans controlled fire for source of warmth and illumination, dealing with bonfires, cressets, torches, and candles burnt near 1000°C [3]. Over thousands of years, illumination relied on the control of the flame and burning fuels created from olive and seed oils, animal grease and tallow [4] until the emergence of gas and electric lamps in 18th and 19th centuries which regarded as the beginning of modern lighting [5,6].

Figure 1: Early forms of light generation (cresset, bonfire, torch, candle) [7–10].

The first coal-gas powered gas lamp that replaced oil and tallow-based illumination was introduced in 1790 by a Scottish engineer named William Murdoch. Coal is a combustible rock that produce flammable gas when heated and at that time Murdoch was experimenting on heating of combustible materials for illumination. After few years of conducting series of experiments, he developed a workable system that can distil and distribute coal gas for light generation. Correspondingly, in early 1800s, many businesses started shifting their focus to the coal gas production and distribution. Notably, coal-based gas lighting industry has showed significant growth and gas lamps begin to illuminate numerous large city streets in United States and Europe by providing 75% cost efficiency, easy and safe operation compared to the previous primitive light sources [11]. Although the widespread usage of gas lamps continued for years, the future of gas lamp was shorter than expected. Around the same time of the invention of gas lamps, in 1800s, an English chemist and inventor Sir. Humphry Davy created the first electric light with passing a current through a platinum strip. Even though his invention was not able to provide enough light for long period of time and impractical for common usage in street lighting, the introduced electrical arc lamp received great attention from the community and set the beginning of the history of electric lighting.

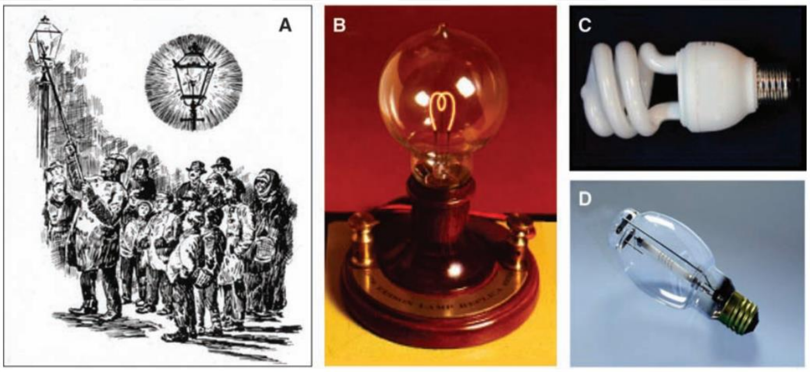

Figure 2: (a) Sketch from 1880s depicting the nightly illumination of a gaslight. (b) Replica of Edison’s lamp. (c) Compact fluorescent lamp. (d) High-pressure sodium lamp [12].

Following the introduction of the first electric light source, more than 70 years, scientists and engineers worked on the development of cost-efficient electric lamp with longer lifetime and that is suitable for commercial development and large-scale production. But it was not until 1879 that Thomas Edison suggested deep vacuum and high resistance bamboo filament as an effective electric light bulb. Although the average efficiency of the initial standard Edison lamp, also named as “incandescent lamp”, was only 2.8 lm/W [13], his efforts resulted in incandescent light bulbs being more advantageous than any other light sources in terms of economical, practical and safety aspects.

As the electricity became the primary source of illumination and widely used for light production, other alternative light sources such as fluorescent and high intensity discharge (HID) lamps have been offered to replace the incandescent lamp. Meanwhile, new technologies like tungsten filaments [14] and mercury vapor light [15] has also been introduced by making incandescent lamps more efficient than before to keep up with this competition. Remarkably, incandescent light bulbs reached the efficiency of around 15 lm/W where the invention of tungsten wires, vacuum pumping, and glass/ceramic technologies significantly improved their efficiencies.

Compared to incandescent lamps, longer lifetime and lower energy consumption capabilities made fluorescent lamps highly popular during 20th century. However, their efficacy was still limited to 90 lm/W because of the temperature losses (up to 3000 K). Meaning that nearly all electrical energy was being converted to heat while generating only small fraction of light. In addition, economic and environmental concerns, and shortcoming of incandescent, fluorescent, and HID lamps motivated researchers to find new ways to produce light more efficiently.

1.2 Historical Background of Light Emitting Diodes (LEDs)

Inorganic materials’ light emitting capability was first discovered by Henry Joseph Round in 1907. At the time, H. J. Round was experimenting on SiC (silicone carbide) crystal at the Marconi Labs, and he was originally trying to find a way to improve frequency signals of the radio detectors. During one of his experiments, H. J. Round noticed something unusual from the SiC crystal. He detected “yellowish light” coming from the junction of the carbondum crystal when he applied potential between two points of the crystal detector [16]. Following that he decided to conduct more experiments to better understand this behavior and came to conclusion that depending on the crystal type, different light colors can be obtained from different crystal detectors with the supplied voltage. Shortly after this discovery, his findings are published in journal of Electric World under the name “A Note on Carborundum” (see Figure 3(b) for the original publication). Although H. J. Round passed into the history as the discoverer of the electroluminescence phenomenon, his results had no impact on subsequent research studies conducted in this field.

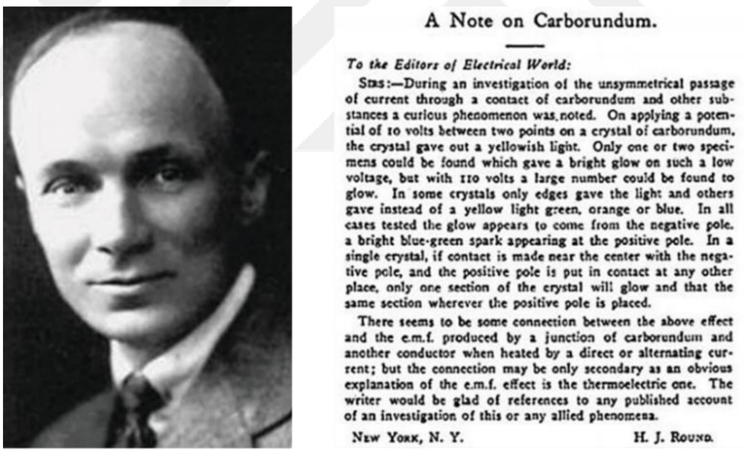

A Note on Carborundum.

To the Editors of Electrical World:

SIRS:—During an investigation of the unsymmetrical passage of current through a contact of carborundum and other substances a curious phenomenon was noted. On applying a potential of 10 volts between two points on a crystal of carborundum, the crystal gave out a yellowish light. Only one or two specimens could be found which gave a bright glow on such a low voltage, but with 110 volts a large number could be found to glow. In some crystals only edges gave the light and others gave instead of a yellow light green, orange or blue. In all cases tested the glow appears to come from the negative pole, a bright blue-green spark appearing at the positive pole. In a single crystal, if contact is made near the center with the negative pole, and the positive pole is put in contact at any other place, only one section of the crystal will glow and that the same section wherever the positive pole is placed.

There seems to be some connection between the above effect and the e.m.f. produced by a junction of carborundum and another conductor when heated by a direct or alternating current; but the connection may be only secondary as an obvious explanation of the e.m.f. effect is the thermoelectric one. The writer would be glad of references to any published account of an investigation of this or any allied phenomena.

NEW YORK, N. Y. H. J. ROUND.

(a) (b)

Figure 3: (a) Henry Joseph Round (b) H. J. Round’s paper: “A note on Carborundum” [17].

Almost 13 years later, a talented Russian technician named Oleg Vladimirovich Losev independently discovered electroluminescence phenomenon when he was working in a Radio laboratory in Soviet Union [18,19]. To better understand the light emission capability of crystalline materials, Losev conducted additional experiments over zinc oxide (ZiO) and SiC crystals used in radio receivers. As a result of these investigations, he proposed the first correct theory for the electroluminescence behavior and despite the fact that LEDs had not yet been developed, Losev's findings formed the basis of the discovery of the today's LEDs [20].

The first modern LED was accidentally invented by James R. Bob Biard and Gary Pittman in 1961 at Texas Instruments in Dallas. Biard and Pittman's original attempt was to build a laser diode. While experimenting on Gallium Arsenide (GaAs) they noticed a significant resistance and voltage drop between the ohmic contacts of GaAs when on forward biased condition. After conducting further studies to better understand this observation, Biard and Pittman realized that semiconductor material's photoconductive reaction was caused by infrared emission of absorbed photons from tunnel junction [21]. Although the findings of Biard and Pittman lead to commercialization of first modern LED, because the wavelength spectrum of the photons emitted from the LED was infrared, which is outside the visible region of human eye, the first modern LED introduced by Texas Instruments was not suitable for the practical usages.

In 1962, Dr. Holonyak Jr. from General Electric's Solid-State Device Research Laboratory Company introduced the first visible red LED made from the compound of semiconductor alloy gallium arsenide phosphide (GaAsP) which is capable of emitting red light in visible region with its wider bandwidth. It should be noted that the efficacy of Holonyak's first red LED was only 0.1 lm/W and it gave very dim light that was only apparent in dark [22]. However, Holonyak was a forward thinking tenacious researcher who believed in the possible advantages LEDs may offer. Taking it one step further, he forecasted that the lamp of the future would be small scale device that provides 10 times more efficiency than the filament made light bulbs. With those notions in mind, he continued his research to improve the efficacy of the LEDs and initiated the practical usage of LEDs in various fields.

Figure 4: Dr. N. Holonyak Jr. [23].

In years to come, semiconductor materials were to be employed as fundamental compound for the commercial growth of the LEDs [24]. In 1972, Holonyak's gradutate student M. George Craford developed the very first yellow LED using gallium arsenide phosphide and additionally he proposed improvements for the efficiency of the Holonyak's red LED [25]. Meanwhile, Herbert Maruska and Jacques Pankove invited the first violet diode. Their work also paved the way for the invention of first nitride based blue LED [26]. In the mid-1970s, green colored LED made from gallium phosphide was also invented and in that time frame LEDs started to become more economical when compared to the very first red LED introduced by Holonyak. The growth and economic affordability of the LEDs is greatly influenced by the developments in semiconductor chip manufacturing, upgraded packaging and processing techniques. Especially, with the advancements in semiconductor materials introduced in 1980s, colored LEDs with higher brightness's began to be a feasible alternative for lighting purposes.

In 1986, the invention of the first nitride-based blue LED by Isamu Akasaki, Hiroshi Amano and Shuji Nakamura eventually revolutionized the lighting industry, allowing high power and efficient solid state lighting [27]. This breakthrough followed by rapid optimization process in LED device production, which led to a cost/lumen reduction of tenfold and a lumen/per LED package increment of twentyfold in each decade [28]. Moreover, development of blue LED initiated discovery of red-green-blue (RGB) and phosphor converted (PC) white LEDs. Correspondingly, creation of blue and white LEDs leads to a remarkable transition in general lighting applications and deservingly, Akasaki and others are awarded the Nobel Price in Physics in 2014 for the invention of blue LED (see Figure 5 for the original illustration).

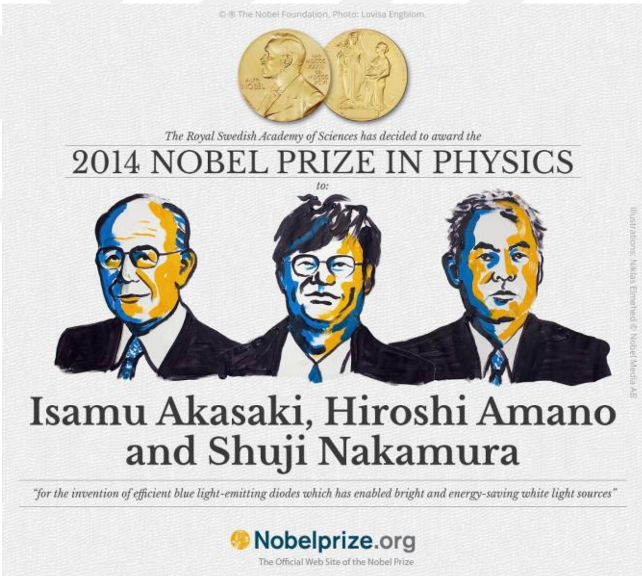

Figure 5: I. Akasaki, H. Amano and S.Nakamura from left to right. Illustration of 2014 Nobel Prize in Physics [29].

In comparison to other conventional lighting solutions, LEDs are advantageous with their superior characteristics including low power consumption, long operational lifetime with nature friendly working mechanism, wide variety of colors, and enhanced user experience with bright colors. In terms of efficacy, fluorescent lamps, despite being able to operate at almost room temperature and possibly having the longest lifespan, cannot compete with LEDs [30]. Correspondingly, at the new age of illumination, LEDs have proven to be the most efficient alternative to conventional light sources [31,32]. In fact, the US Department of Energy (DOE) project that by 2035, LEDs will hold up to 84% of all illumination applications on market [32]. Apart from low power consumption and reliability considerations, LEDs have shown the potential to go beyond the “replacement paradigm” by providing critical advantage in transportation, display and imaging systems, communications, agriculture and other fields with their advanced color control and modulation capabilities [33].

1.3 Basics of LEDs: Working Mechanism and Properties

A diode is a semiconductor circuit element that functions as a one-way switch that permits current flow only in one direction (i.e., forward direction). As the name suggests, LED is a type of diode that emits light when it is forward-biased. In basic terms, when a voltage above a threshold value is supplied to an LED, electrons and holes (free carriers) recombine in the depletion region (or active region), causing energy release in the form of photons [34]. Naturally, atoms of semiconductor materials are bonded to each other in such a way that free charge carriers cannot move to conduct electrical current. However, impurities are often added to a semiconductor system to increase the conductivity. This process is generally referred as “doping,” and since semiconductor materials have a relatively low bandgap, various conduction ratios can easily be achieved with different doping amounts. Semiconductor dopings can be divided into two categories: n-type dopants (donors) and p-type dopants (acceptors). If the semiconductor doped with additional electrons, it is called an n-type semiconductor whereas semiconductor doped with extra holes referred as p-type semiconductor.

As the term implies, a p-n junction is formed by the combination of p-type and n-type materials. When no voltage is applied to the semiconductor, n region electrons diffuse across to the junction to combine with the holes. As a result of hole filling process, negative ions are produced, and positive ions are left behind while charge accumulation result in the formation of a depletion region that prevents onward free electron flow unless it is forward biased. On the contrary, applied voltage in the forward direction, aids electrons in breaking through the depletion region and allow them to flow freely with minor resistance only. Illustration of basic structure and schematic of a typical p-n junction LED on forward biasing is provided in Figure 6 for reference. As it can be seen from Figure, free electrons flow from negative to positive charged region while holes follow path in the opposite direction.

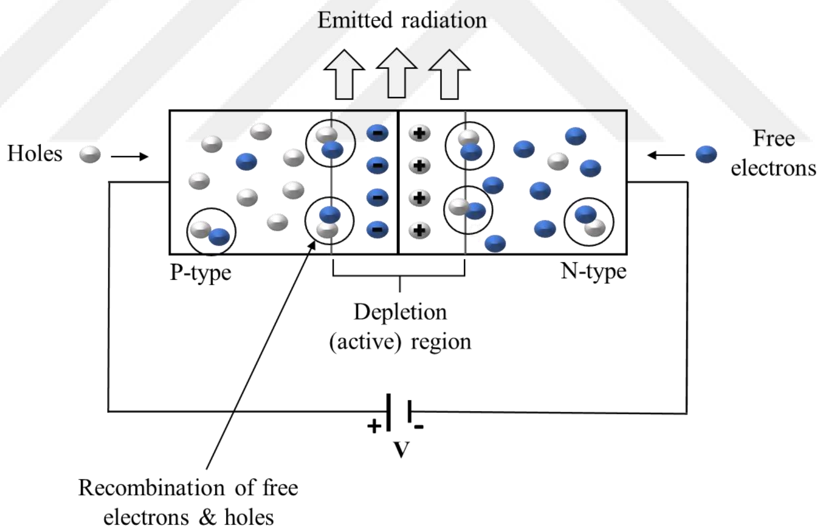

Figure 6: Schematic of a basic structure of an LED with forward biasing.

It is important to state that emitted light during the band-to-band recombination may be visible or invisible to human eye which depends on the energy level difference between the conduction and valance bands. Furthermore, it can be said that light characteristics, visibility and color are directly related to the energy band gap of a semiconductor material [35]. Correspondingly, wavelength of the emission can be engineered with band gap control of the materials in the diffusion region between p-type and n-type regions of an LED, within a few microns near the p-n junction ($\lambda = 1240/E_g$ nm) [36].

LEDs are now capable of photon emission in all visible light wavelengths by progressing from ternary ($GaAs_{1-x}P_x$) material selection to quaternary compositions (AlGaInN). To achieve even higher brightness, superlattice heterostructure made up of alternating group III nitride material with different band-gaps with each layer in thickness few nanometers are being used [37]. Because of their high thermal conductivity, electron saturation drift velocity, critical breakdown voltage, and fracture toughness to resist defects growth, group III nitride materials are ideal for unlocking higher powers in LEDs [38]. However, given the fraction of input power of previous lighting technologies and highest power conversion efficiency of any known man-made light source, it is difficult to keep them operating at a low temperature due to local heating at active region of an LED device.

1.4 Thermal Issues in LEDs

LEDs (along with all other power semiconductor devices) act as discrete heat sources, dissipating heat through electronic packages into printed circuit boards (PCBs) and heat sinks. Currently in optimum current densities of LEDs, around 70% of the input electrical power converts into heat generation [39]. Figure 7(a) shows the structure for a sample lead frame with a metal/plastic body package [40]. As shown in Figure 7(b), the primary cause of temperature rise in LEDs is the stacked thermal resistance barriers in their complex thermal architecture [41,42]. Junction temperature (T_j) is the largest recommended operating temperature in an electronic structure which is shown in the thermal resistance network in Figure 7(b). As indicated by numbers (1 to 3) in thermal resistance map of a typical LED in Figure 7(b), heat is being generated in an LED at (1) the active region due to non-radiative recombination, inside of the optical cavity due to the radiation absorption, electrical structures and semiconductor metal interfaces due to Joule heating [43], (2) phosphor–polymer composite/coating in white LEDs due to Stokes shift and thermal quenching of phosphor [44–48], and (3) outside of the optical cavity due to the radiation absorption and other electrical structures due Joule heating [49,50]. Currently chip on board, wafer level and chip scale packaging are most popular designs in the LED market for heat dissipation [51]. Over the past two decades, the thermal resistance of the packages reduced from 8 K/W [52] at 2008 to 5 K/W [53] at 2016 and now at 3.5 K/W [54].

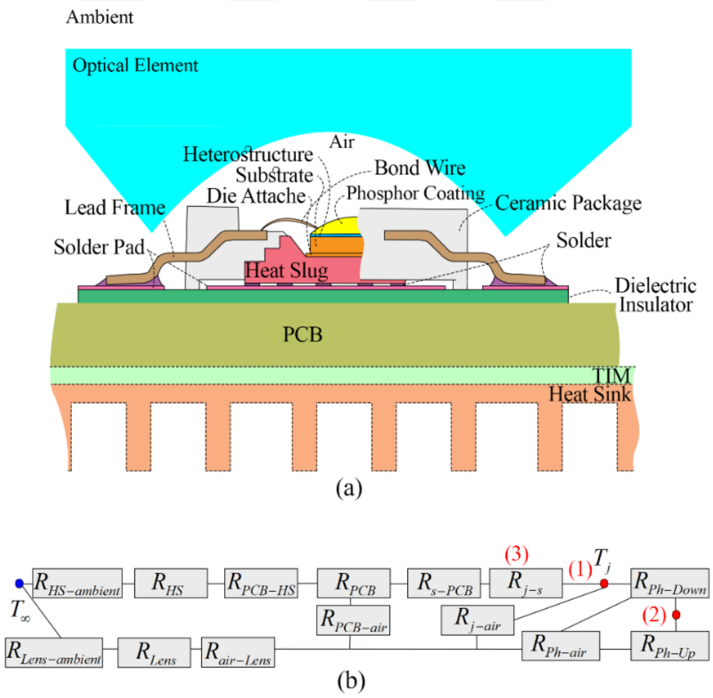

Figure 7: (a) Schematic overview of the package and structure of a typical LED luminaries. (b) Thermal resistance network.

Besides compact size, the challenge in reducing the thermal resistance of an LED package is mainly related to the scarcity of suitable substrate materials where chips are grown hetero-epitaxially on foreign sapphire and SiC substrates [55–57].

Additional interfacial thermal resistance between each grown layer also intensifies the total thermal resistance of the package [42,58,59]. These types of integrations as shown in Figure 7(b), limits the heat dissipation capability of the package due to introduction of interfacial thermal resistances where the thermal characterization techniques are rarely investigated [60]. Attachment of a package to PCB introduces additional three-dimensional thermal resistance where the solder joint quality and thermomechanical properties of the package can also restrain the heat dissipation. Furthermore, there is another heat dissipation barrier from PCB to any additional heat sink and also from phosphor layer to the lens and at the end to the external environment [61].

The temperature rise of the chip influences luminance performance of an LED as well as temperature induced failure, in contrast to incandescent lamps which can cool themselves radiatively [62]. The aging and degradation of LEDs, the majority of which are caused by high temperatures, has long been a topic of debate [63–66]. High T_j was seen exceedingly limiting the life time of LEDs [67,68] and successful thermal management is found to be the key aspect to tackle these problems [69]. However, to offer a suitable thermal solution, interpret photometric characteristics and package capabilities, and make lifetime predictions, it is required to adapt a steady-state and transient junction temperature characterization in large range of conditions.

1.5 Phosphor Converted (Pc) White LEDs

Phosphor converted white light-emitting diodes (Pc-LEDs) are commonly used as a white light source in illumination applications. Even though RGB color blending method is one of the well-known techniques to produce white light, due to low quantum efficiency of monochromatic LEDs [70] and the difficulties encountered during RGB color mixing processes [71], Pc-LEDs are more widely preferred [72,73]. White light generation in dichromatic Pc-LEDs accomplished by combining cerium-doped YAG phosphor (wavelength converted) with blue luminescence (blue LED) [16]. Pc-LEDs utilize photoluminescence effect of phosphor, in which white light conversion is accompanied by additional heat generation when emitted blue light combines with the phosphor. To implement phosphor to the package, either LED chip is directly coated with a phosphor material (conformal coating), a layer of phosphor is placed over the inner surface of the lens (remote coating), or phosphor is uniformly distributed in a reflector cup inside the package (phosphor-in-cup) [74] (see illustration in Figure 8). Depending on the choice of the arrangement, shape and composition of the phosphor layer, thermal and optical performance of the Pc-LED show considerable differences due to photoluminescence effect of phosphor [75,76]. Additionally in case of a high-power emissions, phosphor thermal quenching is observed in all of the aforementioned packaging techniques.

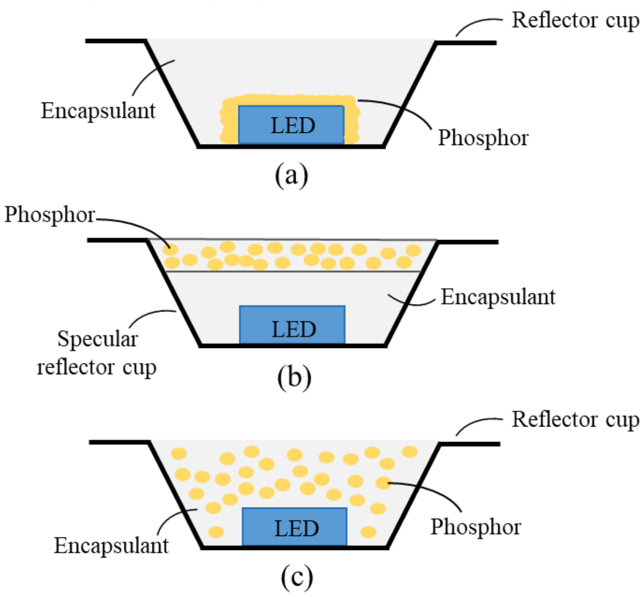

Figure 8: Common phosphor implementations for white light generation: (a) Conformal coating (b) Remote coating (c) Phosphor-in-cup.

Importance of phosphor heat generation and thermal quenching over the color quality (CRI, CCT and uniformity) and lifetime (degradation rate) of Pc-LEDs has already recognized in previous studies [77–79]. In fact, comparison analysis has concluded that highest temperatures are always observed in the phosphor layer regardless of the adopted coating orientation [80]. Although the package and system level cooling solutions for LEDs are presented over the years [81], the excess amount of heat generation in the phosphor layer is still a critical thermal limitation for device performances. Therefore, in recent years, the importance of phosphor related thermal issues in Pc-LEDs has been highly emphasized to come up with novel phosphor arrangement [82–84]. According to the local particle analysis of Arik et al. [77], the temperature of phosphor ($T_{phosphor}$) can exceed the junction temperature (T_j), when an effective cooling is not provided. High phosphor temperature ($T_{phosphor}$ >300 °C) can cause irreversible degradation and even phosphor carbonization [45] and therefore special attention should be paid to the thermal management of phosphor in Pc-LED white light systems.

1.6 Scope and Outline of the Present Study

In line with the above-mentioned thermal, optical, and electrical concerns with current Pc-LED devices this thesis aims to:

In Chapter II:

- Provide a detailed literature review for currently employed T_j measurement techniques for the purpose of attempting to address the governing phenomenon, benefits, drawbacks, possibilities, and applications of each technique.

- Compare different T_j measurement techniques to provide insight into the topic and direction for future research.
- Discuss the non-ideal thermal calibration processes and current accuracy concerns to form a better understanding of the motivation to come up with an improved dynamic T_j characterization approach.

In Chapter III:

- Propose a more accurate and time efficient forward voltage measurement method.
- Experimentally characterize transient and dynamic opto-thermal behavior of bare and coated LED chips under operation.
- Introduce a novel immersion cooling combined with YAG:Ce phosphor to overcome the thermal challenges of current Pc-LEDs.
- Conduct particle based experiments to form an understanding for the thermocapillary flow of dielectric fluid and accumulation behavior of immersed phosphor particles.

In Chapter IV:

- Numerically analyze the thermal performance of newly proposed immersion cooled Pc-LED.
- To propose an advanced and dynamical numerical approach that enables particle-based analysis of immersion cooled phosphor and closer examination of the location dependent self-heating of phosphor with light interaction.

- Provide insight about critical design parameters and their relative impact on the opto-thermal performance of Pc-WLEDs.
- Discuss the changes recorded in temperature and kinetic energy levels that can be used to control the distribution of the circulating phosphor at optically and thermally favorable orientations in future studies.

CHAPTER II

LITERATURE REVIEW

Over the last 20 years, different T_j measurement techniques have been introduced by researchers, and those measurement methods have progressed over the years. Yet, it remains to be a hot topic since researchers are frequently coming up with novel approaches to determine the T_j or making improvements over the existing techniques. It is important to note that experimental T_j measurement of LEDs is not a straightforward task. The majority of the LED modules comprise surface covering lens, encapsulation, and other package components that obstruct the chip temperature measurements. This highlights the fact that the selection of appropriate techniques may be limited by the unique requirements and operating conditions of the inspected device. Correspondingly, the literature review part aims to put an emphasis on various experimental measurement techniques that are available to assess the T_j of LEDs. This chapter is composed of a large number of summaries of investigations done on T_j of LEDs and gives detailed discussions for the advantages and disadvantages inherent to each technique based on findings presented in the literature. Selection of experimental parameter reports of different researchers are given as a reference for comparison.

The literature review part starts by looking at temperature sensitive optical parameters (TSOPs) that are used for T_j determination. Conventional approaches such as wavelength shift and broadening as well as new techniques like microscopic hyperspectral imaging are covered. Later, optical temperature probing methods like infrared thermography, thermoreflectance, Raman spectroscopy, and liquid crystal thermography are analyzed. Spatial and temporal resolutions, temperature sensitivity, and accuracy are taken into account when comparing these approaches. Later, temperature sensitive electrical parameters (TSEPs) are investigated, and the primary focus has been given to the well-known forward voltage measurement (FVM) technique, while literature examples of other existing electrical temperature methods used for LEDs are also mentioned. A table summarizing the benefits, drawbacks, capabilities, and future possibilities of various techniques are provided in summary and conclusions.

2.1 Temperature Sensitive Optical Parameters (TSOPs)

T_j may be indirectly measured using an LED's inherent optical characteristic. The emission spectrum of a semiconductor device is influenced by temperature variations due to the temperature dependence of the energy bandgap [85]. This behavior motivates researchers to use spectral power distribution (SPD) characteristics such as peak wavelength and spectral bandwidth of LEDs, which are known as temperature sensitive optical parameters (TSOPs), to estimate T_j [86]. TSOP T_j measurement method is a non-destructive and do not interrupt the electrical performance of the LEDs [87–91] (e.g., in case of an alternating current (AC) LEDs [92], TSOP based T_j measurements have shown successful implementation without altering their electrical performance [93].)

The TSOPs are unique for each electrical working condition and light output changes depending on the internal quantum efficiency and bandgap characteristics of an LED at each specific temperature and input current [94]. Summarized illustration of the SPD response to temperature and input current induced changes of an arbitrary white LED is shown in Figure 9. It is known that with an increasing T_j, SPD shows a red shift and broadening [95]. This red-shift phenomenon is primarily due to the band-gap reduction. This was explained by Wang et al. [96,97] for GaN based blue LEDs in low temperatures and recently similar results were reported at high temperatures for high brightness GaN on sapphire blue LEDs [98]. It should be noted that SPD displays a blue shift and broadening with increasing input current.

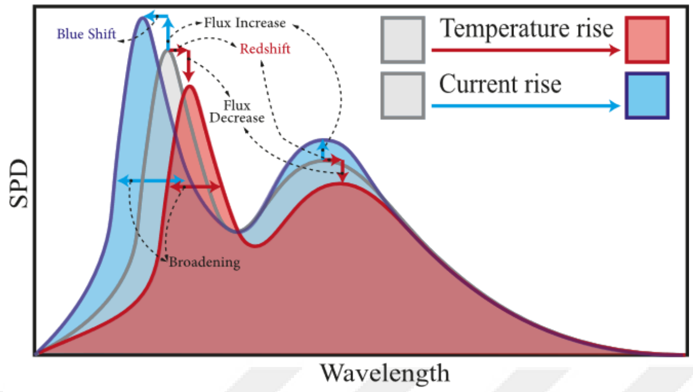

Figure 9: Illustration of temperature and input current induced changes of spectral power distribution (SPD) for an arbitrary white LED.

Li et al. [99] studied the effect of input current and temperature on the spectral behavior of green InGaN/GaN multi-quantum well LED and showed that the excitation source could alter the carrier dynamics in the active region. A large blue shift was observed in high input power levels mainly due to the carrier screening effect as a result of a weakened piezoelectric field that causes the quantum-confined Stark effect [100]. This issue can be verified by the findings of Kim et al. [101] which analyzed carrier leakage of GaN-based on photoluminescence properties of LEDs both at forward biased and intentionally formed leakage path conditions. Increased current leakages were observed in low series resistance for LEDs which led to a blue shift of the SPD. At temperature range of 273 to 338 K, Lin et al. [95] identified an almost linear relationship between the center of mass wavelength and full width at half maximum (FWHM) with T_j at input currents of 150 to 850 mA for GaN-based blue LED. The slope of the center of mass wavelength per T_j was below 0.034 nm/K while for FWHM, broadening was above 0.052 nm/K. Assuming high precision temperature measurements by taking precise optical measurements within 0.1 nm, the accuracy of T_j measurement based on wavelength shift was around 3 K while the FWHM measurement could reach below 2 K. Based on this, the authors concluded that FWHM calibration can yield high accuracy in T_j evaluation. It should be noted that spectral width and shape of the LED emission can also be associated with carrier distribution, the density of states, and the successful pairing of electrons and holes, etc. [102]. Even though band-filling effects can be eliminated with calibration experiments, alloy broadening and kT broadening are still a concern for the accurate determination of the spectral lines. Considering these issues, the accuracy of the wavelength shift method is stated to be only 5-10% of the FWHM of the emission line [16]. However, in devices with narrow emission, the accuracy of the wavelength shift method increases and can be a suitable approach for T_j prediction [103].

Chhajed et al. [104] calibrated the peak wavelength of UV, blue, green and red GaN based LEDs for a forward current range of 10 to 100 mA at temperatures of 22 to 120 °C. Similarly, a high temperature coefficient of the spectral width was determined in comparison to the wavelength shift. Temperature coefficients of dominant wavelength for the blue, green, and red LEDs were determined as 0.0389, 0.0308 and 0.1562 nm/K correspondingly. These slopes increase to 0.0466, 0.0625 and 0.1812 nm/K for the FWHM based T_j evaluations. Similarly, a strong red shift of red AlGaInP LED was also seen in another study of authors for trichromatic white LED system [105]. Blueshift was negligible for the red LED and slightly higher in the UV LED while the highest blueshift effect was recorded for the green LED. The authors stated that the uncertainty of T_j estimation based on the wavelength shift method is higher in comparison to the FWHM method. Furthermore, the authors have preferred FVM with a reported accuracy of ±3 °C over TSOP method.

Chen et al. [106] conducted T_j estimation experiments and obtained peak wavelength shifts for three different AlGaInP LED arrays. Shifting characteristics investigated at longer, central, and shorter wavelengths shown that center wavelength is the most suitable method to calculate T_j of an LED array. Tamura et al. [107] analyzed the wavelength shift of InGaN based white LED at temperatures from 20 to 160 °C and their investigations have shown that blue light emission from the active layer and yellow light emission from YAG:Ce phosphor formed two different electroluminescence bands while each band has displayed a distinct behavior with the temperature change. However similar to previous cases, T_j was stated to be successfully calibrated to the blue emission of the chip. Chen et al. [108] have shown a simplified peak wavelength shift variation at different T_j for white LED under different drive currents. Their findings have shown that temperature dependence of peak wavelength is lower for direct current (DC) LED compared to bilevel drive while thermal energy needed for correlated color temperature (CCT) stabilization is also less for a DC LED. Gu et al. [109] selected the point of interest as the lowest energy in the SPD between the peaks of blue and yellow emissions. The ratio of the total radiant energy of white LED to the radiant energy within the blue emission in different T_j has shown a linear relationship. They reported that with a ratio of 0.005, the temperature prediction accuracy of 1 K can be achieved in commercial white LEDs with this relation.

TSOP based methods have also shown to be a practical approach for measuring phosphor temperature in an operating white LED. Based on the total emission division of a white LED to a sum of the spectrum of the blue chip and two spectrums from phosphor with a short and a long wavelength band, Yang et al. [110] examined the fitting peak wavelengths and FWHMs of the short and long wavelength bands at the different phosphor temperatures. They have stated that phosphor temperature can be precisely measured by checking the variations of its related emission spectrum. Similar to the LEDs, redshift at higher temperatures was observed. Linear relationships were seen for FWHM and peak wavelength of the phosphor in different temperatures. However, this model is limited to be practical for the same phosphor only and it can't be used for mixture of different phosphors combinations.

Recently TSOP based temperature measurement methods are extended for two-dimensional (2D) thermal mapping. Based on new microscopic hyperspectral imaging (MHI), the 2D spectral power distribution can be obtained from light emitting surfaces and can be used to incorporate TSOP for surface temperature measurement of the LEDs. Jin et al. [111] used MHI based centroid wavelength method to study 2D temperature distribution of the blue, green and red LEDs (see Figure 10). After calibration of centroid wavelength coefficient, authors reached as low as 3 μm resolution for surface temperature measurement of the LEDs which is claimed to be capable of reaching sub-micron level accuracy.

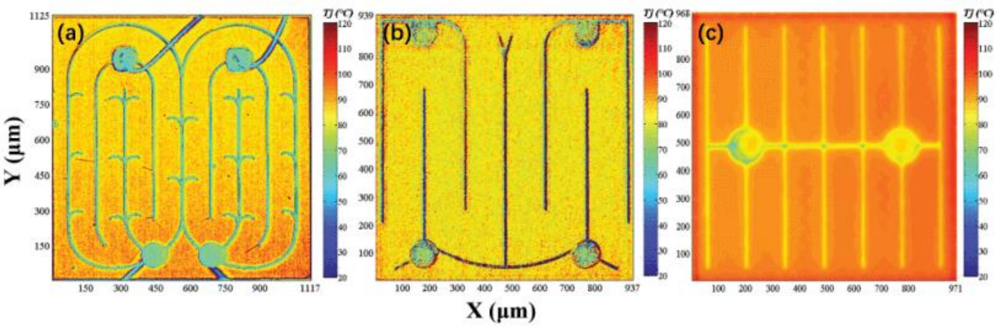

Figure 10: Two-dimensional (2D) temperature distribution of (a) blue, (b) green and (c) red LED measured with microscopic hyperspectral imaging (MHI). To prevent temperature fluctuations, average of 2 × 2 pixel temperature is taken in both X and Y direction [111].

This method is also shown practically in micro-LEDs. Feng et al. [112] recently performed a thermal study on GaN based micro LEDs. Temperature dependence of the bandgaps of the chip based on the SPD was studied. In temperature range of 25 to 80 °C, FWHM broadening from 27 to 35 nm and redshift attributed to bandgap reduction of 0.024 eV was observed. Although authors proposed that micro-LEDs bandgap behavior with T_j follows a semi-empirical Varshni relation, from the presented experimental results a reliable coefficient of temperature cannot be seen for FWHM or bandgap for T_j calibration. Parametric summary of TSOP based experimental LED T_j measurement reports are presented in Table 1.

Table 1: TSOP based experimental temperature measurement parameters employed in the literature for thermal characterization of LEDs. References are sorted by year. Not provided parameters are indicated by a hyphen in the table (Δδ: Uncertainty, λ: Wavelength).

Year	LED Type		Temperature Coefficient		Measurement Range				Δδ
	Color	Material System	λ_{Peak} (nm/K)	λ_{FVHM} (nm/K)	T (K)	λ_{Peak} (nm)	$\lambda_{Centroid}$ (nm)	λ_{FWHM} (nm)	(K)
2004 [90]	Red	AlGaInP	0.1376	-	298-343	627-640	-	-	-
2005 [104]	Red Blue Green	AlGaInP GaInN GaInN	0.1562 0.0389 0.0308	0.1812 0.0466 0.0625	295-393	629-644 460-464 517-519	-	19.2-30.8 23.9-26.7 46.6-50.4	10
2012 [95]	Blue	-	0.03181	0.0532	298-338	453-454.5	-	19.3-22	-
2013 [106]	Amber	AlGaInP	-	0.052	295-338	591-597	-	-	-
2014 [108]	White	-	0.085	-	300-370	450.5-456.5	-	-	-
2014 [88]	White	InGaN	0.04	-	298-363	-	-	-	-
2018 [113]	UV	AlGaN-NanoWire	0.027	-	298-358	-	-	-	-
2019 [111]	Red Blue Green	AlGaInP GaInN GaInN	0.108 0.026 0.025	-	298-348	- - -	650.3-655.5 455.4-456.7 531.7-523.9	-	0.9

2.2 Optical Temperature Probing Methods

Optical temperature probing techniques are generally nondestructive, and easy to handle with a minimum or no downtime. However, the studied surface should be exposed so that temperature probing can be utilized based on reflection, deflection, interference, fluorescence, birefringence, absorption, or thermal emission optical phenomena [114]. In case of LEDs, the device cannot be probed with secondary optics, due to its determining thermal effect on T_j (refer to Figure 7) [115]. During the measurements, excitation, detection, or reference light beam is generally adopted, and variation in light properties including amplitude and phase, polarization, and frequency are recorded for the corresponding temperature evaluation. The employed light beam can be focused/defocused, polarized, and deflected, or operated in modulated and pulsed continuous wave modes to meet the desired measurement objective. Although there are a number of optical temperature probing techniques employed for thermal characterization of working electronic devices, only infrared (IR) thermography, thermoreflectance, Raman spectroscopy, and liquid crystal thermography are found to be suitable for LEDs, and included in this survey (readers can refer to [116–118] for further information about excluded optical temperature probing methods). In the majority of these techniques, measurement signals come from the surface, or a region close to the surface of the test LED, which is assumed to assimilate the actual T_j. At the same time, some methods have the potential to provide data from the internal layers of the chip. A critical drawback of some of the optical temperature probing techniques is the possible interference of the active probe source (e.g. focused laser beam) with the device's electrical and thermal performance, which can be partially avoided by carefully selecting the source's incident wavelength and power [119–121].

2.2.1 Infrared (IR) Thermography

IR thermal imaging is a real time imaging method for measuring temperature distributions [122]. Application of IR thermography can be seen for the thermal inspection of various types of LEDs, including chip on board (COB) [123], surface mounted devices (SMD) [124], and flip-chips [125]. This method is widely preferred for various thermal management related problems in LEDs [126–131]. The basic principle of IR thermography is to capture electromagnetic radiations emitted from the surface of objects in the IR spectrum and monitor the corresponding 2D temperature maps. Currently, commercially available IR imaging systems can offer temperature sensitivity within 0.1-1 K and temporal accuracy of 100 μs [132]. Although the IR region of the spectrum extends up to 100 μm, due to the sensitivity reduction above 20 μm, only the 0.7-20 μm range is used for temperature measurements [133]. A typical experimental arrangement and measurement apparatus of IR thermography is illustrated in Figure 11.

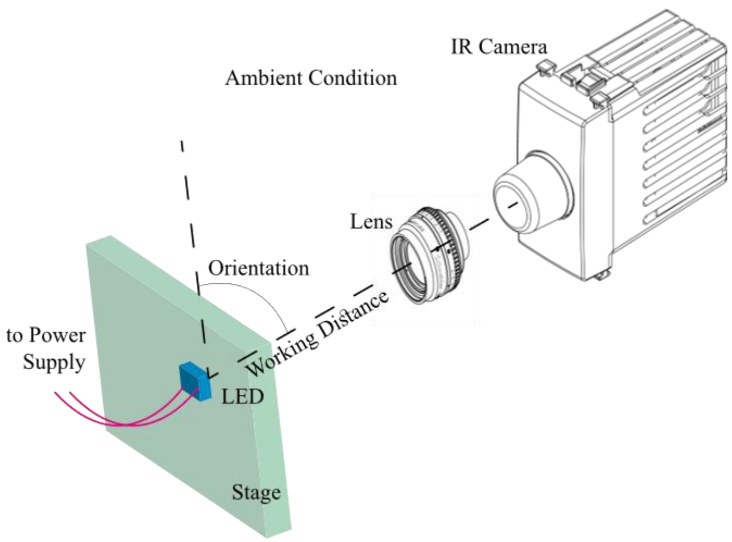

Figure 11: Schematic of the generally used experimental arrangement and apparatus of the IR thermography measurements.

The set up essentially consists of a lens with a known working distance to focus the thermal radiation on the camera's detector. Based on the orientation of the LED and ambient condition, for each set up position, an adjustable emissivity setting should be used to calibrate the detector.

Cheng et al. [134] evaluated the thermal characteristics of RGB white LEDs based on thermocouple calibrated IR thermography, FVM, and finite element (FE) method with a transparent optical lens still covering the LED chip. Emissivity values of 0.90-0.94 for the red, 0.90-0.93 for the green, and 0.92-0.94 for the blue LED were determined based on the thermocouple calibrations. The possible reason for the significant change in the emissivity was presented as the transparency of the molded lens, IR emission and reflection from other components of the LED module. Correspondingly, the authors have offered a calibration factor to improve the accuracy of the IR thermography measurements. In their analysis, a comparison of the corrected IR measurements and FVM have shown up to 30 °C temperature difference which reveals that in reality, surface temperature and T_j are not equal to each other.

Based on the forward voltage verified thermal characterizations conducted by Cengiz et al. [115], a similar emissivity value of 0.9 for the Pc-LED with a molded lens was found to be an accurate calibration for IR imaging of the chip. In another study, Ozluk et al. [135] studied the effect of molded lens on T_j of a green LED by examining thermal and optical properties after the successful removal of the lens from the chip. Based on thermocouple calibrated results, the emissivity of the green bare LED was evaluated as 0.84. Authors have then recommended that proper removal of the chip covering lens can extend the accuracy and reliability of the IR measurements by decreasing the T_j difference between FVM and IR to 3.9 °C.

Chernyakov et al. [136] analyzed the thermal distribution in high power flip chip InGaN/GaN blue LED based on IR thermal radiation (see Figure 12(a)). Authors have proposed the usage of a 2.5 to 3 μm short wavelength IR camera to improve the spatial resolution of the measurements down to ~3 μm. Moreover, the emissivity variation of each LED part was accounted for temperature controlled preliminary calibrations which claimed to provide less than 2 K temperature accuracy for IR measurements. Likewise, Wu et al. [91] conducted temperature controlled calibrations to determine the emissivity of materials of high power multi chip COB LED. Following the successful calibration of the IR camera, the difference between measurement and numerical simulations was found to be less than 2%.

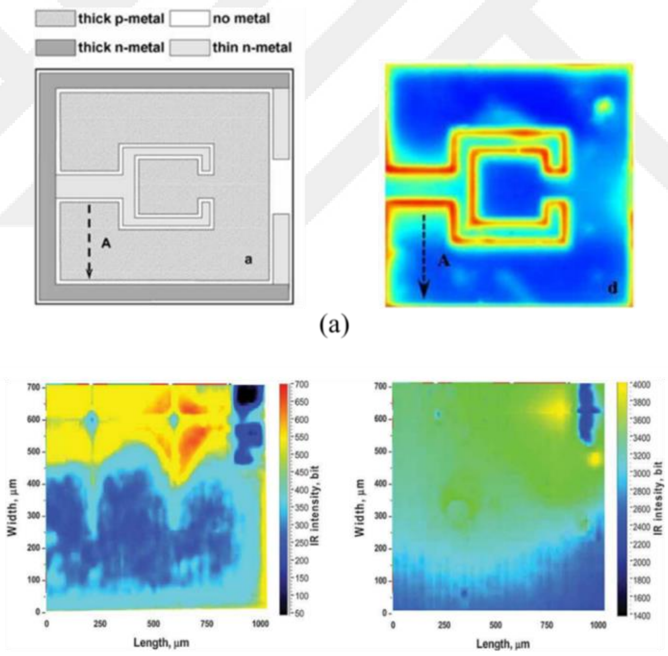

Figure 12. (a) Image of lateral infrared (IR) distribution of a flip chip LED. (Left) Schematic of the chip, (Right) captured IR emissions [136]. (b) IR emission intensity distribution of (Left) bare chip and (Right) thin film coated chip [137].

Chang et al. [126] preferred to calibrate the emissivity of GaN based green LED by black painting the empty surface of the LED wafer as a reference point. As a result of the applied correction algorithm for adjustment of response and superimposed offset signal images, the reflected radiation was analyzed, and the emissivity was corrected for each pixel. In a more recent study, Aladov et al. [137] suggested the usage of a film coating with transparency in the visible region and absorption in the IR region. Application of special thin film coating aims to prevent emission absorption of LED under test and assure real temperature mapping without falsification. A comparison of the captured IR images with and without coating is given in Figure 12(b).

Diffraction limited spatial resolution and local temperature uncertainties are two major issues of IR thermography measurements [138,139]. Even though diffraction limited spatial resolution is an inherent drawback, local temperature uncertainties can be dealt with by the calibration of the changing radiative properties of the inspected surfaces. With that being said, accurate determination of the emissivity may have uncertainty due to significant variation in the radiative properties of the materials in the heterostructure and packaging. Semiconductor layers, metallic electrodes, interconnections, coatings, and bonding elements have differing transparency or reflectance to infrared radiation which results in wrong interpretation of collected radiation and interference of emissivity values of the sublayers [139,140]. To overcome this issue, researchers have been employing various calibration techniques like two temperature maps [141,142], irradiance based emissivity corrections [143], high emissivity coatings [144] and radiative micro carbon particles [145] for the correct determination of the surface emissivity.

In general, thermal concerns still exist on the emissivity of LEDs which requires another source of reliable temperature measurement technique, usage of supplementary black coating or microparticles that may cause heat spreading, damage, or visible emission absorption that disturb operational thermal and optical behavior of LED. As depicted in Table 2, the material emissivity of semiconductors can vary significantly at different spectral bands and for interconnection metals much lower emissivity values can be observed [146].

Table 2: Summary of IR thermography focused in the literature for temperature measurement of LEDs. Not provided parameters are indicated by a hyphen in the table (ε: Emissivity).

Year	LED Type		ε	Resolution		Spectral Range (µm)
	Color	Material System		Spatial (µm or mrad)	Thermal (K)	
2010 [127]	White	-	-	-	0.1	8-13
2010 [123]	White	-	0.27 (White LED)	-	-	2.5-5.0
2012 [91]	Blue	-	0.5 (GaN) 0.89 (Sapphire) 0.02 (Au Electrode) 0.05 (Al Heat Slug)	1.07 mrad	0.05	2-15
2012 [134]	Green Blue Red	InGaN InGaN AlGaInP	0.90-0.94 (LEDs) 0.92 (Molding)	468	0.02	-
2012 [126]	Green	InGaN/GaN MQW	0.82 (GaN) 0.51 (ITO) 0.25 (Contact Metal) 0.96 (Black Paint)	15	0.03	3.5-5.1
2013 [136]	Blue	InGaN/GaN	-	3	2	2.5-3
2014 [88]	White	InGaN	0.86 (Sapphire)	30	-	8-9
2018 [113]	UV	AlGaN-NanoWire	-	-	-	7-14
2019 [111]	Red Green Blue	AlGaInP GaInN GaInN	-	30 31 32	-	-
2019 [135]	Green	InGaN	0.84 (GaN)	-	1	2.5-5.1
2019 [137]	Blue	AlInGaN	-	3	0.2	5-12
2021 [150]	Red	AlGaInP	0.84 (GaN)	-	-	-

In addition, parameters like humidity, ambient and atmospheric temperatures near the inspected object also have an unignorable influence over the radiation properties [147]. Semiconductor doping also modifies the radiative properties of the active region and as shown in the study of Welna et al. [148], when free electron concentration is increased up to 10-19 cm-3 in n-GaN active region, shifting towards shorter wavelengths (from 7 μm to 2 μm) occurs in infrared absorption band. One of the latest studies conducted by Rongier et al. [149] thoroughly discusses these property changes for different spectral bands and opacity regions. By taking the emissivity variations into account authors have successfully developed an in-lab IR thermography test bench that is calibrated for quantitative thermal analysis of high luminance LED front light.

2.2.2 Thermoreflectance

Thermoreflectance microscopy is a high resolution and non-contact thermal profiling method that measures the relative change in the reflectivity over a surface and maps the temperature distribution according to the reflectivity variation [151]. Even though the temperature dependency of material reflectivity is usually in the order of 10^{-5}-10^{-4} K^{-1} [152], temperature induced changes can be detected by incorporating a sensitive (amplified) measurement system. The benefit of thermoreflectance imaging is in its ultra-fast temporal resolution of up to 800 ps and spatial resolution of 200-250 nm if UV or visible illumination is used [153]. Moreover, it is possible to optimize thermoreflectance for a wide range of materials and it has been used to measure the temperature of various electronic components [154–160].

The temperature resolution of the thermoreflectance method depends on the noise generated during measurements and the detector's sensitivity while spectral resolution is limited by the wavelength of the optical source. In some cases, reflected and emitted light from beneath the LED surface can interfere with the surface reflectivity of the chip and can lead to an inaccurate surface temperature measurement result. To avoid this issue, Summers et al. [161] have employed thermoreflectance imaging using a confocal microscope to measure the surface temperature of the AlInGaP red LED. Results from widefield and confocal imaging were compared and verified with the FVM. A negative offset in the widefield temperature measurement method was observed and the advantage of confocal microscope imaging usage has been shown. In another study, Ling and Tay [162] thermoreflectance thermography method to study the surface temperature of phosphor coated blue LED. Measurements were carried out with a 5X zoom microscope lens with a light source of 405 nm wavelength claiming to have the lowest emission from the chip itself. LED surface reflectivity variation with temperature was calibrated and a relative reflectivity coefficient of $1.71x10^{-5}$ 1/K was determined.

Xiao et al. [163] proposed to use the relative reflected intensity of the incident exciting light to determine T_j. The lock-in method was used to extract the interference of the emitting light from LEDs and increase the measurements' dynamic range. Their proposed technique was calibrated with micro thermocouple measurements and authors stated concerns about the calibration using thermocouples due to the difference in diameters between the exciting light spot and the thermocouple and the uniformity in thermal distribution on the surface of the chip. Kendig et al. [164] made use of thermoreflectance imaging to determine the 2D temperature maps of an encapsulated UV and blue LEDs. Thermoreflectance signals were obtained with a custom 1-megapixel charge-couple device (CCD) system and the lock-in technique was implemented to increase the measurement resolution. The wavelength, surface roughness and material dependent thermoreflectance coefficients were calibrated to measure quantitative temperature values. As a result, the thermoreflectance method was found to be adequate for investigating thermal non-uniformities and transient thermal response of the LED.

In one of the latest studies, the reflective light intensity change of a blue GaN LED was exploited to derive the 2D transient temperature distribution of the operating device [165]. In contrast to other studies, the authors captured light reflection with a high-speed camera with a 505 μs to 68 μs resolution and to prevent bandgap modulation effect a 690 nm wavelength, red LED was employed as an illumination source. According to the authors, the proposed measurement method provides better spatial resolution than traditional optical probing methods, with the degradation from the homogeneity of the 2D temperature distribution occurring only at high frame rates due to a shorter exposure time.

Recently, Zheng et al. [166] employed the thermoreflectance method to study the surface temperature of lateral type blue LED chip (see Figure 13). In their measurement, reflectivity change of the golden metal electrode was recorded, and it has been observed that the thickness of the electrode was sufficiently thick to hide unwanted reflections from the underlaying materials. For the thermoreflectance experiments, an incident probe laser beam with spot surface of 3 μm was used. As a result, good agreement between thermocouple, FVM and thermoreflectance methods was observed in the T_j range of 75°C. However, discrepancies between different methods were seen at higher temperatures where FVM is showing obvious higher values. The authors state that this difference is due to the self-heating and finite thermal resistance between the T_j and measured surface points. It should be mentioned that as T_j increases significant heat flux from the surface to the ambient due to a higher transfer coefficient can be expected [167] which can result in underestimation of the surface thermography of LEDs.

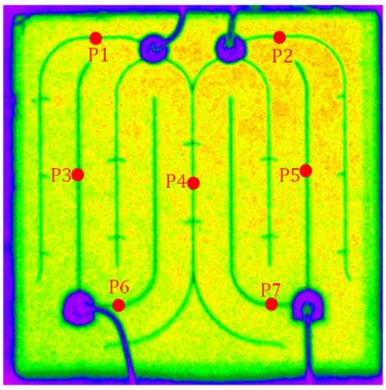

Location	T (°C)
P1	96.2
P2	95.4
P3	96.8
P4	95.8
P5	96.2
P6	98.4
P7	97.4

Figure 13: Surface temperatures of a blue LED measured at different locations with thermoreflectance method [166].

2.2.3 Raman Spectroscopy

Raman spectroscopy is a non-contact temperature mapping technique that can provide submicron spatial resolutions up to 1 μm [168] and nanosecond temporal resolutions up to 200 ns [169] during time resolved measurements. With this technique, temperature distributions across the active region of semiconductors formed by Raman active material layers are evaluated based on their phonon frequency. A typical Raman system is composed of an excitation source (often a laser) that is focused on the LED, beam splitter, sample holder and a spectrometer that can detect the frequency shifts (see Figure 14). As an excitation source, a variety of lasers such as Argon ion (488.0 and 514.5 nm), krypton ion (530.9 and 647.1 nm), He:Ne (632.8), Nd:Yag (1064 and 532 nm) and diode laser (630 and 780 nm) can be employed [170]. Temperature measurement errors due to excitation source induced heating and carrier generation can be reduced by lowering the source or by choosing a source with a wavelength below the band gap of the LED (see Table 3).

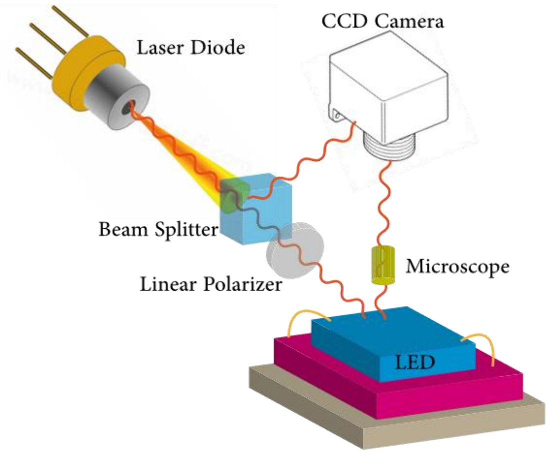

Figure 14: Schematic of a typical Raman spectroscopy setup.

It is worth mentioning that Raman spectroscopy temperature measurement of large surface areas may be impractical due to the need for raster scanning and data integration [139]. Moreover, fine temperature profiling is time consuming, because detecting Raman signals might not be easy [146]. Nonetheless, the Raman spectroscopy approach is capable of capturing temperature profiles of micron size features with high spatial resolution and it has been studied by many researchers for thermal characterization purposes (e.g Diamond [171], AlGaN/GaN [172–174], Graphene [175] and others [176–180]).

In an early study conducted by Schwegler et al. [177], Tj of InGaN based LED was obtained using micro-Raman spectroscopy. The device was driven with moderate input currents, up to 30 mA with a power density of 705 W/cm^2. Temperature evaluations were made considering the shift in GaN E^2 (high) phonon frequency with temperature, and in order to reach high spatial resolutions, the authors combined a 514 nm wavelength laser excitation source with a 0.7 μm spot diameter microscopic lens. Results from micro-Raman spectroscopy, TSOP, and FE models were found to be in good agreement, and T_j was evaluated to be 140 °C for 30 mA input current. In another study, Chitnis et al. [176] used micro-Raman spectroscopy mapping to evaluate the T_j of a 325 nm flip chipped deep UV LED (see Figure 15(a)). Similar to the previous analysis, the E^2 (high) phonon frequency shift of AlGaN was examined and to prevent light absorption by the device, a 488 nm wavelength laser that has below bandgap excitation was used as a source. LED was driven with low input currents up to 50 mA and the highest surface temperature was determined to be 70 °C, indicating a good agreement between TSOP and micro-Raman spectroscopy results. In a later study, Senawiratne et al. [181] presented a T_j analysis of GaN based blue and green LEDs with sapphire and GaN substrates by micro-Raman spectroscopy. Measurements were conducted with a 785 nm wavelength laser excitation source while the Raman frequency shift of E^2 (high) phonon was investigated. Different from previous studies, LEDs were driven at relatively higher input currents, up to 250 mA (357 A/cm^2) and Raman peak shifts to the lower wavenumber sides were observed due to thermal lattice expansion at high current levels. Considering the spectral resolution of the spectrometer used for the measurements, the accuracy of the micro-Raman technique was evaluated to be ±7°C.

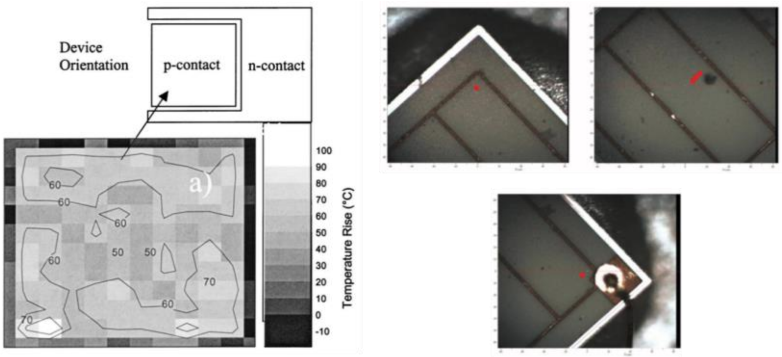

(a) (b)

Figure 15: (a) Micro-Raman spectroscopy temperature map of the active area of flip chip UV LED driven with 50 mA input current [176]. (b) Five different laser beam focus locations over the LED chip surface for the Raman spectroscopy measurements [182].

It should be noted that both thermal and stress fields have a strong influence over the Raman frequency shifts. Meaning that the phonon shifts captured by the spectrometer may be induced by simultaneous effects of both temperature and stresses under combined thermomechanical loadings. Therefore, to reach high accuracy results, the distinction of thermal strain effects should be made for the linewidth of the Stokes shifted peak [183]. Wang et al. [184] acknowledged this issue for the T_j evaluation of an unpackaged UV LED. In their analysis, a 442 nm wavelength laser with a 5 μm spot size was used as an excitation source and the spectrometers integration time was reported to be 3 s. In order to evaluate the stress effects over the peaks, the Raman spectrum of a stress-free bulk GaN wafer was also analyzed. Their findings have shown that the E_2 (high) Raman peak position of the LED chip was 1.8 cm^{-1} higher than the stress free GaN wafer. This upshift was mainly attributed to compressive stresses of the GaN layer grown on sapphire. To overcome this issue Raman spectroscopy findings were corrected for stress-induced shifts.

In a more recent analysis, Tamdogan et al. [182] used the Raman spectroscopy method to evaluate junction temperature of GaN based blue LED with and without phosphor coating. Experimental measurements were handled using three different laser excitation sources (532, 440, and 325 nm) with a 1 μm beam diameter and 50X objective. Five different surface locations where laser beam was focused shown in Figure 15(b). Bare and coated LEDs were driven with 150, 300, and 400 mA input currents, and Raman spectroscopy findings were compared to the IR and FVM analysis for the validation. Even though the measurement results for uncoated LED were found to be concurrent with the other measurement methods, bare chip and phosphor layer Raman emissions were overlapped for the coated LED which in fact limits the usage of the Raman spectroscopy method for the phosphor coated LED chips.

One way to overcome this issue was found to be the usage of Raman responsive microparticles. This is a common practice to broaden the applicability of the technique in which Raman active particles like anatase TiO_2 are embedded in an LED to capture temperature gradients across the surface [185,186]. The application of nanoparticles can also provide higher spatial resolutions for probing temperatures of small length scale features [187]. However, due to thermal resistance between the surface and p-n active region, TiO_2 particles spread over the LED surface only give insight into the surface temperature but are not sufficient to determine the actual T_j of the LED. A parametric summary of Raman spectroscopy based studies is presented in Table 3.

Table 3: Raman spectroscopy parameters employed in the literature for Tj measurement of LEDs. References are sorted by year. Not reported parameters are indicated by a hyphen in the table (λ: Wavelength).

Year	LED Type			λ_{Source} (nm)	Resolution (μm)
	Color	Material System	λ_{Peak} (nm)		
1999 [177]	UV	InGaN/GaN	410	514	0.7
2002 [176]	UV	AlGaN/AlGaN	324	488	-
2008 [181]	Blue Green	GaInN/GaN	-	785	-
2010 [184]	UV	InGaN/AlGaN	370	442	5
2013 [188]	UV	AlGaN/GaN MQW	-	488	1
2015 [189]	Blue	-	-	632.8	-
2018 [182]	Blue White	-	465 -	532, 440 and 325	1

2.2.4 Liquid Crystal Thermography

During the phase change of liquid crystals and at the intermediate phases where both liquid and solid molecular structures exist [190], light reflection shows distinct behaviors at specific temperatures [191]. Considering this temperature sensitivity, liquid crystals can be applied over the surface of the device, and reflections at unique wavelengths and colors can be used to assess surface temperatures [192]. The selection of suitable liquid crystal compounds is determined by the transition temperature between phases. Commercially available liquid crystals enable temperature profiling between the range of 30 °C to 120 °C with 0.5 °C to 30 °C increments [193,194]. For reference, a typical experimental measurement arrangement of the liquid crystal thermography method is depicted in Figure 16.

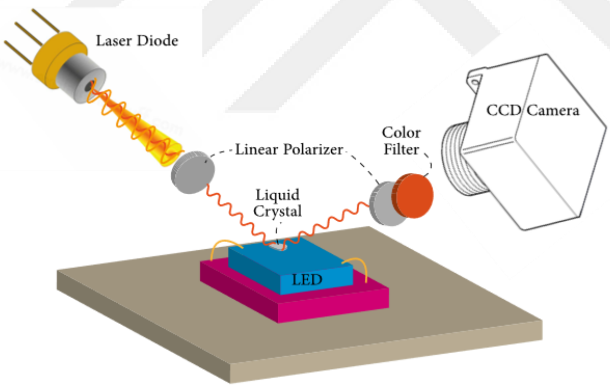

Figure 16: Schematic of the experimental arrangement of the Liquid Crystal (LC) thermography technique. Test setup typically composed of polarized laser beam, charged coupled camera with color filter and liquid crystal coated over the LED surface.

Lee and Park [195] were among the first to use nematic crystal thermography for temperature measurement of visible LEDs. Liquid crystals with transition temperatures of 302 K, 313 K, 331 K, 356 K, and 380 K were applied over the LED chip, and a red filter was used to reduce LED's optical power which can otherwise overwhelm the reflected light from the chip. A high power 660 nm laser beam was used as the illumination source since the chip is transparent to this wavelength and it was ensured that the laser beam did not heat up the device. Due to the blockage of LED light, the authors suggested the usage of transparent high-power laser for accurate spatial temperature measurements. It was seen that, at the temperatures above the transition temperature, liquid crystal changed from anisotropic to isotropic medium and that region appeared as a dark gray under microscope image. Even though, authors were able to reach 21 μm and 35 μm resolutions, the temperature measurements zones were limited to transition temperatures of the liquid crystals. In a similar procedure, Hwang et al. [196] used the liquid crystal thermography technique to observe local hot spot zones in GaN based blue LED chip with a size of 330 × 330 μm^2. For the measurements, a liquid crystal with a 29 °C anisotropic-isotropic transition temperature was used and localized hot spots of 80 μm and 400 μm size were observed.

The spatial resolution of liquid crystal thermography can be extended to 2 to 4 μm and can be less expensive than other optical probing methods, however, the uniformity and thickness of the liquid crystal can affect its accuracy and resolution [116]. Therefore, temperature errors caused by the heat spreading and temperature profile distortion should be taken into account during the measurements. Although high spatial resolutions can be reached with this technique, it can only detect local hot spots over the LED surface but not the actual T_j. It can be seen that due to the complexity of the experimental setup, coating difficulties, and uncertainty of its thermal effects, liquid crystal thermography is not a common LED junction temperature measurement technique.

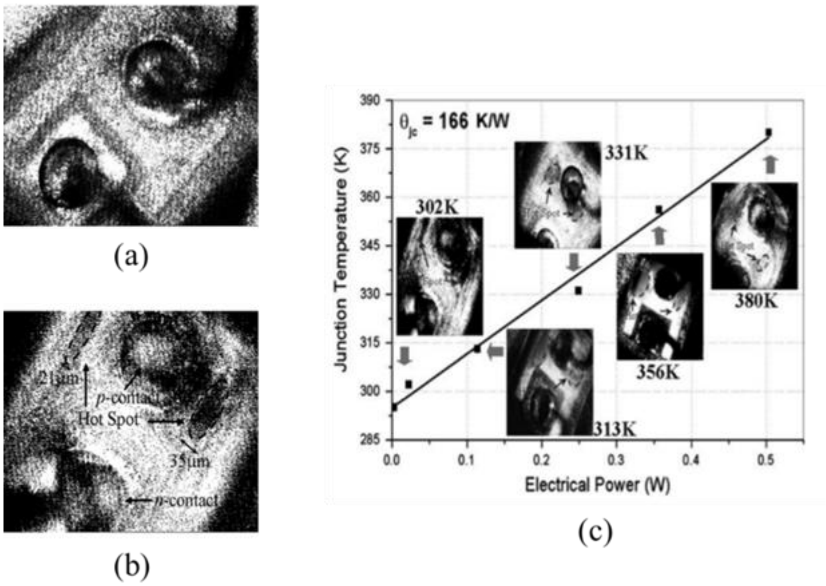

Figure 17: Liquid crystal temperature measurement of an LED (a) image before and (b) image after 22.4 mW electrical power applied. Hot spots become visible in part b when LED temperature reaches to transition temperature of the liquid crystal (c) temperature measurement results obtained using liquid crystal with different transition temperatures [195].

2.3 Temperature Sensitive Electrical Parameters (TSEPs)

Similar to the TSOPs based methods, semiconductor T_j measurements can also be performed via exploiting electrical sensitive parameters (TSEPs) of the device under study. Typically, temperature measurements with TSEPs are comprises of two stages. First, the TSEP response of the device is calibrated at different temperatures. To perform the calibrations, an external system like an oven, a dielectric bath, or a thermally controlled hot plate are generally employed to heat the device while the change in TSEP is measured. Then, in the latter stage, the relationship formed in the calibration phase is utilized to determine the actual T_j at operational current levels. The main advantage of the TSEPs based methods is that measurements can be made on fully packaged devices without a need to remove any package component for visual or mechanical access to the chip [197] or in most cases, require no addition or modification to the device's configuration. However, spatial resolution of TSEPs based methods is unclear and mainly rely on the spatial distribution of the TSEP characteristic of the device. In addition, non-isothermal distributions within the device may introduce additional errors due to averaged measurement values. Forward voltage, threshold voltage, leakage current, gain, and resistance are the most common TSEP used to measure the temperature of semiconductor devices. Since the forward voltage (V_f) is the most common and preferred technique to determine the T_j of LED, it has been reviewed individually in the upcoming *Forward Voltage Method (FVM)* section. Compared to the FVM, there are only a few other TSEP based temperature measurement methods in the literature specifically employed for the LEDs and they are discussed concurrently under the section named *Other TSEP Based Methods*.

2.3.1 Forward Voltage Method (FVM)

LED product manufacturers and researchers generally prefer the well-known forward voltage method (FVM) for T_j estimation of LEDs. Whether it is phosphor converted LED [182], multi-chip configuration [198], or a LED lamp [199], FVM is shown to be a promising approach to estimate the temperature of the active region. Therefore a number of examples of FVM for T_j evaluation of LED devices can be found [75,200,201]. Notably, claimed accuracy of this method ranges from ±3 °C [87,105] to ±0.88 °C [202].

FVM exploits temperature dependence of the forward biased diode's voltage through passing a constant current through the LED and monitoring voltage flow across the diode. A typical forward current-voltage characteristic of an LED is represented in Figure 18. Plotted current-voltage curve is comprised of three regions. Low-current section (see region (a) in Figure 18) represents the region where current-voltage behavior is dominated by the trap-assisted tunneling or defect assisted carrier leakages (Perlin et al. [203] broadly discussed the dominancy of carrier transport by tunneling across the active region and readers can refer to their study for more information about the topic). As the voltage increases, an exponential in current can be observed (see region (b) in Figure 18) which is dominated by the radiative recombination. Finally, when the voltage exceeds a certain limit (e. g 2.5 V for blue LED), deviation from exponential behavior is observed (see region (c) in Figure 18) due to the increased role of ohmic series resistance.

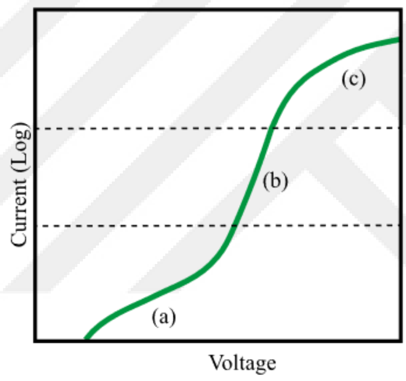

Figure 18: Typical semi-log forward voltage behavior of an LED.

Exponential behavior observed in the region (b) in Figure 18, where a small increase in the voltage result in a significant current flow in the diode, brings the opportunity of recording voltage values that can change with temperature with very small pulse currents (to avoid thermal perturbation). Within the exponential current interval, researchers are finding a linear relationship between V_f-T_j with a slope that is dependent on the drive current. In the study of Keppens et al. [204], the theoretical base of the linear behavior is well discussed. In some cases, due to fault in connections to the p-n junction, higher series resistance, or low quality of heterostructure manufacturing, the current interval in the exponential region cannot be achieved. This issue can block the possibility of calibration with low currents or achieving a meaningful relationship from the calibration.

Typically, the calibration process should involve short periods of pulses since heat can be still generated when the device is electrically active to non-radiative recombination, radiation absorption and Joule's heating in the LED [36]. Therefore, applied pulse values and durations should be selected such that heat generation in this period does not interfere with the calibration process [88].

In one of the earliest attempts, Xi and Schubert [205] developed an expression for the T_j-V_f relation and showed that constant values for the temperature coefficient of -2.3 mV/K at a temperature range of 20-120 °C exist for the studied GaN based UV LED. This is known to be the first study that investigated the dependence of junction temperature on operating voltage for GaN LED grown on a sapphire substrate. Furthermore, Jiang et al. [206] were the first to report of T_j characteristics of GaN based blue LED on Si substrate. In their study, constant temperature coefficient of -3.0 mV/K at temperature range of 30-90 °C was recorded. When compared to LEDs on sapphire, T_j was found to be much lower which was mainly attributed to the thermal conductivity difference of Si and sapphire. Meyaard et al. [207] looked at the temperature coefficient of GaInN LEDs from 80 K to 450 K and found two-slope characteristics for T_j-V_f temperature coefficient of -8 mV/K from 80 K to 100 K and -1.7 mV/K from 200 K to 450 K.

In recent studies, it has been claimed that the constant temperature coefficient voltage assumption for FVM is not always accurate. Onwukaeme et al. [208] investigated T_j of GaN based blue LED using non-linear dependence of V_f at temperature ranges of 20-100 °C. In their experiments, 100 mA pulses were used in the calibration process and quadratic fitting is claimed to be more accurate than linear fitting for temperature coefficient of voltage. The deviation reported in this research can also be seen in other studies where relatively high pulse values were used in the calibration process. [209] For instance, Kim and Han [210] investigated the T_j dependency on the heat dissipation of a GaN based blue LED by analyzing the decrease in V_f at elevated temperatures. FVM was employed to determine T_j and LED was calibrated by applying 5 mA current for 10 ms. In their analysis, deviation from the linear behavior was observed above 125 °C and cubic polynomial was found to be the ideal fit to characterize the relation at high temperatures. Linear deviations in high pulse values can be attributed to junction heating that leads to calibration of the V_f to a higher T_j. In high temperatures thermal droops also increase in the LEDs which indeed intensify the self-heating of the LED [211–214]. In low temperatures, deviation from the constant voltage coefficient of temperature can be explained by internal series resistance [204]. However, at low pulse durations, which ensures no T_j rise [88] and falls into the exponential current interval (e.g 1 mA), numerous perfectly linear T_j-V_f were reported in the literature [89,105,113,115,135,150,182,202,215,216].

With the rapid growth of LED products, FVM based commercially available test systems for their thermal investigation became available. One well-known measurement equipment that utilizes FVM is the commercially available transient thermal T3ster [217]. Measurement with T3ster equipment comprises both hardware measurements and software calculations in compliance with the JEDEC standards [218–220]. The equipment is capable of recording the dynamic temperature responses with submicron time resolution via single or multi-port measurements. In addition to T_j evaluations with respect to the V_f drop across the p-n junction region, the heat flow path from device to the ambient and thermal resistances can be measured.

Yang et al. [221] used the T3ster measurement system to determine T_j and thermal resistance of a PAR 38 light bulb. In their analysis, k-factor (temperature coefficient of voltage) calibrations were made when LED was driven with 1 mA bias current and ambient temperature was changed from 25 °C to 85 °C. Correspondingly, nearly linear V_f-T_j relationship was realized with a 5.97 K/V calibrated k-factor and further thermal characterizations were made for 36 mA operational current. In another study of Yang et al. [222], thermal resistance measurement of an LED module was made using T3ster. In experiments, LED was driven with 3.2 W input power and the overall thermal resistance of the module was found to be 4.10 °C/W and 9.18 °C/W for two different heat pipe substrates. Based on the instrument specifications and measurement conditions, the uncertainty of the thermal resistance measurement with T3ster system was found to be 11.3%. Liu et al. [223] used T3ster combined with an integrating sphere to evaluate the T_j and thermal resistance of a blue LED mounted on an aluminum plate. For the measurements, the time of the test system delay was set to 1 μs with a temperature measurement accuracy of 0.01 °C. A linear relationship between V_f-T_f was formed with a value of -1.043 mV/°C. LED was driven with 300 mA input current for 60 s at 25°C ambient temperature while sensor current was 10 mA for 100 s. As a result, T3ster T_j calculations and simulated T_j values showed similar trends with a nearly 1 °C difference.

Yang et al. [224] measured T_j and thermal resistance of an organic light emitting diode (OLED) using T3ster. During the k-factor calibrations, OLED was driven with a 1 mA sensor current at a temperature range between 15-55 °C with 5 °C temperature interval. A linear relation between V_f and T_j was verified with k-factor of a -0.023 mV/°C. According to their thermal characterizations, the thermal gradient between T_j and case temperature was found to be within 14.5 °C when OLED was driven with 120 mA input current with an optical efficacy of 18.3 lm/W. Further examples of using T3ster can be found in a number of studies [108,124,130,225–228].

At JEDEC JESD51-51 [218], it is stated that to perform k-factor calibration, an isothermal environment is required. Concerns exist about the accuracy of thermal equilibrium of the commercially available temperature measurement systems during the k-factor calibration process. Typically to achieve a thermally equilibrium and to obtain corresponding V_f, LEDs soldered on a PCB were mounted on a thermal controlled heat sink. Then the heat sink temperature was set to a pre-defined measurement value. In these configurations, non-isothermal environmental conditions, or thermal resistance difference between thermocouple and LED may cause calibration inaccuracy [49]. This concern is also recently pointed out by Hantos et al. [209] in the framework of Dephi4LED project [229]. As mentioned by the authors, when attachment on temperature controlled heatsinks is used, heat transfer toward the air builds up a parallel heat-flow path which disturbs the accuracy of the k-factor calibration and the same issue in the test phase exists.

During the conventional FVM calibration process, desired “n” pulse temperature ($T_{p,(1,\ 2,\ \ldots,\ n)}$) should be kept constant for several minutes to perform “m” number of pulses ($P_{1,\ 2,\ \ldots,\ m}$) with a control interval in between each pulse (t_o). Oven insulation and active heater controls are commonly used to maintain equilibrium condition for measurement ranges. Even though, the isothermal condition can be more accurate at temperatures near to the room temperature, heat dissipation from the oven and air motion inside the oven increases temperature fluctuations and thermal resistance between calibration thermocouples and T_j increases. To ensure pulse current temperature to be equal to T_j, oven arrangement as configured in EVAtherm system can be used [50,115,135,150,201] in which LED placed at the middle of a thermally controlled oven with no direct contact between the heater embedded walls. In this configuration, several thermocouples record the air temperature and PCB to increase the speed and accuracy of the isothermal condition. In addition, fins can be used to suppress the air motion and increase the thermal uniformity. Thus, thermal resistance difference and radiation heat transfer issues can be controlled and T_j at the desired temperature can be achieved with more assurance.

Figure 19 compares experimental parameters from different research groups that performed FVM calibrations in a concise manner.

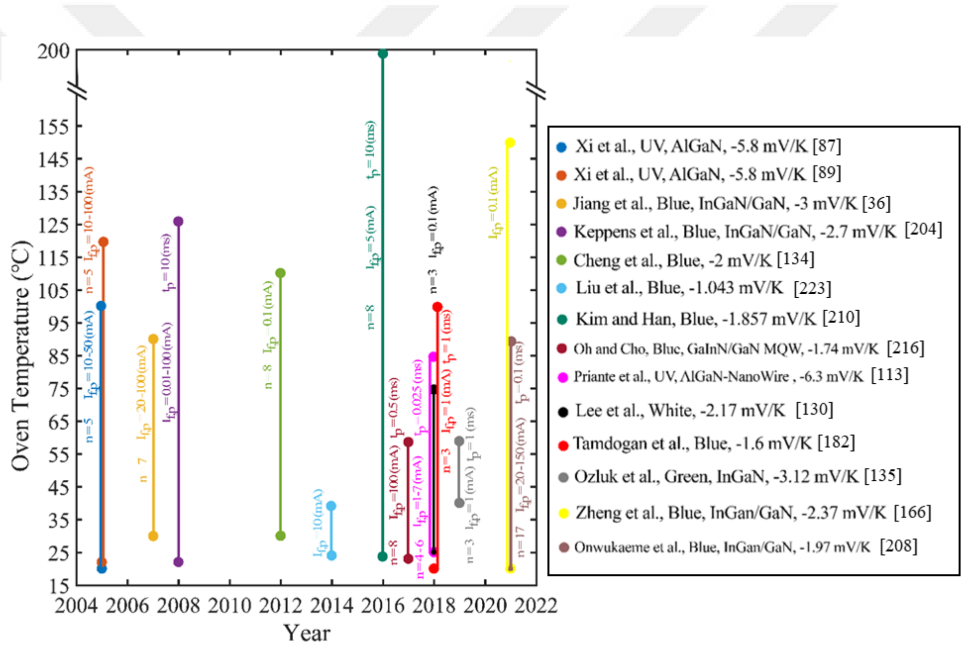

Figure 19: Yearly summary of the employed oven temperature ranges for the calibration of FVM from different research groups. $I_{f,p}$ represents the applied pulse current in mA, t_p represents the duration of the applied pulse current in ms and n stands for the number of temperature points set for the calibration measurement within the given oven temperature interval. Legend provides author indication (oldest to most recent from top to the bottom), studied device types, and k factors obtained from the pulses with minimum value of $I_{f,p}$. Each colored line indicates the temperature difference between $T_{p,1}$ and $T_{p,n}$.

Table 4: FVM parameters employed in the literature for T_j measurement of LEDs. References are sorted by year. Not reported parameters are indicated by a hyphen in the table ($I_{f,p}$: Pulse current, $t_{p,max}$: Maximum pulse duration time, V_f: Forward Voltage and Δδ: Uncertainty).

Year	Color	Material System	Temperature Coefficient of V_f (mV/K)	Behavior of V_f-T_j	$I_{f,p}$ Range (mA)	$t_{p,max}$ (μs)	Operating V_f (V)	Δδ (K)
2005 [87]	UV	AlGaN	-5.8	Linear	10-50	-	5.2-7.7	3
2005 [89]	UV	AlGaN GaInN	-5.8 -2.3	Linear	10-100	-	-	3
2006 [206]	Blue Blue	InGaN/GaN InGaN/GaN	-3 -2.7	Linear	20-100	-	-	-
2008 [204]	Red Red White Green White Blue White Green White White	AlGaInP AlGaInP - InGaN MQW - InGaN MQW - InGaN MQW - -	-3.391 -2.998 -2.219 -1.767 -1.742 -1.653 -1.648 -1.466 -1.423 -1.263	Linear and Non-linear	0.01-100	10000	3.408 2.58 3.246 2.77 2.98 2.981 3.017 2.541 2.982 2.887	-
2012 [134]	Green Blue Red	-	-2.714 -2 -1.714	Linear	0.1	-	2.39-2.58 2.32-2.46 1.54-1.66	4.8 4.3 3.9
2013 [207]	Blue	GaInN	-1.7	Linear and Non-linear	-	-	-	-
2014 [223]	Blue	-	-1.043	Linear	10	-	-	0.01
2017 [216]	Blue	GaInN/GaN MQW	-1.74	Linear	100	500	2.86-3.2	-
2018 [113]	UV UV	AlGaN-NanoWire	-6.3 -5.2	Linear	1	25	-	-
2018 [130]	White	-	-2.17	Linear	0.1	-	-	-
2018 [182]	Blue White	-	-1.6	Linear	1	1000	2.45-3.5	-
2019 [135]	Green	InGaN	-3.12	Linear	1	1000	2.328-2.395	2.3
2021 [166]	Blue	InGan/GaN	-2.37	Linear and Non-linear	0.1	-	-	-
2021 [208]	Blue	InGaN/GaN	-1.97 to -4.34	Non-linear	20	100	-	3
2021 [230]	White	-	-1.58	Linear	0.1	-	-	-

As shown in Figure 19, a wide range of pulse current ($I_{f,n}$) values was reported while only few authors provided pulse duration ($t_{p,n}$) values. It can be seen that, in general, only a few pulses are performed, and the value of “n” rarely exceeds 10. This issue arises from hardship and time-consuming process of achieving thermally equilibrium condition. Initial temperatures are mostly adapted near the room temperature however consistency in the value of maximum temperature cannot be seen. Interestingly these inconsistencies in experimental parameters have showed their effect on behavior of voltage-temperature which can be seen in more detail in Table 4 where experimental measurement parameters employed in various FVM based LED thermal characterization studies are summarized.

2.3.2 Other TSEP Methods

Despite the fact that FVM can be used by an arrangement to measure the T_j of AC LEDs [231], Zhu et al. [232] introduced a new method for AC LED T_j measurement. In this method, a periodic bipolar voltage pulse signal was applied as an input while the amplitude of the output current was calibrated as a temperature sensitive parameter. The accuracy of the measurement was tested via direct thermocouple chip measurement, and 1.2% relative deviation was observed between these measurement methods. Other TSEPs methods, such as the threshold voltage method for AC LEDs [233] and low forward current method [234] can also be found in the literature. For instance, Zhao et al. determined the resistance of n-GaN layer as a function of temperature and used this relation to evaluate the T_j of a blue LED. Electrodes of the chip were attached to the voltmeter with ohmic type connectors and the chip was calibrated with 5 mA for 0.5 s pulse currents at 20-195°C ambient temperatures. Experiments were repeated for five LED dies from the same batch to ensure the consistency of measured data and interval shift of 0.1 Ω for separation of the mixing curves. The accuracy of the method is claimed to change between ±3 °C to ±1 °C for T_j, increasing from 30 °C to 120 °C. Validation of the temperature dependent resistance method with FVM has shown that the proposed technique is a promising approach for the measurement of LEDs. Wu et al. [235] proposed an interesting approach to avoid heating during pulse current calibration of TSEP. Instead of forward voltage, authors suggested the usage of temperature dependent reverse current to determine T_j of InGaN based blue LEDs. In addition to the prevention of excess heating in pulsed condition, the authors have pointed out that the reverse current method is more sensitive to the temperature variations than the FVM which can enhance the signal to noise ratio measurements. However, research community favors forward current instead of reverse current for calibration and information on the practicality of the reverse current method is scarce.

2.4 Other Approaches

2.4.1 Thermocouple Thermometry

Thermocouple thermometry is a widely used contact temperature measurement technique that relies on an intrinsic thermoelectric phenomenon known as the Seebeck effect. In basic explanation, an electromotive force is generated when the two ends of the thermocouple experience a temperature difference, and the resultant voltage difference between the measurement and the reference junction point can be evaluated to probe the temperature of an unknown point [236]. The usage of passive thermal temperature sensors for thermal characterization may be the simplest and the cheapest amongst other measurement approaches, however, thermocouples cannot be utilized for direct T_j measurement of LEDs since they cannot reach the active area. Thus researchers should select another reachable point that is close to the chip (e.g surface, solder point, or electrodes) and asses the temperature based on the thermal resistance from that point to the junction region [237,238] (refer to Figure 7).

Jung and Lee [239] implemented the solder temperature measurement technique to analyze the heat dissipation performance of an LED headlight and evaluated the junction to solder point resistance ($R_{j\text{-}sp}$) as 1.7 °C/W. In their analysis, T-type thermocouples were attached to the solder point of the LED chip, and soldering point temperature (Ts) at thermal equilibrium was recorded as 62.8 °C. From solder point temperature measurement analysis, T_j was calculated to be 103.6 °C which was found to be 6.4 °C less than the FE analysis. Song et al. [240] determine the T_j of CREE XR-E LED mounted on a thermoelectric cooler using solder point temperature measurement technique. A T-type thermocouple was directly mounted on the solder point surface, and $R_{j\text{-}sp}$ of the LED was assumed to be 8 °C/W which was taken from the manufacturers' datasheets. As a result, T_s was found to be changing between 65-125 °C with a constant interval of 15°C for input currents ranging from 300 to 1000 mA with constant interval of 100 mA. In another study, Faranda et al. [241] tested the heat dissipation performance of refrigerating fluid on a fabricated LED prototype by analyzing the decrease in T_j of COB white LED. Thermal resistance from the selected measurement point to the junction was given as 6.5 °C/W and measurements were carried out with a FLUKE 54II thermometer and a temperature sensor. T_j was found to be changing between 50-56.5 °C and 110.7 °C-123.2 °C for different refrigerating liquid levels. In a more recent study conducted by Rammohan et al. [242], T_j of high power LED array was determined using solder point temperature measurement technique. K-type thermocouples were attached to the solder points of each LED, and total $R_{j\text{-}sp}$ of the LED array consisting of 6 high power LEDs was given as 2.75 °C/W at 31 °C ambient temperature. Experimental T_j values were found to be ranging between

45 to 85.5 °C for different input power and ambient conditions. Correspondingly, the authors have concluded IR based temperature maps are in agreement with the reference numerical work findings and solder point temperature measurements.

Direct attachment of a thermocouple tip onto the new generation micro/nano scale electronic devices is a handicap [243] and special care has to be taken while preparing a functional setup that can probe temperature in small features. Nowadays, thermocouple detectors manufactured through lithography and vapor-deposition are gaining popularity for thermal characterization in micron and nano scale electronic devices [244]. A thermocouple probe with junction size as small as 100 nm^2 may be produced with above mentioned techniques for use in the electronics industry [245]. However, prior fabrication of electric connections with external circuits onto micro-LEDs is required to perform temperature measurements with miniaturized thermocouples. Correspondingly, precise implementation of micro-thermocouples to the device is considered a time-consuming approach. It is only ideal for one-time measurement of a few discrete points rather than thermal probing on a regular basis. Nonetheless, LED temperature measurement with micro-nano size thermocouples and microsensors has been exercised by several researchers.

Shih et al. [246] micromachined monolithic thermocouples with 78 μm and 118 μm probe sizes for electrical and thermal inspection of micro-LEDs. Mechanical tests verified that probe tips can exactly contact the micro-LED electrodes with low contact forces, and consequently, thermal, and electrical properties were successfully determined. Micro thermocouples were also adopted in the study of Xiao et al. [163] and it seems that due to the direct covering of the surface of the LED, light absorption both at the surface of the thermocouple and LED or light reflection back to the active region resulted in the over estimation in temperature findings. Although the authors claimed that a 200 μm diameter thermocouple surface is barely affected by the incident or reflected light, the effect of light emission blockage on the LED itself was not discussed. In a more recent study, Choi et al. [247] first time fabricated a Pt based microscale resistance temperature sensor with lift-off process and embedded the sensor onto an SMD-LED package for T_j measurement. Compared to the unstable micro thermocouples, the stationary position of the developed Pt sensor claimed to be minimizing error by providing simple and reliable thermal characterization. Even if a good agreement between microsensor measured T_j temperature of the SMD-LED and numerical and structural thermal analysis was observed, prior calibration of the temperature coefficient of the resistance of the Pt microsensor via another reliable measurement approach is still required for accurate thermal characterization.

Overall, the usage of thermocouples for temperature monitoring is relatively straightforward. They provide rapid response, easy maintenance, and cost-effective solution for many applications. However, T_j measurements with thermocouples are highly dependent on the thermal resistance from the measurement point to the junction point. Generally, those values are acquired from manufacturer datasheets that represent average resistance values only and the additional contact resistance between the tip of the thermocouple and the point of interest is generally ignored. The solder point temperature technique is only applicable for simple LED configurations in which the LED is solely mounted over PCB. In most cases, reaching the solder point of complex LED packages and lamps is a challenging process, and soldering or usage of adhesives to attach thermocouples to joint points can damage the package integrity and decrease the accuracy of the technique. The spatial resolution and response time of the thermocouple thermometry method are limited by the probe size and thermal capacitance of the thermocouple respectively. Moreover, light absorption-induced thermocouple self-heating due to local luminance cannot be disregarded since it might lead to the overestimation of T_j during operation [248].

2.4.2 Magnetic Nanoparticle Thermometry (MNPT)

In recent years, imaging of magnetic nanoparticles at molecular concentrations for non-invasive temperature measurements has been emerging in micro and nanoscale thermal investigations [249–253]. Magnetic nanoparticles are superparamagnetic substances that have temperature sensitive magnetization curve that allows them to be used for nano-second resolved internal temperature probing. Even though magnetic nanoparticle thermometry (MNPT) usage is currently more common in biomedical and biological applications, Hu et al. [254] employed the MNPT technique to determine the heating and cooling characteristics of LEDs. In their analysis, the blue LEDs' chip surface was coated with a layer of MNP and an AC magnetic field generator and magnetic field detector were used to excite and collect signals from the sample. Particle influence over the light extraction was tested with an integrated sphere system to ensure that MNP, does not alter the optical performance. One to one mapping relation between the magnetization intensity and temperature was formed according to the Langevin equation. Before the LEDs' thermal analysis, the system was calibrated with thermocouples and ferrofluid sample whose temperature is known. According to the first and third magnetic field harmonic responses, LED temperature was recorded to be 31.2 °C, 41.3 °C, and 53.8 °C when operating at 25 °C ambient temperature and under 5.0 V, 5.1 V, and 5.2 V input voltages. Although the proposed MNPT technique is a promising new approach in the field of experimental T_j measurement of LEDs, the technique failed to provide detailed point to point temperature profiles of the surface of the LED. Also, similar to the other measurement techniques that utilize responsive particles and coatings (Raman active particles and liquid crystals), the measured temperature belongs to the MNP layer temperature which is assumed to be equal to the LED chip surface temperature and not the actual LED T_j.

In summary, the influence of the thermal issues is preventing LEDs from reaching their true potential. Especially generated heat in the p-n junction region is a direct indicator of poor performance that results in a decrease in radiant flux, light quality, efficiency, and reliability. Considering the challenge for the development of an adequate cooling architecture, interpretation of photometric characteristics and package capabilities to overcome the thermal issues, it is of fundamental importance to accurately determine T_j in the actual operating environment. Correspondingly, above given critical review, summarizes large number of experimental LED T_j measurement approaches to address the measurement principle, accuracy and applicability of the methods for various types of LEDs. In addition to the critical discussion provided, possible problems one may experience with each measurement approach are also explored to introduce a helpful guideline for experimental research for LEDs.

CHAPTER III

EXPERIMENTAL STUDY

In this chapter, number of experimental studies conducted are presented. In the first section, an improved FVM is introduced for dynamic performance evaluation of the LED. Thermal, optical, and electrical measurement of bare chip is presented in the second section. Following that an immersion cooling technique is demonstrated for the preparation of the LED packages. Particle based investigations are done in the final section and detailed discussion are provided at the end of the chapter.

3.1 Dynamic Temperature Sensitivity Measurements

3.1.1 1st Step: Calibration of I-V Characteristics

Different from other TSEP based measurement approaches, a more accurate and time efficient FV measurement technique was introduced and adopted within the scope of this thesis. To better understand the differences between the conventional and the introduced FVM, a schematic of the calibration of the transient electrical and thermal parameters are shown in Figure 20.

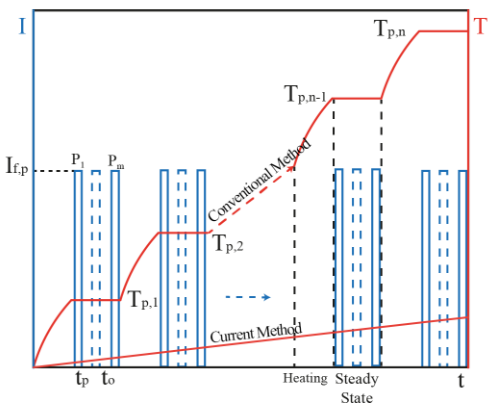

Figure 20: The calibration procedure for the forward voltage technique. The schematic provides a comparison for the current and conventional oven temperature measurement method.

In a typical FVM measurement, the device under test is heated to a chosen pulse temperature ($T_{p,(1,\ 2,\ \dots,\ n)}$) in the thermally controlled environment and after the temperature of the junction and ambient reaches thermal equilibrium (this is ensured by keeping T_p constant for a decision time), current and voltage characteristics are measured in “m” number of pulses ($P_{1,\ 2,\ \dots,\ m}$) with a t_0 time interval in between each pulse. After each T_p has reached the steady state temperature, a constant pulse forward current ($I_{f,p}$) value is applied for a low enough pulse duration (t_p) time to avoid any self-heating while adequate enough to make corresponding pulse voltage ($V_{f,p}$) readings.

As covered in Chapter 2, test environment’s ability to reach thermal equilibrium during the FVM measurements is a critical drawback. Although oven insulation and active heater controls are often used for the thermal control, the method is found to be more reliable at temperatures close to the room temperature. However, at high temperatures, heat dissipation from the oven and the air motion inside the oven increases, causing fluctuations in temperature readings and incorrect thermal equilibrium assumptions. Furthermore, in case of using thermally controlled hot plates to regulate temperature, due to the thermal resistance between the LED junction and hot plate, temperature differences significantly increase at high temperatures. This also result in inaccurate calibration of V_f and correspondingly overestimation of T_j. To avoid uncertainties associated thermal equilibrium assumption, a new thermal control solution is adapted for the accurate LED thermal characterization within the scope of this thesis.

As illustrated in Figure 21, tested LEDs attached over the heat sink are initially positioned at the center of the oven. With the help of thin, densely packed aluminum fins placed inside the oven and the air temperature near the LED chip surface was suppressed to uniform temperature. As the oven heats up to a predefined temperature point at a rate nearly +0.5 K/min, the temperature of the heatsink, LED and air close to the chip surface simultaneously measured with thermocouples to keep track on the thermal equilibrium.

Concurrently, electrical characteristics were determined by using Keithley 2602B high precision source meter which is controlled by a custom-made Test Script Processor (TSP). Depending on how long the source meter needs to read data ($V_{f,p}$), t_p was ranged arranged to be changing between 2 to 2.4 ms at most while the off interval between each pulse was set to be 0.5 s. To account for the statistical fluctuations and assure precise measurements, m = 4 pulses were performed for each T_p interval. A wide range of pulse current magnitudes ($I_{f,p}$), from 0.1 to 100 mA, were examined to determine the optimum pulse value. When compared to existing FVM applications, much higher calibration readings (n>50) can be achieved with the proposed technique while large number of data points inside the new oven arrangement (see Figure 21) ensures reliable measurements.

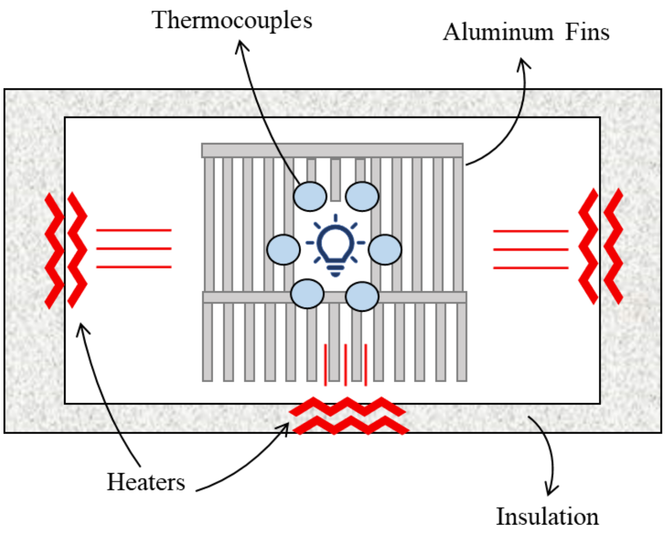

Figure 21: Illustration of the thermal environment and thermocouple arrangement of the current study.

3.1.2 2nd Step: Actual Measurement of T_j (Test phase)

As shown in Figure 22, test phase measurements were made through series of source delay measurements (SDM) cycles. For a delay time of t_c, the source output was set to a particular forward current (I_f) level throughout each cycle. The forward voltage (V_f) was then calculated with two 4-wire voltage measurements. Directly after, I_f was decreased to calibration phase pulse current ($I_{f,p}$ = 1 mA) with a delay time of t_p= 3 ms. It should be noted that t_p includes 1 ms delay and two voltage measurements each longing for 1 ms. This way, T_j can be assessed based on the calibration data and as pulse duration ends, source immediately returns to its continuous operation at a value of I_f.

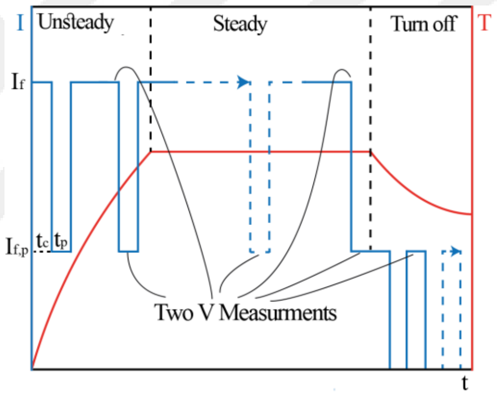

Figure 22: Illustration of the transient test phase (red line shows the trend of temperature rise of the junction).

I_f values can be selected as desired. Considering the operation range and temperature limit of the blue LED Chip (Cree C460EZ1000-0216-2) used in this study, current of 300, 500 and 700 mA were applied to the test device with and without heatsink. To evaluate dynamic temperature variation, t_c values were increased controllably. For instance, from 0 to 3rd s, t_c was set to 20 ms. After that from 3rd to 15th s, t_c was raised to 100 ms. From 15th to 75th s, t_c was increased to 1 s, and finally from 75th to 1167th s, t_c was increased to 10 s. Devices were turned off at t = 1167 s, and 122 pulses with a 2 ms delay were supplied again with $I_{f,p}$ equal to 1 mA to understand the dynamic behavior of the device after the turn off. During the test phase measurements, LabSphere Illumia Plus 610 brand integrating sphere system was utilized to record the light output simultaneously. Integrating sphere is special measurement system that is capable of measuring various optical parameters including radiant flux, luminous flux, chromaticity, wavelength (peak, center, centroid and dominant), FWHM Bandwidth, Correlated Color Temperature (CCT), Color Rendering Index (CRI). The device contains a CDS-610 model detector and 2-meter diameter sphere which was painted with reflective coating with emissivity over 0.98 [255]. Configuration of the LED within the integrating sphere system during test measurements is shown in Figure 23.

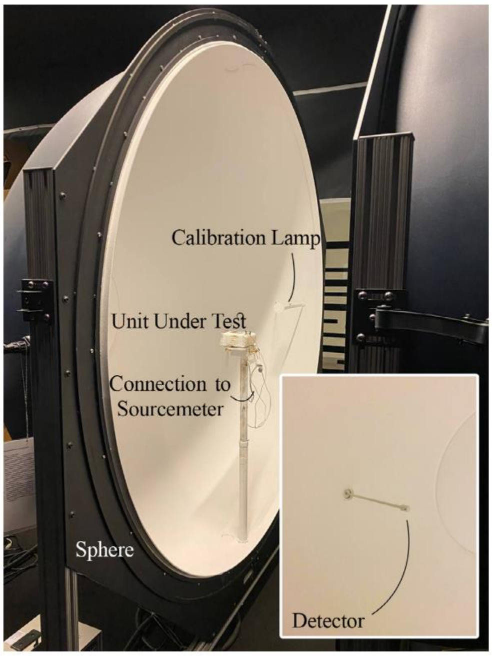

Figure 23: Integrating sphere setup with tested device positioned at the center.

Measurement time interval of the sphere and source meter were adjusted using a spline interpolation with a not-a-knot end condition. Furthermore, heat generation of the device was calculated using Equation 1 with respect to the LED's optical power (P_{out}) and V_f at the end of each continuous phase before the pulse application.

$$Q_{LED} = V_f I_f - P_{out} \quad (1)$$

As shown in Figure 22, mainly three thermal regions were expected: (1) A sudden temperature increase at the unsteady zone. (2) Steady zone where time dependence of temperature is low. (3) Turn off zone where temperature drop of the device can be analyzed.

3.2 Bare Chip Thermal Characterization

In this study, a blue LED chip (Cree C460EZ1000-0216-2) with an emission area of 0.9x0.9 mm^2 and a dominant wavelength of 462.5-465 nm was chosen. LED was mounted over a 30x30x1.5 mm^2 PCB (consist of Al base, ceramic dielectric, and copper conductive layer) with surface mount technology. For a broad evaluation of the thermal performance, LEDs were tested with two different configurations; with and without a heat sink. It is important to state that LEDs were tested in room temperature at 21°C and no active cooling was employed. Steady-state spectral distribution of the high-power blue LED chip at 500 mA is shown as representative in Figure 24. Peak, center, centroid, and dominant wavelengths were measured as 460.9, 461.2, 464.6 and 465.7 nm respectively while FWHM bandwidth was evaluated as 28.2 nm.

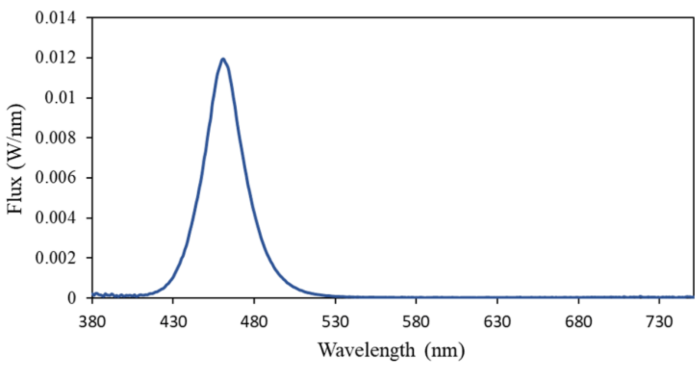

Figure 24: Spectral power distribution of a blue LED chip driven at 500 mA without heat sink.

Result of calibration experiments is depicted in Figure 25. For low pulse current values ($I_{f,p}$ = 0.1 mA), slight fluctuations for V_f responses are observed due to the carrier leakages. More detailed comparison for the linear (Eq.2) and quadratic (Eq.3) fitting of the calibration results for different $I_{f,p}$ are given in Table 5.

$$V_{f,p} = A(T_j) + B \tag{2}$$

$$V_{f,p} = A'(T_j)^2 + B'(T_j) + C' \tag{3}$$

According to the calculated sum of square errors (SSE) for both fittings, best linear fit was achieved for $I_{f,p}$ = 1 mA while best quadratic fit was observed for the $I_{f,p}$ = 10 mA for the tested LED. For the linear fit, deviation from the linear behavior was observed at high $I_{f,p}$. In addition, best fittings were achieved for both quadratic and linear correlations for $I_{f,p}$< 25 mA. On the contrary, when LED pulsed with higher forward currents, additional heat generation occurs in the active region of the LED which shifts T_j from T_p and yields to inaccurate calibration of the FVM.

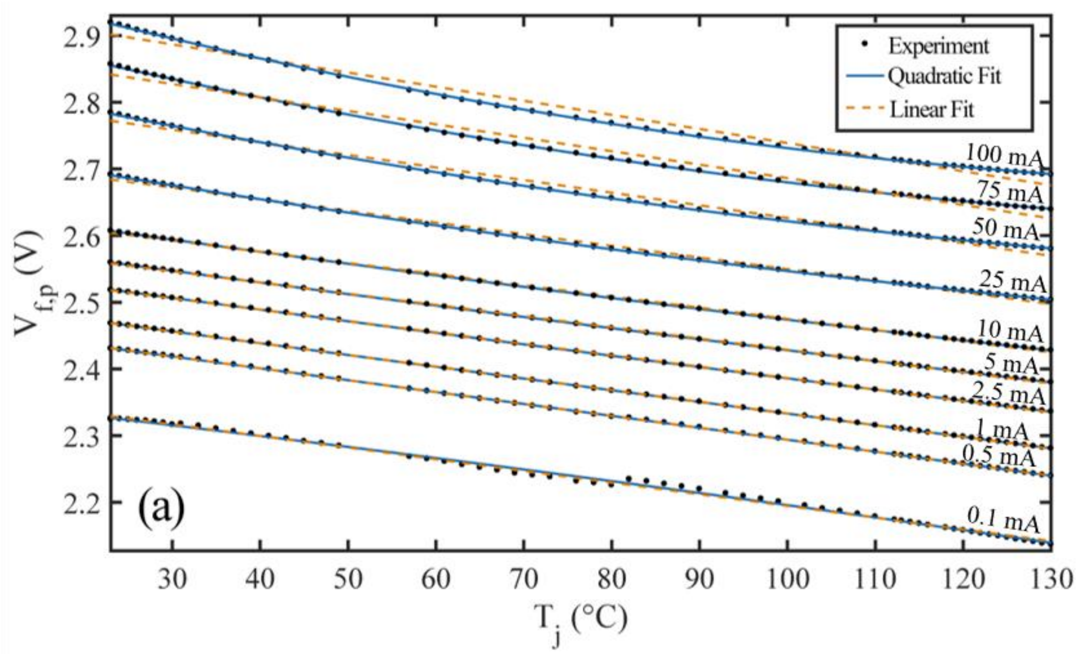

Figure 25: Calibration results for bare LED chip.

Table 5: Calibration results based on linear and quadratic correlations. Best fitting results for each correlation is highlighted.

$I_{f,p}$ (mA)	LED Linear Fit			LED Quadratic Fit			
	A ($x10^3$)	B	SSE ($x10^5$)	A' ($x10^7$)	B' ($x10^3$)	C'	SSE ($x10^5$)
0.1	-1.75	2.370	40.2	-17.9	-1.47	2.361	147.6
0.5	-1.78	2.472	9.6	-1.35	-1.76	2.472	9.1
1	-1.75	2.509	4.5	2.56	-1.79	2.510	3.0
2.5	-1.71	2.557	10.3	5.96	-1.80	2.560	1.9
5	-1.68	2.597	24.4	9.96	-1.83	2.601	1.9
10	-1.6	2.643	81.2	18.48	-1.95	2.651	0.4
25	-1.74	2.724	402.3	40.92	-2.36	2.743	0.6
50	-1.89	2.818	1131	68.64	-2.93	2.847	17.1
75	-2.01	2.888	1914	89.39	-3.375	2.928	23.8
100	-2.11	2.950	2656	105.50	-3.719	2.998	25.7

Experimental trendline of the junction temperature of the LED chip with and without heat sink is provided in Figure 26(a). As can be seen from the graph, at 3^{rd} and 15^{th} seconds, the device's temperature rise trend line shows two leaps. The first one, at 3^{rd} second, is related to the t_c increase from 20 ms to 100 ms while the second one, at 15^{th} second, is related to the t_c increase from 100 ms to 1 s. The influence of the heat sink on the transient behavior of the LED is almost negligible in the first 15 seconds. On the other hand, in low powers, heat sink is found to be effective in keeping the T_j cooler during the temperature rise. Moreover, at all power levels and after 15 s, employed heat sink was successful to keep T_j at low temperature levels.

In addition, temporal output power of the LED is shown in Figure 26(b) where optical power loss due to the T_j rise can be observed clearly. In time dependent optical study of the LED, output power determinations contained low optical powers of the pulse periods (t_c = 20 ms and 100 ms used in the first 15 s). Thus, P_{out} of the LED in the first 15 seconds is evaluated lower than the actual working condition, as light response time of the LED was effective on the measurement.

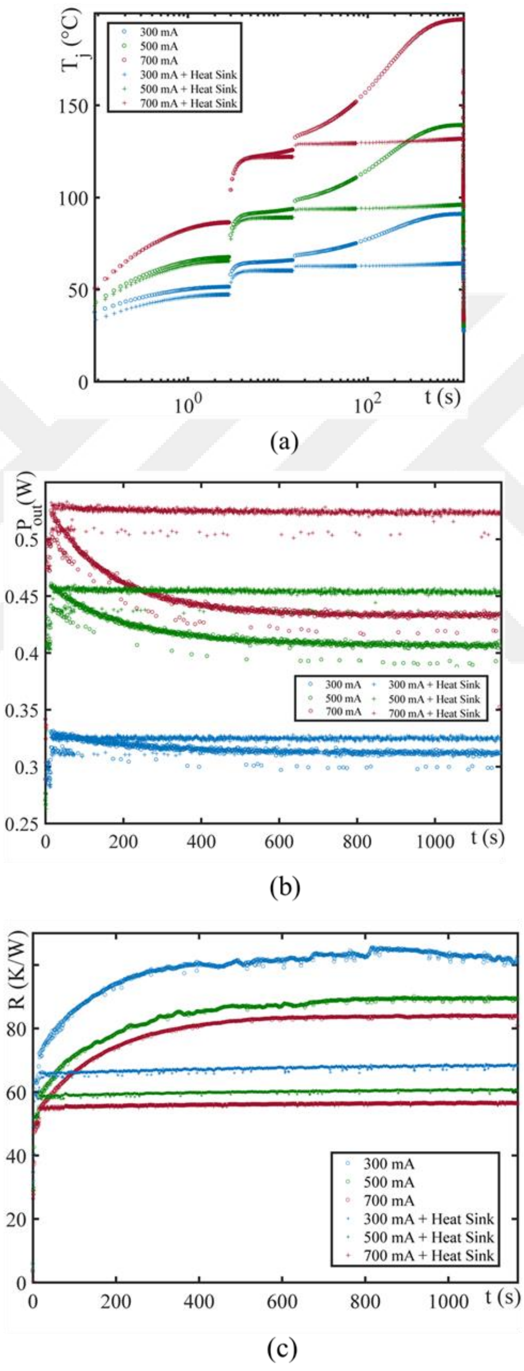

Figure 26: (a) Transient junction temperature (b) output power (c) dynamic thermal resistance of LED.

Time-dependent thermal resistance of LED is shown in Figure 26(c). As can be seen from Figure, LED's thermal resistance rises from 0 to 15 K/W between 0 to 100 ms. It is worth nothing that without heatsink, LED reaches steady state after 600 s, whereas with a heat sink, reaches to steady state instantly. The reason for the immediate T_j rise and fall of the LED can be mainly attributed to the dominancy of the spreading thermal resistance between the PCB and chip and from PCB to the heatsink. It is known that spreading thermal resistance results into higher thermal impedance.

Not only during operation but also T_j variation of the LED is investigated after the turn off. Immediately after the turn off, LED experiences a sudden temperature drop of temperature. With heat sink after 15 ms of turning of the device, T_j drops 9.4 °C, 16.5 °C, and 25.1 °C for forward currents of 300 mA, 500 mA and 700 mA. Without the heat sink, also similar junction temperature drops of 9.1 °C, 16.6 °C, and 27.8 °C are recorded. For a short period of time, the active region of the LED is lumped from other components due to the small LED chip size (950x950x170 μm^3), high thermal conductivity and sudden uniform temperature reduction. This lumped behavior continues almost for 50 ms and completely follows the lump capacitance model (refer to Eq. 4) [256].

$$\theta(t) = e^{-bt} \tag{4}$$

Independent of the applied input power, exponential fitting passed on dimensionless temperature (θ) and time (t = 0 is assumed to be the turn off) gave the same time constant values (η). According to the definition of η, heat transfer coefficient (h) of the lumped LED can be calculated as follows:

$$h = \frac{\rho c_p V \eta}{A} \tag{5}$$

Where V represents the volume of the active region while ρ, c_p and A is the density, specific heat and area of surfaces exposed to the h respectively. For the analytical calculations, thermophysical properties were taken as 490 J/kg-K for c_p [257], 6150 kg/m^3 for ρ [36] and 85 μm for V/A. As a result, h without heat sink at first 50 ms was found to be 649.8 W/m^2-K and for the system with heat sink it was evaluated as 1187.2 W/m^2-K.

In summary, above presented analysis can help to understand the significance of the temperature rise in pulse durations during the calibration phase. For instance, when temperature rise with respect to the pulse time (for pulse duration < 50 ms) evaluated using the Eq. 6, pulse currents within the range of 1 to 10 mA cause an acceptable temperature rise in all short pulse durations. On the other hand, unless it performed in 1 ms range, pulse values as high as 100 mA should be avoided due to the significant temperature rise that leads to inaccurate temperature calibrations. Notably, PCE in Equation 6 stands for the power conversion efficiency of the LED and evaluated based on the ratio of optical power output to the input electrical power.

$$\Delta T = \frac{(1 - PCE) I_{f,p} V_{f,p} t_p}{\rho A c_p} \tag{6}$$

The effect of junction temperature on normalized optical power indicates that optical power decrease is more severe at higher input powers. Yet, when PCE is plotted against T_j (see Figure 27), a different behavior can be seen. From 300 mA to 700 mA, PCE rate decreases from -0.09 %/K to -0.05 %/K. This implies that thermal droops are less severe in high current densities. Since the current densities explored within the scope of this study are close to the optimal current densities, Shockley Read Hall recombination is proportional to the carrier concentration and this recombination is low relative to other recombination processes [258]. For this reason, optical power and PCE losses are primarily associated with Auger recombination effects and reduction of thermal droops at higher current densities are explained by the temperature insensitivity of the Auger recombination [259].

The interrelations between P_{out}, P_{in}, T_j and I_f at steady state conditions are highlighted with color stripes in Figure 27. For the studied drive currents for LED, efficiency of higher than 35% cannot be achieved in useful emission power levels as Auger losses significantly reduces internal quantum efficiency and interfacial thermal resistance in thermal design prevents the application of the chip in lower temperatures. However, since the chip itself is directly exposed to the ambient, immersion cooling with high refractive index dielectric liquids can be used not only to increase the extraction efficiency, but also to significantly reduce the junction temperature [260].

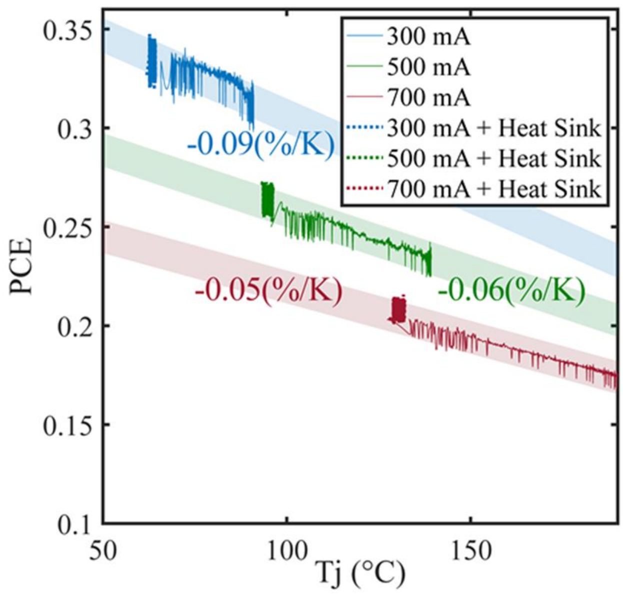

Figure 27: Variation of PCE with T_j at different operating currents.

3.3 *Immersion Cooling of LEDs with Phosphor Particles*

3.3.1 Material Properties

In this study, NuSil S-7200 [261] was chosen as an immersion fluid due to its superior dielectric strength (15.7 kV/mm) and ability to maintain thermophysical properties almost constant during the application. However, similar to other silicone-based fluids, special care should be given to the viscosity measurements since its viscosity is temperature dependent and can vary based on the batch and age of the liquid. To determine the viscosity, experimental measurements were carried out with Anton Paar RheolabQC rotational rheometer controlled by Anton Paar RheoCompass software in the device temperature range (see Figure 28(a)). Findings were compared with the results presented by Vattellie et al. [262] for 47V500 silicone oil, and close temperature dependence values were found based on this comparison (see Figure 28(b)).

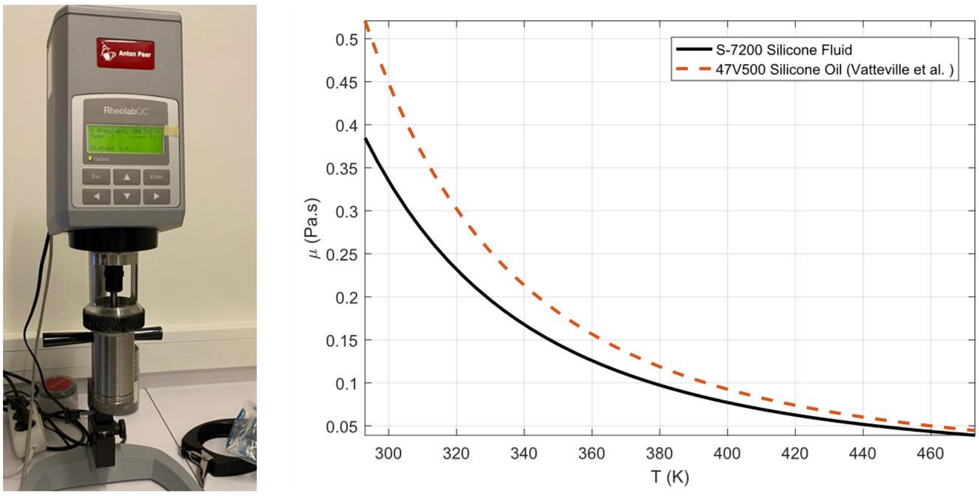

(a) (b)

Figure 28: (a) RheolabQC viscosity measurement device and experimental setup. (b) Determined best fit $\exp(b_0+b_1/T)$ for the viscosity behavior of the liquid where $b_0 = -6.96$ and $b_1 = 1760$.

As a blue light converter, $Y_3Al_5O_{12}$:Ce(2%) phosphor is selected with an excitation range of the peak at 455 nm, which is in good agreement with the chosen blue LED chip. Particle size distribution and optical performance of the utilized YAG:Ce phosphor is shown in Figure 29 based on the data provided in [167].

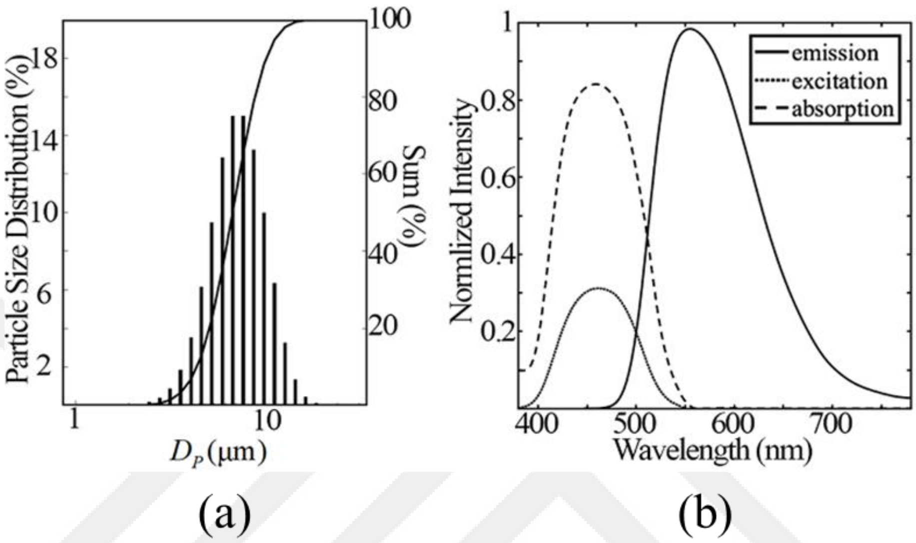

Figure 29: (a) Particle size distribution and (b) optical properties of the YAG:Ce phosphor (Optical properties are normalized in the 200-800 nm range, and data is shown in visible light range) [263].

Other thermophysical properties of the fluid and phosphor are provided in Table 6 as a reference.

Table 6: Material properties.

	ρ_f (kg/m^3)	k (W/m-K)	C_p (J/kg-K)	β (1/K)	μ (Pa.s)
Fluid	997	0.17	1460	≈0.0001	exp (-6.96 + 1760 /T [K])
Phosphor	4550	13	770	-	-

3.3.2 Test Setup Preparation

Step by step preparation of the LED chip for the immersion cooling study is shown in Figure 30. Initially, a phosphor/NuSil S-7200 fluid mixture is applied over the LED chip (Fig. 30(b)) with a controlled amount of phosphor concentration. Although there are several other ways to add phosphor particles into an immersion cooled LED package (e.g., adding phosphor after filling the dome with the immersion liquid, spreading phosphor over the LED chip without immersion liquid, or thoroughly mixing the immersion liquid and phosphor for simultaneous application), a two-step application was found to be the most suitable approach for individual particle tracking and better camera recordings. After the phosphor application, Devcon 2-Ton epoxy is applied over the joint locations of the glass dome (see Fig.30(c)). To not have an excess amount of epoxy that obstructs the view for the camera measurements, epoxy was dispensed as droplets at the edges of the dome. Following that, epoxy droplets are carefully spread all over the joint locations, and leakages were cleared out before epoxy started curing at room temperature. Immediately after, the glass dome was centered and placed over the LED package, as shown in Figure 30(d). After 8-12 hours, epoxy is completely cured, and the package was ready for immersion liquid application. As depicted in Figure 30(e), immersion liquid is poured inside the package through the hole with a needle. It should be noted that the dome is manufactured with a 2-mm hole on top to pour out the liquid safely, to have a passage for any formed bubbles to get out and measure fluid temperature during operation. After filling the dome with immersion fluid (see Fig. 30(f)), the test device preparation step is completed, and immersion cooled LED package became ready for the experimental measurements. Dimensions of the prepared LED package is summarized in Table 7.

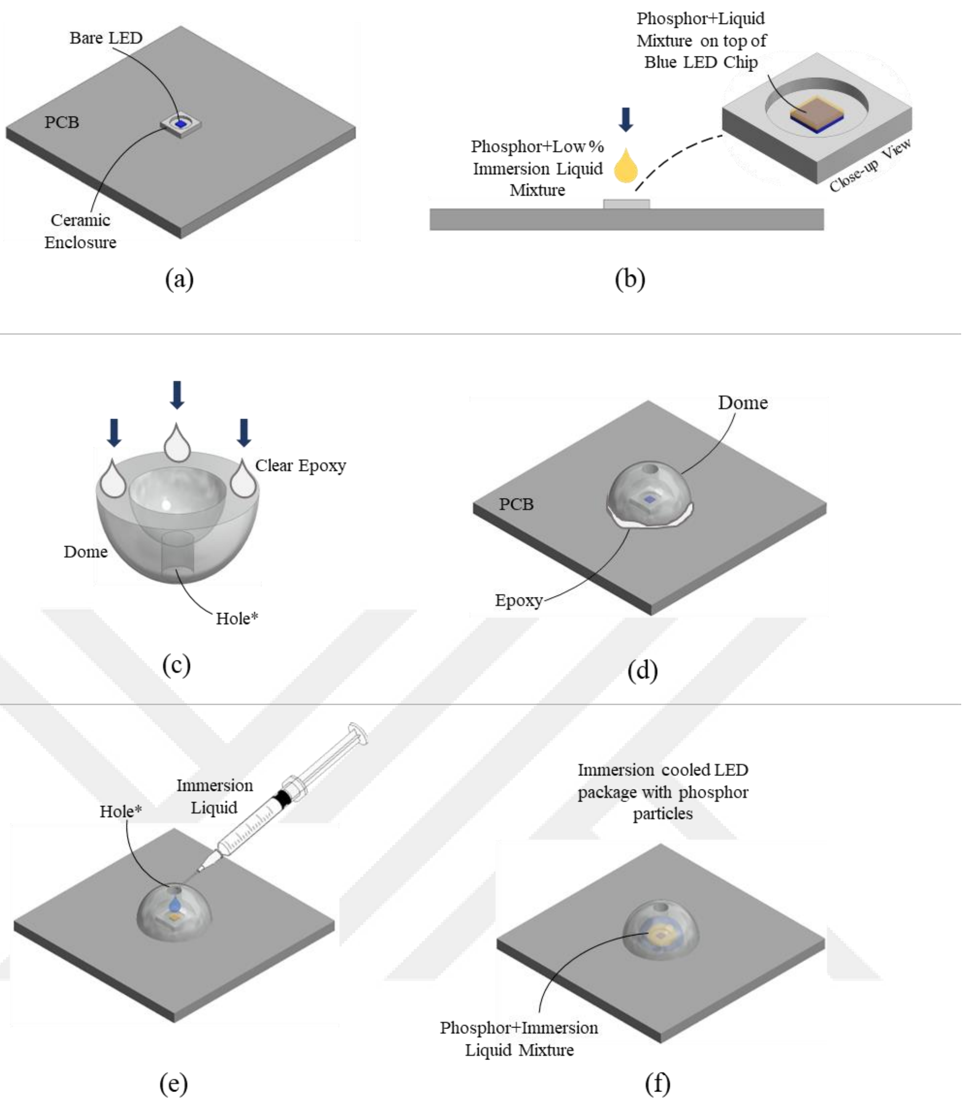

Figure 30: Step by step overview of the test setup preparation of the immersion cooled LED package with phosphor particles embedded (*A multi-purpose hole used for pouring the immersion liquid, preventing the bubble formation and for the fluid temperature measurements).

Table 7: Dimensions of the package components.

Component	Geometrical Details
Chip	0.980 x 0.980 x 0.170 mm
Ceramic Enclosure	3.5 x 3.5 x 0.71 mm
PCB	350 x 350 x 1.6 mm
Dome	Diameter: 10 mm, Thickness: 2 mm, Hole Diameter: 2 mm

3.3.3 Experimental Measurements

Experimental setup for the immersion cooled LED package was arranged such that particle and natural convection currents can be captured simultaneous with the LED T_j and fluid temperature measurements. Fluid and particle flow was monitored with Canon EOS 6d Mark II Body combined with Canon MP-E 65mm f/2.8 1-5x lens. Selected macro lens is able to record objects at up to 5x life size with high magnification and glare reflection from the package was minimized with the circular polarizer attached to it. Moreover, environmental vibrations were prevented by building the setup on an optical station with passive isolators (See Figure 31).

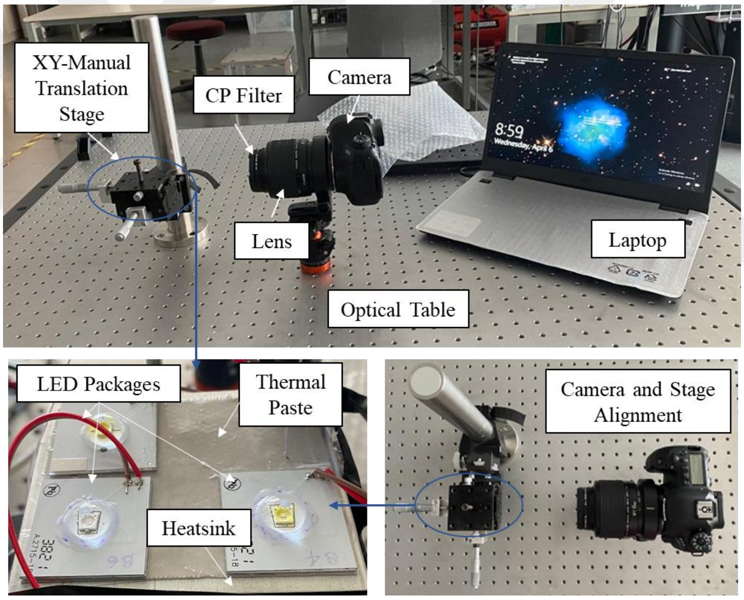

Figure 31: Experimental setup for thermal and particle-based flow investigations.

Prepared LED packages were attached to a heatsink with a thermal paste to run the LED at higher input currents safely. A heat sink was placed on top of the XY-axis manual linear translation stage which provides high sensitivity control for camera focusing. Camera was remotely controlled with the laptop through EOS Utility application to run the experiments without disturbing the predefined arrangement of the camera.

Similar to the bare chip thermal characterization, T_j of the LED was measured with FVM following the steps explained in the Section 3.1. Different from bare chip thermal characterization, this time fluid temperature was also measured to assess the temperature difference between the chip and the fluid. T-type thermocouple was placed inside the mixture domain through the 2-mm hole on top of the dome and fluid temperature was recorded during operation.

Two different LED packages were prepared to investigate the effect of particle heat generation with blue light emission: (1) Blue LED with phosphor particles, (2) Black coated LED with phosphor particle and studied cases are illustrated in Figure 32. For all cases, ambient conditions were kept identical while LED chip input current was altered to have same T_j and fluid temperature. As a result, for all test vehicles, LED T_j was set to be 100 °C while fluid temperature at the top region was measured to be 40 °C.

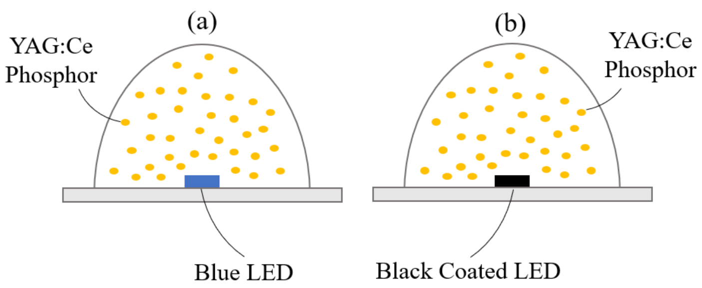

Figure 32: Schematic of immersion cooled LED packages. (a) Blue LED and (b) black coated LED.

3.4 Particle Based Investigations

For the initial case, input current of the immersion cooled Blue LED with low phosphor concentration was gradually increased to 1 A and changes in the velocity profiles were observed as the chip temperature increases. Since particle emission is stronger at higher input currents, a driving current of 1 A was selected as the test case to detect particles more clearly. At 1 A input current and at 25 °C room temperature, T_j and fluid temperature near the top dome surface of the immersed blue LED was measured to be 100 °C and 40 °C respectively. When compared to the findings of bare chip thermal analysis with heatsink attached (See Fig. 26(a)), the effectiveness of immersion liquid cooling can be clearly acknowledged. In previous analysis, LEDs are driven with 700 mA highest to not exceed the operational temperature limits and T_j was measured to be much higher than 100 °C while in this case immersion cooled LED, 100 °C of T_j was only reached when LED is driven with an input current of 1 A.

Particle tracking experiments are repeated a number of times to check the fidelity of the findings and 2 separate uncoated immersion cooled blue LED packages are tested under the same conditions. Although the findings for the two separate cases were found to be similar to each other, after a number of trials, an interesting observation was made in one of the cases. Small bubbles were observed near the chip region that cause particles to reach much higher speeds. At first the observed bubbles were assumed to be result of boiling of the silicone-based fluid. However, temperature measurements were clearly showing that the temperature within the mixture domain do not reach to the flash point of the silicone based fluid (Flash Point of NuSil S-7200 ≥ 315 °C [261]). In fact, the maximum temperature limit of the CREE LED is given to be 150 °C for a safe operation. Meaning that, it is not possible for fluid to start boiling near the chip region due to heat generation from the chip without burning the LED out. The second assumption was that fluid near the particle surface was boiling due to heat dissipation from the particle to surrounding fluid. Even though the particle light emission is the highest when particles are close to the chip this assumption cannot also be valid because in a test case prepared with TiO_2 particles that does not have a photoluminescence effect similar bubble observations were also made, proving that the bubbles are not resulting from the heat generation from the particles. Remarkably, after conducting a detailed literature review over the topic and carefully examining the experimental results, it was concluded that the observed bubbles were due to the micron scale air bubbles introduced to the mixture domain during the preparation of the immersion cooled LED package and these micron scale bubbles were being attracted towards light. Light induced manipulation of the bubbles inside the fluid were result of the change in surface tension which is known as the Marangoni effect. Despite the fact that at small scales, trapping and manipulation of soft particles (bubbles and droplets) were studied before with laser beam irradiances [264,265], millimeter scale air bubble trapping with immersion cooled blue LED is known to be a first time observation. In conclusion, the Marangoni trapping of the bubbles result in a pumping effect for particles. Phosphor particles in contact with bubble shows sudden jumps and a drastic increase in particle velocity can be seen. These findings were noted and aimed to be insightful future research that can make use of the millimeter scale bubble manipulation for different applications.

Following the blue LED analysis, black coated LED was tested to compare the particle trajectories with and without light emission. In order to have the same chip temperatures, lower input currents were employed. Considering that all the emitted light from the LED was being absorbed by the black coating, 100 °C of chip temperature was reached at 600 mA. Captured images for various immersion cooled LED packages are given in Figure 33 for reference.

The natural convection currents within the package are given as three dimensional and multiple flow loops. Since only two-dimensional visuals can be captured with the current experimental setup, location of interest for the particle tracking was from the center of the chip to middle of the mixture domain where phosphor particles were moving in the vertical direction only with no velocity component in the third dimension. Correspondingly, camera was focused to center of the chip and images were recorded for 120 seconds after reaching to a thermal steady state condition.

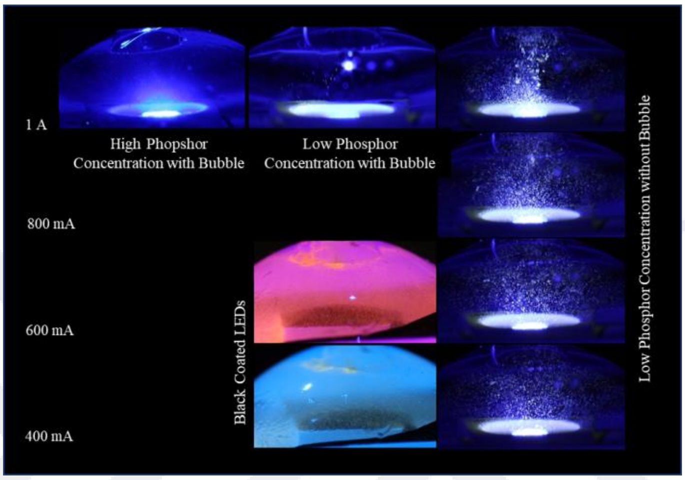

Figure 33: Captured images of the various immersion cooled LED packages.

Post processing of the videos were made in MATLAB with an image processing tool. Since the chip and ceramic enclosure dimensions are already known, pixel number of those locations were measured in MATLAB and used to evaluate the dimension of a single pixel within the image. Since the time difference between each frame is already known, by evaluating the pixel difference of one particle location to another in the vertical direction, particle velocities were determined. Table 8 summarizes the evaluated particle velocities for different cases.

Table 8: Particle velocities obtained with image processing.

	$v_{p,max}$ (μm)	$v_{p,min}$ (μm)
Blue LED (no bubble)	51.8	38.1
Blue LED (with bubble)	503	122
Black Coated LED	6.67	1.54

Post processing of the video recordings has shown a 10-fold increase in the particle velocity as a result of while light conversion, and when there are bubbles introduced to the domain, velocities are observed to be 100 times higher. The bubble induced effect is something need to be considered separately considering the scope and nature of the current project. But the critical question here is what is causing this 10-fold increase in the particle velocity when LED light is incorporated?

Regardless of the coating, heat generation from the LED causes a viscous plume, which is known to be a fluid motion caused by a continuous source of buoyancy resulting from the density change of hot fluid in contact with the high temperature body. This viscous plume rises and draws ambient fluid radially inward to mix with the higher temperature fluid inside the plume. As a result, particle trajectory within this natural convection flow is driven by the particle inertia, hydrodynamic drag, and force of gravity both with and without the presence of blue light. A slight increase in particle and fluid velocity can be expected when the particle self-heating effect is included. Yet, as discussed in the computational analysis part, this difference should be more evident for particles with a diameter higher than 25 μm, and still this increase in particle velocity can only be 1.5 or 2 times higher than the case without blue light emission. Correspondingly, there should be another force present that is increasing the micron scale particle's kinetic energy much more than expected.

In 2018, Arthur Ashkin won a Nobel prize for the invention of optical tweezers that can trap microparticles in an area with the help of an optical gradient force [266,267]. It is known that at a micron scale, gradient forces losses their significance and photopheresis force becomes a dominant effect, allowing particle manipulation using light. Generally, origin of this phenomenon is associated with a temperature gradient along the particle surface resulting from the anisotropic particle heating [268].

Even though the literature examples mainly cover the optical manipulation in aerosols [266,268], in a recent study of Zhang et al. [269] optical trapping of black particles were demonstrated in glycerol due to photopheresis induced by the laser irradiance. Surprisingly, the photopheresis was reported to arise from the momentum exchange between the liquid and solid phases resulting from the change in thermal accommodation coefficient.

Likewise, the observed variation in phosphor particles velocity with optical interaction can be related to the photopheresis force acting on the particle with light interaction either as a result of the temperature gradient along the particle surface or due to the momentum exchange between liquid and phosphor as a result of the difference in accommodation coefficient. The latter assumption is more likely to be the explanation for the given case, considering relatively high thermal conductivity of the phosphor (13 W/m-K) uniform temperature distributions can be expected across the particle surface. Although a conclusion cannot be made for the basis of the photopheresis force acting on the particle with the current setup, the resultant effect can be clearly seen with the change in the particle movement.

CHAPTER IV

COMPUTATIONAL STUDY

This chapter introduces an advanced computational model for the numerical analysis of immersion-cooled Pc-LED. In the first section, a particle-based investigation of phosphor particles is conducted with and without accounting for the self-heating effect. The thermal performance of the package, fluid flow paths, and particle trajectories are discussed to form a better understanding. In the second section, model validation is done by comparing the particle velocities obtained from the experimental and computational analysis.

4.1 Liquid Immersion Cooled High Power Pc-LED

Compared to the conventional cooling techniques including natural and forced convection over finned surfaces, making use of dielectric fluids in direct contact with a heat generating device can provide more effective heat dissipation and increased thermal uniformity in high power LEDs [270]. Tamdogan et al. [271] showed that single-phase heat transfer with cooling fluids can provide thermal performance improvements up to 60% over air convection cooling. In another study, Kahvecioglu et al. [260] showed that liquid cooling of Pc-LEDs can produce 25% enhancement in lumen output when both thermal and optical effects incorporated.

Thus, considering the improvements that direct liquid cooling can provide, inclusion of heat generating phosphor particles into an immersion cooled Pc-LED configuration can introduce a direct thermal passage for effective heat dissipation. With this objective, current study focuses on developing an advanced Pc-LED model that can overcome the thermal issues introduced by heat generating phosphor particles. This effort provides important insights about how the individual phosphor particles affect the thermal behavior of a liquid cooled high power LED package by considering the change in the thermo-optical characteristics of these particles in motion.

4.1.1 Numerical Analysis: Two phase Modeling Without Phosphor Heating

For the initial analysis, an immersion cooled blue LED package with suspended phosphor particles and cooling liquid mixture was investigated to have an insight of the thermal and optical characteristics in the package. Different heat generation rates of the test chip were examined and the motion of phosphor particles due to natural convection currents as well as local heat transfer coefficients over the LED chip were analyzed. A discrete phase model (DPM) of a high-power white LED package was created in order to keep track of individual particles interacting with the carrier fluid and heat flow in a closed LED system. Fluid flow and particle motion are described in terms of flow velocity and temperature distribution as well as particle velocity, particle temperatures and particle kinetic energies at different heat generation rates. A base knowledge was obtained to understand how the particle motion was affected by the heat dissipation from an LED chip without considering the optical heat generation of the phosphor particles.

For this purpose, an idealized discrete phase CFD model of a high-power LED package was created with components that consist of an LED chip (1 mm^2), a ceramic submount (3.5 mm^2) with 0.35 mm thickness , a 1.6 mm thick LED board (30 mm^2), an LED lens with a 20 mm outer diameter and dielectric fluid-phosphor mixture (see Figure 34). Since the fluid domain was in a closed system and phosphor particles were suspended in the fluid domain, initial position, size, and temperature of individual particles were defined with an injection file in the model. A MATLAB script was written to define the initial positions of the particles which were homogeneously distributed in the fluid domain. For the preliminary analysis, in total, 124 particles were created and located in the hemispherical fluid region with a radius of 9.04 mm. A fixed spherical particle diameter of 20 μm was utilized in the current analysis identical to that of the injected particles in a previous paper published by Arik et al. [77].

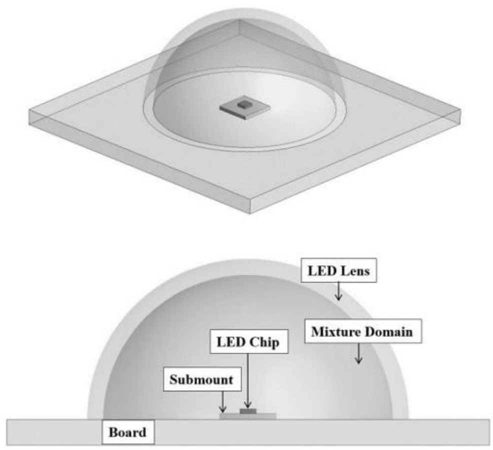

Figure 34: CFD model geometry for the preliminary numerical analysis.

In addition, initial temperature and velocity of particles were set to be 293 K and 0 m/s respectively since they were suspended in the fluid at room conditions before the operation of the LED. Particle loading ratio and material density ratio of phosphor particles in the fluid region were limited to 3.4E-07 and 1 respectively to characterize the flow characteristics of particles without interaction with each other. Simulations were carried out with two-way coupling approach that allowed fluid-to-particle and particle-to-fluid interactions. While fluid carrier influences the particles via drag, particles also influence the carrier-fluid via reduction in mean momentum. In addition, particles closely follow the natural convection currents of fluid since the calculated Stokes number range is between 2.0E-08 and 2.4E- 09 (<< 1).

A mesh sensitivity analysis was conducted to obtain the optimum number of elements as depicted in Figure 35(a). While changing the mesh size junction temperature results were recorded to find suitable mesh configuration. No significant temperature change was observed for mesh counts higher than 345K elements in the computational model.

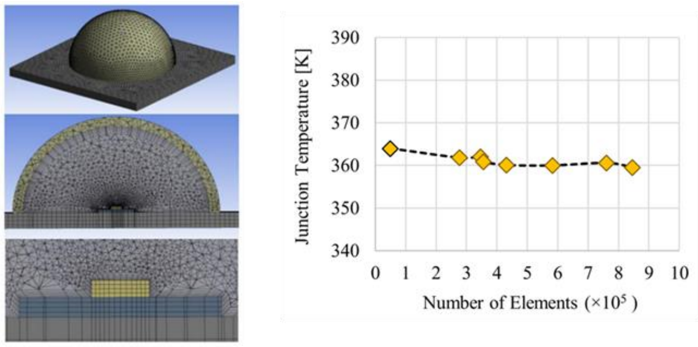

(a) (b)

Figure 35: (a) LED package mesh distribution. (b) Mesh sensitivity analysis.

Figure 35(b) shows the mesh distribution over the external surfaces of the LED system at the half cross section for the package and the region around the LED chip. As can be seen, while the PCB, submount and LED chip components had hexahedral mesh structure, the LED lens and fluid volume had tetrahedral mesh structure with a total number of about 350 K elements. Minimum orthogonal quality and maximum skewness in the mesh were determined to be 0.17 and 0.86, respectively, which indicated the mesh quality was acceptable.

Simulations were conducted for steady state flow conditions however a time dependent analysis was conducted for particle tracks. Interaction between phosphor particles and the optical fluid were coupled to enable heat, mass and momentum transfer between the discrete phase and continuous phase. Number of continuous phase iterations were selected as 10 per DPM iteration and DPM sources were updated for each flow iteration. External surfaces of the LED system including all the sides of the PCB and LED lens were subjected to convection heat transfer with a heat transfer coefficient of 10 W/m^2-K. The LED system was simulated at an ambient temperature of

27 °C. Three different volumetric heat generation rates (0.6 W, 1 W, and 1.4 W) were applied to the LED chip in order to observe the impact of natural convection currents on the trajectory and energy levels of phosphor particles. Three phosphor particles at various initial locations with respect to the LED chip were selected as shown in the Figure 36.

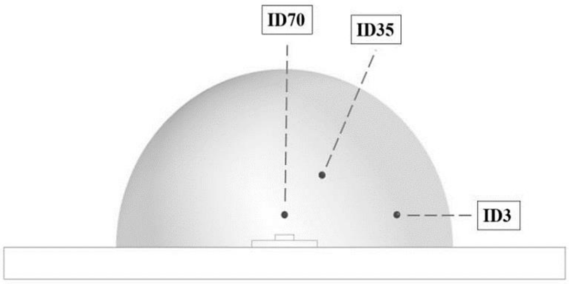

Figure 36: Selected particles location and distribution in Pc-LED package.

Figure 37 shows the velocity vectors at the mid-plane and the three particles shown in Figure 38 were in different flow regions due to the natural convection currents in the fluid domain at different power levels. The results show that the magnitude of flow velocity at 1.4 W heat generation rate decreases outside of the loop region when compared to the 1 W and 0.6 W cases and higher velocity magnitude can be seen closer to the LED chip region.

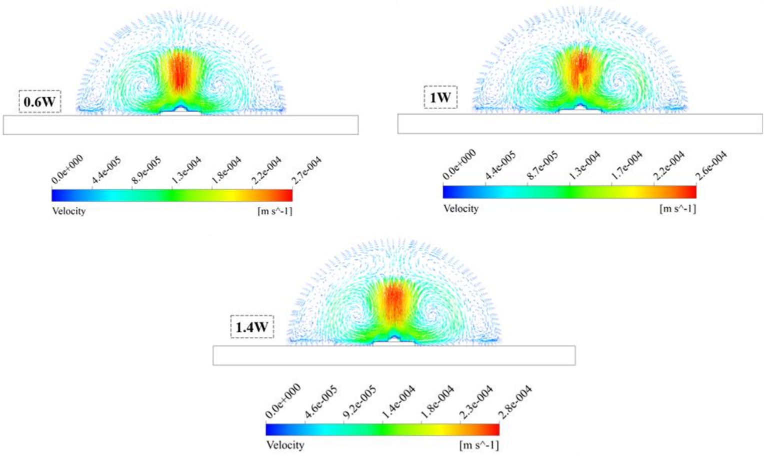

Figure 37: Natural convection flow regions for various power levels.

For the preliminary analysis, the likelihood of phosphor particles to get the direct blue light emission was investigated as they move in the fluid domain as a result of the buoyancy effects. When overall particle trajectories were investigated, it was observed that the LED chip heating power influences the overall distribution inside the mixture. For a 1 W input power, particle trajectories show a denser distribution inside the mixture domain and attracted by the fluid flow in different directions. On the other hand, during 0.6 W and 1.4 W heat generation cases, the particles attracted by the same natural convection flow loops more for the given time interval and movement changes are less visible than the 1 W case. However, in order to have a better understanding of the particle behavior within the flow, individual particle trajectories inside different regions have to be analyzed in detail. If the motion of phosphor particles were better understood at different thermal conditions, then the conversion losses at different parts of the fluid domain and the region of interest where the motion of phosphor particles is most desired in terms of optical and thermal aspects could be identified with the help of analysis.

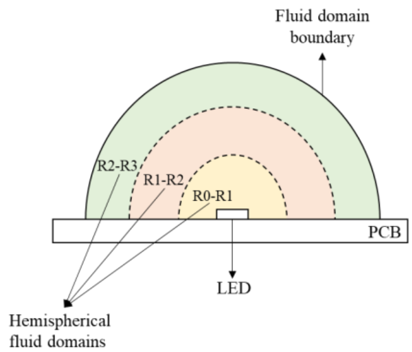

Figure 38: Selected hemispherical regions inside the fluid domain.

Fluid domain was divided into 3 different hemispherical sections that represent the possible regions at which phosphor particles are translating. In the analysis, position vectors of three identified particles with respect to the center of the fluid domain were determined since the magnitude of position vectors indicates the regions of the fluid that the particle spends the most time during its travel. Each particle was evaluated for the percentage of time in which the particle moves in a given field of a fluid domain relative to its total particle trajectory time. A statistical analysis was made to evaluate the possibility of a first exposure of a phosphor particle to blue light emission considering the relative positions of a phosphor particle to the LED chip. The hemispherical regions of different diameters are shown in Figure 38 with the labeled fields. R0 represents the center of the LED chip and radii R1, R2 and R3 are defined as 3.1, 6.2 and 9.4 mm respectively.

In addition to the evaluation of the positions of phosphor particles relative to the LED chip, the impact of heat generation rate and junction temperatures on the heat transfer coefficients over the LED chip are discussed in the next section together with the effects on velocity magnitude as well as energy levels of phosphor particles. Detailed analysis of three selected phosphor particles is also made to get a better understanding of particle behaviors at different initial positions in the fluid domain.

T_j of the LED chip and temperature distributions over the fluid domain were determined for three heat generation rates at 0.6 W, 1 W and 1.4 W and T_j of 337 K, 362 K, 387 K were obtained for 0.6 W, 1 W and 1.4 W respectively. Temperature gradients in the mixture domain without the particles were also investigated. It was found that temperature values observed in a mixture flow region closer to the LED dome area are higher when phosphor particles are not included. Figure 39 shows the change in average fluid flow velocities in the mixture domain with and without the suspension of phosphor particles. It was observed that when the discrete phase was included, energy transfer between two phases were enabled and the average flow velocity due to natural convection was increased.

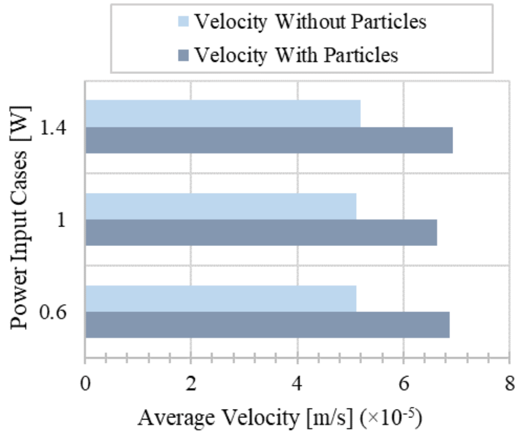

Figure 39: Average flow velocity with and without particles.

Internal energy and temperature changes of individual particles (ID3-35-70) with respect to heating power can be seen in Figure 40. As it is expected, average particle temperature data show a similar trend as the LED package temperature distributions. For heating power of 0.6 W, junction temperature is found to be 337 K while average particle temperature is 322 K. When the heating power is elevated to 1 W, the highest LED chip temperature is 362 K while particle temperature is around 335 K for all three particles. Finally, for 1.4 W heat generation rate, junction temperature is 387 K, and the average particle temperature is found to be 354 K.

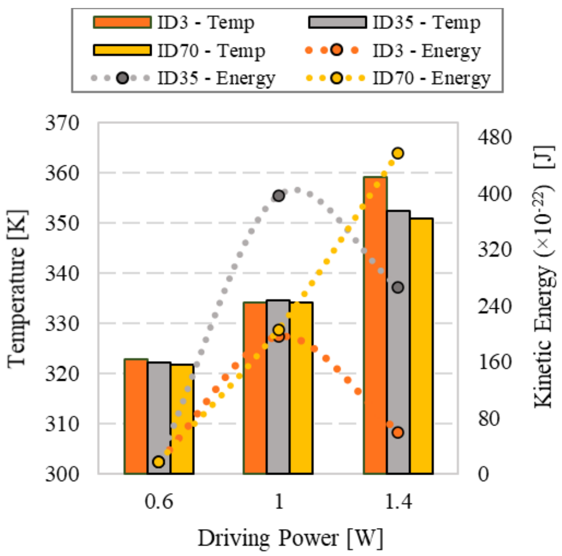

Figure 40: Effect of driving power over kinetic energy.

Since the particle ID70 is in the close vicinity of the upper side of the LED chip, it is subjected to stronger natural convection currents. This was also seen in Figure 41 where the kinetic energy of the particle ID70 is the highest. Since it has a higher average velocity magnitude compared to the other particles, it is expected that the heat transfer coefficient over the particle ID70 is also higher. This results in a lower particle temperature value for the ID70 as shown Figure 40. The observation is also supported in the case of ID3 whose initial position is located at the farthest position in the package. It has a lowest kinetic energy and velocity magnitude in average and higher particle temperature as a result of a lower heat transfer coefficient.

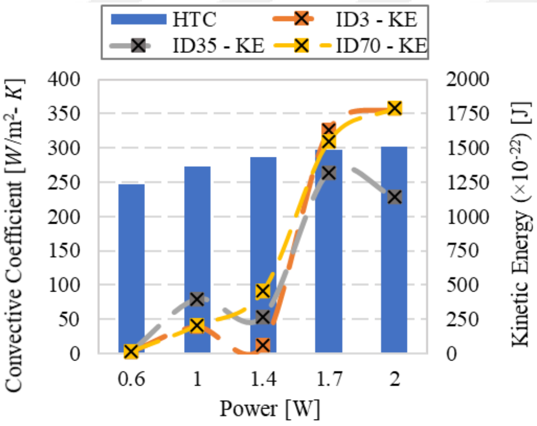

Figure 41: Variation of convective coefficient and kinetic energy with LED driving power.

Figure 41 demonstrates the variation of heat transfer coefficient and kinetic energy with the change in power inputs. As can be seen, heat transfer coefficient and kinetic energy levels change exponentially with power at three originally selected power levels (0.6, 1.0 and 1.4 W). Additional simulations were also conducted for 1.7 W and 2.0 W power levels, and it was seen that this exponential behavior sustained up to 1.7 W and the increase in heat transfer coefficient and kinetic energy levels diminish thereafter. It is worth taking a deeper look and see if the heat transfer coefficients and kinetic energy levels show a different behavior or go to some asymptote with further increase in power.

There are two natural convection flow circles or loops observed in the package, one close to the LED chip (a part of R0-R1 and R1-R2 regions) and the other close to the LED lens (R2-R3 region). The motion of the particle ID35 whose initial position is at the intersection of these circles is subjected to more fluctuations in its kinetic energy level as seen as a downward trend from 1.7 W to 2 W unlike other two particles.

It is also observed that the particle close to the LED chip shows a more consistent rising trend in its kinetic energy level while the ups and downs become more visible as the particle initial position is located farther away from the chip. This is attributed to multi-directional velocity vectors more dominantly observed at the fluid region away from the chip. The results indicate that the kinetic energy changes are influenced by the initial position of a particle and for each particle, kinetic energy changes will be different with the increasing volumetric heat generation. Multi-directional velocity vectors for 1 W volumetric heat generation case can be seen in Figure 42.

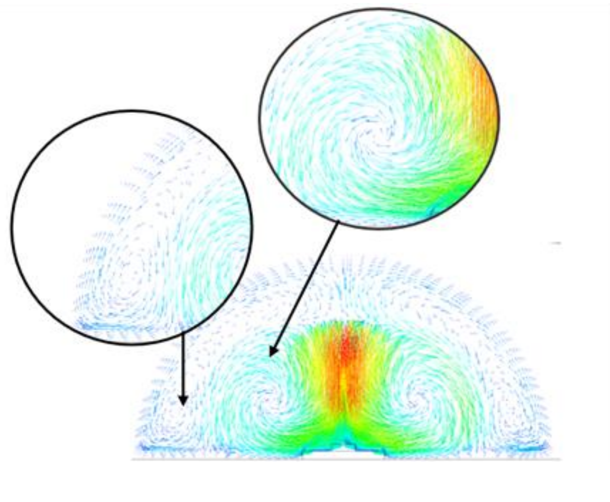

Figure 42: Multi-dimensional flow distribution for 1 W LED heat generation.

Figure 43 demonstrates the velocity history of particle ID3 at three different LED power levels. As it can be seen, the velocity magnitude and fluctuation frequency are all affected by the initial position of the particle, flow path of the particle and the source power dissipated from the LED chip. In fact, the generated heat amounts have a distinct effect at different regions of fluid flow.

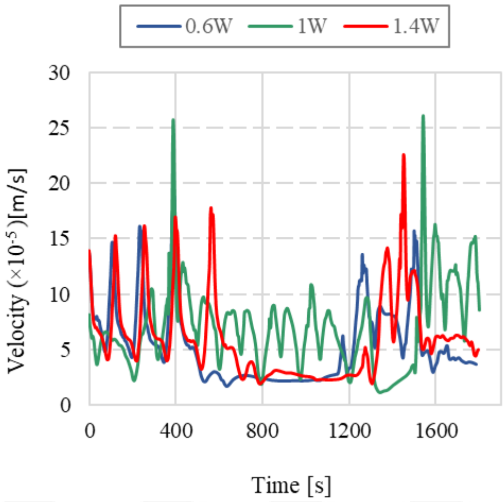

Figure 43: Time dependent particle velocity variation of ID3 phosphor particle.

Furthermore, for particles ID3-35-70, individual path trajectories were investigated to understand particle flow regime under various heat generation cases. The results demonstrate that selected phosphor particles are influenced by the flow regime in the R2-R3 region more than other two regions of the domain. Since R2-R3 region has relatively the largest volume than other regions, it is expected that the particles spent their time mostly in this region. However, it is important to increase the time spent in the region of R1-R2 and especially R0-R1 in order to increase the likelihood of white light emission. As it can be seen from the Table 9, when 1.4 W heating power case is compared to the other cases, particle ID3 spent more time in R2-R1 and R1-R0 regions than it spent in 0.6 W and 1 W cases. In addition, when the heating power was set to the 0.6 W, flow behavior in R3-R2 region becomes more significant than the other parts of the mixture domain. Travel time, path length, velocity, and kinetic energies of particles at different initial positions all affect the optical behavior of the LED package. Different regions have different sizes of the fluid domain and the particles at these regions possess a distinctive chance to yield white light emission. Therefore, flow and energy analysis of particles above may give a significant insight towards how optothermal interactions affect the performance of the LED package. Table 9 shows the percentage of time spent inside different regions for phosphor particles ID3, ID70 and ID35 respectively. The results shown that if the initial position of phosphor particle is at the intersection of two loops, particle is attracted to the towards LED chip more as the heat generation increases from 0.6 W to 1 W. However, if the initial position of a particle closer or far away from the intersection area, particle is expelled from the vicinity of chip region. From 1 W and 1.4 W particle behavior is different. ID35 is expelled from LED chip area and ID3-70 are attracted towards the LED chip.

Table 9: Percentage of time spent in different hemispherical regions.

	0.6 W		1 W		1.4 W	
Particle No	Time Spent (%)	Regions	Time Spent (%)	Regions	Time Spent (%)	Regions
ID 3	83.2	R2-R3	87.9	R2-R3	78.1	R2-R3
	12.9	R1-R2	6.4	R1-R2	16.7	R1-R2
	2.9	R0-R1	2.0	R0-R1	3.8	R0-R1
ID 35	80.7	R2-R3	76.9	R2-R3	83.6	R2-R3
	14.8	R1-R2	17.9	R1-R2	13.2	R1-R2
	2.1	R0-R1	4.0	R0-R1	2.4	R0-R1
ID 70	74.7	R2-R3	83.6	R2-R3	72.7	R2-R3
	18.6	R1-R2	12.9	R1-R2	20.5	R1-R2
	3.6	R0-R1	2.5	R0-R1	4.9	R0-R1

Based on the preliminary numerical analysis, it was observed that there are two significant natural convection current loops observed inside mixture domain, one closer to the chip the other closer to the glass dome and multi-dimensional flow loops are compared with the individual phosphor particle trajectories for different time intervals. When the initial positions of particles were examined according to the different natural convection loops, particles showed different behaviors with the increasing heat generation rates in terms of kinetic energy changes and velocity magnitudes. Computational results have shown that the initial positions of phosphor particles and volumetric heat generation rates influence the probability of particles to get direct blue light emission inside the optical fluid.

4.1.2 Advanced Pc-LED Numerical Model: Analysis of Self-Heating Particles Over an Immersion Liquid Cooled High Power Blue LED

Following the first set of numerical study, an experimental setup was built for the proposed Pc-WLED configuration. Initial experiments were conducted to better interpret the findings presented in Chapter 4.1.1 and form the fundamentals to develop the advanced Pc-WLED numerical model which will be discussed thoroughly in this chapter. Figure 44 depicts the main components of the new Pc-WLED in a prototype setup where convective flow patterns can be seen due to the heat generation of the immersed LED chip. Injected phosphor particles inside dielectric fluid enclosed by a hemispherical dome are in continuous motion under buoyancy effects generated by the higher temperatures at LED surfaces.

In order to characterize the thermal behavior of such configuration, location based self-heating values of phosphor particles and their motion require deeper fundamental research. Since the thermal and optical performance of Pc-WLED packages are strong functions of various phosphor related parameters (i.e. particle size, position, volume fraction, etc.) during operation, it is critical to develop a more realistic dynamic model that can accelerate the optothermal optimization of new generation LED products. Different from preliminary implementation of DPM to characterize the phosphor motion in an immersed cooled LED, updated DPM approach with locally variable self-heating particles introduced herein to analyze the light phosphor interaction in an immersion cooled LED package.

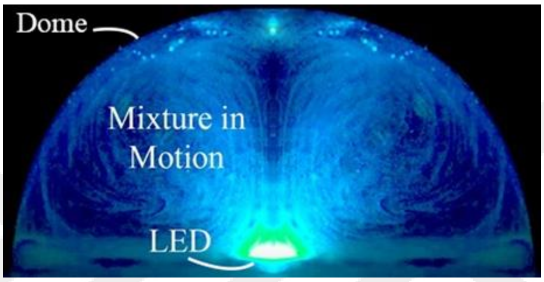

Figure 44: Phosphor-fluid mixture in a Pc-LED configuration.

DPM scheme is advantageous to track phosphor particles under natural convection driven flow since it accounts for the mutual interaction between the fluid and particles with two-way coupling. An LED lens, phosphor particles, encapsulant fluid, chip, mold base, and Printed Circuit Board (PCB) are all modeled using fully coupled fluid flow and energy equations. Phosphor particle trajectories are calculated in the Lagrangian frame while the continuity, momentum, and energy equations of continuous fluid domain are solved in the Eulerian frame.

The Lagrangian-Eulerian two-phase model is represented by the following equations [272,273]:

$$\nabla.(\rho \boldsymbol{V}) = 0 \tag{6}$$

$$\nabla.(\rho \boldsymbol{V}\boldsymbol{V}) = -\nabla P + \nabla.(\mu \nabla \boldsymbol{V}) + \rho\beta(T - T_o)g + S_m \qquad (7)$$

$$\nabla.\left(\rho \boldsymbol{V} c_p T\right) = \nabla.(k\nabla T) + S_e \qquad (8)$$

The source terms for the momentum and energy exchange between particles and the fluid represented by the S_m and S_E [274,275]:

$$S_m = \sum n_p \frac{m_p}{\delta V} \frac{d\boldsymbol{v}_p}{dt} \qquad (9)$$

$$S_E = \sum n_p \frac{m_p}{\delta V} \frac{dT_p}{dt} \qquad (10)$$

Where t, v_p and T_p are time, particle velocity and particle temperature, respectively. In addition, m_p is the particle mass, n_p is the number of particles within a cell volume (δV).

Because of the drag force (F_D) acting on each particle with a mass of m_p, difference between v_p and local fluid velocity (v_f) can be expected.

For the accurate computation of the particle motion, the force balance equation derived from Newton's second law is solved in the Lagrangian approach:

$$\boldsymbol{v}_p = \frac{d\boldsymbol{x}}{dt} \qquad (11)$$

$$\boldsymbol{F} = m_p \frac{dv_p}{dt} \qquad (12)$$

Where **F** represents all the relevant forces acting on the particle and can be written as:

$$\boldsymbol{F} = \boldsymbol{F}_D + \boldsymbol{F}_B + \boldsymbol{F}_G + \boldsymbol{F}_x \tag{13}$$

In which, F_D is the drag, F_G is the gravitational, F_B is the buoyancy force, and thermophoretic, brownian, and erosion/accretion forces are denoted by F_x and found to be unimportant and neglected for trajectory calculations. Upon the review of [276], it has been determined that the thermophoresis effect is more significant in gases due to weaker cohesive intermolecular forces than that in liquids with the exception that the liquids with low thermal conductivity (i.e., less than 0.04 W/m-K) may still be subject to thermophoresis. However, given the main phase in the present study is liquid and the thermal conductivity of YAG:Ce^{+3} is approximately three orders of magnitude bigger (i.e., 13 W/m-K [45]), thermophoretic effects are deemed to be negligible. Moreover, the studies of [277–281] show that disregarding the Brownian influence is a suitable approach for the modeling of dispersed particles above the submicron scale. Given the present effort deals with particle sizes in the range of 5 µm $\leq d_p \leq$ 45 µm, the Brownian forces are considered to be negligible as well [282]. Therefore, eliminated the last term on the RHS, the drag force is the dominant term in Eq. 13, and the buoyancy and gravitational forces are secondary.

$$\boldsymbol{F}_D + \boldsymbol{F}_B + \boldsymbol{F}_G = m_p \frac{d\boldsymbol{v}_p}{dt} \tag{14}$$

Time dependent integrated force balance equation acting on each particle is obtained as:

$$\frac{d\boldsymbol{v}_p}{dt} = \boldsymbol{F}_D(\boldsymbol{v}_f - \boldsymbol{v}_p) + \frac{g(\rho_p - \rho_f)}{\rho_p} \tag{15}$$

Where g is the gravitational acceleration and ρ_p and ρ_f are particle and fluid density, respectively. Expression of drag force in terms of viscosity (μ), drag coefficient (C_D), and particle Reynolds number (Re_p) is as follows:

$$\boldsymbol{F}_D = \frac{18\mu}{\rho_p D_p^2}\frac{C_D Re_p}{24} \tag{16}$$

Where Re_p is calculated based on the relative velocities of the continuous and discrete phases as:

$$Re_p = \frac{\rho_f\, D_p\left|\boldsymbol{v}_p - \boldsymbol{v}_f\right|}{\mu} \tag{17}$$

Depending on the drag model in use, the coefficient of drag can be calculated using Re-C_D relations given in [283,284]. By applying the rigid spherical drag law, C_D can be determined as:

$$C_D = a_1 + \frac{a_2}{Re} + \frac{a_3}{Re^2} \tag{18}$$

Where a_1, a_2, and a_3 are the model constants presented in [283] or

$$C_D = \frac{24}{Re}\left(1 + b_1 Re^{b_2}\right) + \frac{b_3 Re}{b_4 + Re} \tag{19}$$

Where b_1, b_2, b_3 and b_4 are calculated to be 0.1862, 0.6529, 0.4373 and 7185.35 for a spherical particle with a shape factor of 1 based on the given relations of Haider and Levenspiel [284].

The simplified version of the trajectory equation is obtained by solving Eq.11 and Eq.12 together in each coordinate direction with the assumption of constant body force over each small-time interval. The time required for particle velocity adjustment is represented by particle relaxation time (τ_p):

$$\frac{dv_p}{dt} = \frac{1}{\tau_p}(v_f - v_p) \tag{20}$$

The interaction between continuous and discrete phases should be well defined with the adaptation of suitable coupling approaches for an accurate prediction of particle-laden flows [285]. Dilute suspension of solid particles can be represented by one or two-way coupling depending on the particle volume fraction (ϕ_p). In this study, ϕ_p ranges from 10^{-8} to 10^{-5}. Unlike the one-way coupled DPM numerical modeling approach [286], volume fractions are taken into account in this study to allow phosphor particles to influence the carrier fluid medium while the fluid also has an impact on phosphor particles throughout their path. Although one-way coupling can be justified for the particle volume fractions near 10^{-8} [36] to simplify the momentum and energy equations, the interphase exchange of heat and momentum should be accounted for to ensure the dynamic coupling of thermal and optical models for self-heating photoluminescence particles. With the two-way coupling approach, the momentum and heat exchange are represented with sink and source terms in the momentum and energy balance equations of the continuous phase.

Since the discrete phase particle (YAG:Ce) is not a volatile material, no change is observed in the mass of particles during their motion. Thermal conduction in hypothetical collision with other particles or the surrounding domain is ignored because each particle is modeled as a perfect sphere.

A representative three-dimensional (3D) geometry is created including a chip, a sub-mount, a PCB, and optically clear dielectric fluid encapsulated inside a hemispherical glass dome. Additional connectors and wire bondings are excluded from the model to simplify the computational domain without compromising the accuracy. Schematic of the high-power LED package is presented in Figure 45(a) with relevant dimensions of each component given in Figure 45(b).

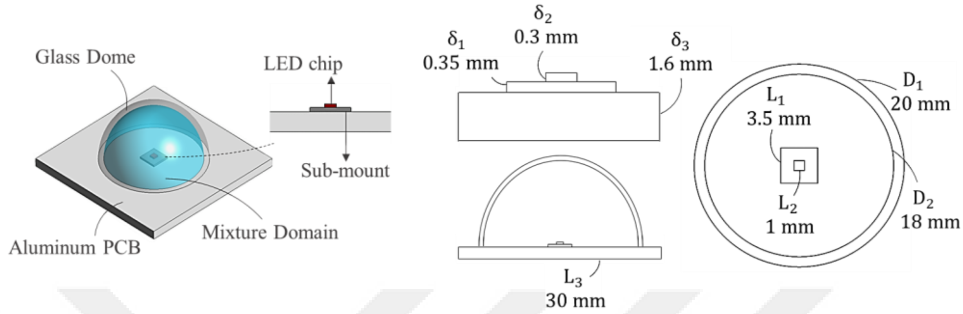

Figure 45: Three dimensional symmetric CFD modeling geometry.

Table 10: Material properties.

Thermal Conductivity (W/m-K)		Thermophysical Properties HFE 7000	
k_f (HFE 7000)	0.075	μ (kg/m-s)	0.0238
k_{chip} (Si)	180	ρ (kg/m3)	1400
k_{mount} (Enclosure material)	24	β_f (1/K)	0.00219
k_{dome} (Epoxy-glass fiber)	0.17	c_p (J/kg-K)	1300
k_{PCB} (Al Die Cast 90)	105	κ (m^2/s)	4.12E-08
-	-	Pr	413

Following 3D modeling of the LED package's main components, an in-house MATLAB script was written to define the initial positions of the particles for a specified number of particle injections. In the script, particles are separated by a uniform spacing determined by np inside the domain, as well as the wall-to-particle and the device-to-particle distances. In a such manner, overall particle behavior can be analyzed in a broader view and the heat dissipation capability of the proposed cooling method can be examined in any position. To import the file containing the dispersed initial particle positions into ANSYS Fluent, a file injection model is utilized. As DPM simulations begin and the position of particles is initialized, the code has no further effect on the solution. Initially, particles are assumed to be in momentum (v_p=0 m/s) and thermal equilibrium (T_p=293 K) with the surrounding fluid. Similar to reported cases in the literature [83,84,287], thermal and flow behaviors are examined in 5-45 μm phosphor diameter range.

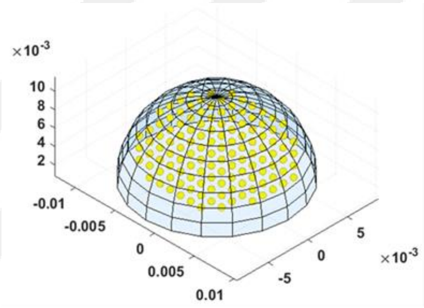

(a)

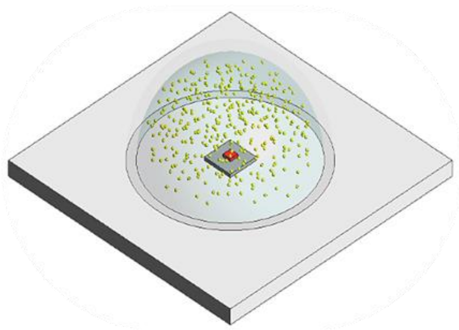

(b)

Figure 46: (a) Visualization of the in-house written code for particle distribution in MATLAB, and (b) initial locations of the injected particles at t=0 s in ANSYS Fluent (number of particles = 343).

The range of volume fraction of phosphor particles in the fluid domain (ϕ_p) varies between 10^{-8} to 10^{-5} in different particle size cases. Particle Re range is found to be in between 10^{-5} and 10^{-7} (Re_p<<1) while Stokes number is less than unity for the studied cases and it is expected that the particles will follow the primary phase flow field. Additionally, the natural convection flow regime is assumed to be laminar as the calculated Rayleigh numbers are below 108 with Prandtl number close to 413 [288].

In order to keep the consistency with the previous experimentally validated immersion cooling study [270], the outer surfaces of the dome and the PCB are exposed to a convective heat transfer coefficient of 10 W/m^2-K at 300 K ambient air. In addition, heat generation of the chip is defined as 1 W considering typical operation conditions of the high-power LED. To model the natural convection in a hemi-spherical region, Boussinesq approximation is applied with the density of the fluid being taken constant in all terms of the momentum equation, except the Buoyancy term. Thermal radiation is disregarded to simplify DPM simulations due to the dominance of convective heat transport (convective heat transfer is determined to be two to three orders of magnitude higher than radiation heat transfer). Schematic of the employed boundary conditions, governing parameters, and equations are given in Figure 47.

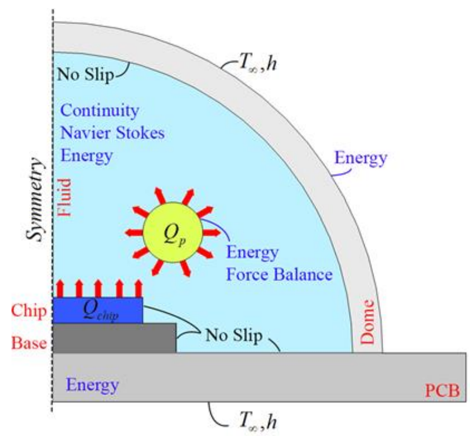

Figure 47: Schematic illustration of the boundary conditions, governing parameters, and equations.

To ensure grid independence on computational results, a mesh sensitivity analysis is performed with coarse and fine grid sizes (Figure 48(b)). For each mesh configuration, temperature variations at thermally critical locations such as the chip's surface, and middle and top positions of the mixture domain are recorded. The variation of the fluid velocity with the grid size is also analyzed at the same region to find the optimum mesh size as the most significant temperature difference is observed at the middle point along the vertical axis in the fluid domain (shown in Figure 51). Grid independence is obtained for mesh above 0.8 million element number with negligible variations in the temperature and the velocity of 0.3 K and 0.001 mm/s, respectively. In addition, the maximum aspect ratio is less than 10 and the volume ratio for elements with high skewness (0.75-0.89) is found to be below 0.02. Figure 48(b) shows the cross section of the domain with the optimized mesh and the refinement of the grid in the proximity of the solid boundaries.

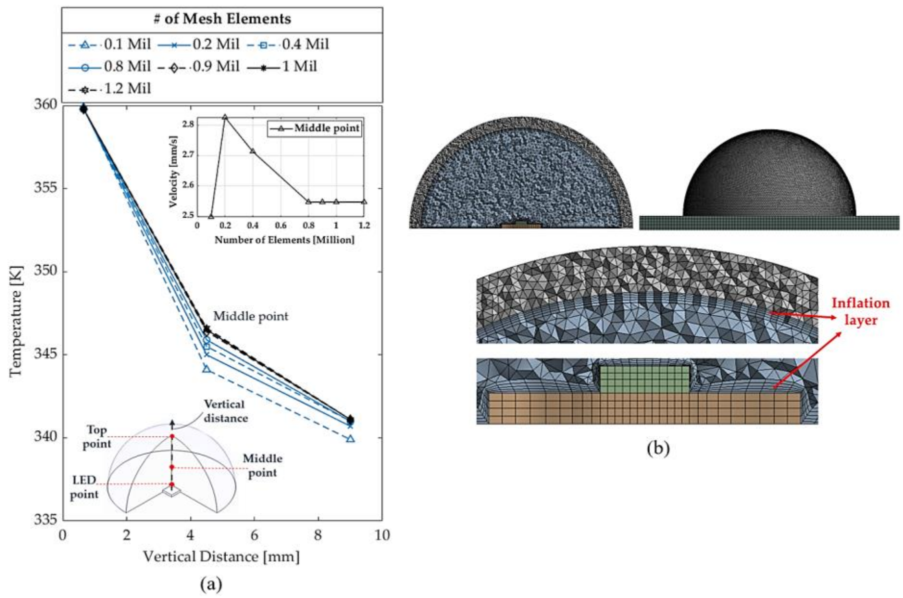

Figure 48: (a) Mesh sensitivity analysis presented for seven different grid refinements, and (b) optimized mesh distribution of the model and inflation layers between the fluid/solid interfaces in close view.

During the phosphor conversion, a fraction of the blue light emission is turned into heat due to low quantum efficiency of phosphor and Stokes shift effects. Particle heat generation strongly depends on the position of the particles with respect to the chip. Hence, it is crucial to implement a position-dependent heat generation rate of phosphor in thermal simulations. Local heat generation rates for 5 µm to 45 µm diameter YAG:Ce particles are presented by Azarifar et al. [44]. In that study, Monte-Carlo ray tracing simulations were employed over discretized control volumes and the change in phosphor heat generation depending on the particle was shown. Since higher phosphor heat generation rates were observed for the particles closer to the chip and heat generation rates were decreasing as the phosphor particles placed away from the chip, it was concluded that the heat generation rate of a phosphor particle can be neglected for irradiance values less than 0.1 W/mm^2.

In order to account for position dependent thermal variations, phosphor heat generation results of that research are exported to FLUENT simulations with a User Defined Functions (UDF) (refer to Appendix A). Custom inert heating law is activated to include the influence of heat generation on the particles. As particles move from one computational cell to another, temperature difference between particle and fluid is calculated at any instant based on spherical body convection thermal resistance. Heat transfer coefficient over particle surface is predetermined by the Ranz and Marshall correlations and based on the simple time-dependent heat balance equation, temperature difference is added as a source term to the energy equation of the continuous phase [289,290].

$$Nu = \frac{hd_p}{k_\infty} = 2.0 + 0.6Re_d^{1/2}Pr^{1/3} \tag{21}$$

$$m_p c_p \frac{dT_p}{dt} = hA_p(T_\infty - T_p) \tag{22}$$

Since the internal conduction resistance of a micro-scale phosphor particle is considerably smaller compared to external convection resistance, the lumped model is assumed for the particles moving throughout the domain. Magnitudes of heat generation of phosphors and the corresponding heat flow paths of the LED package are then used to determine how the heat generation is applied at different regions of the fluid domain. As can be seen in Figure 49, when a phosphor particle is located on the surface of the chip, Qp can reach up to 2 mW. For a particle with diameter of 45 µm, the self-heating effect is considered to be very significant with Q_p ranging from 0.2 mW to 2 mW where the distance from the chip is below 1 mm.

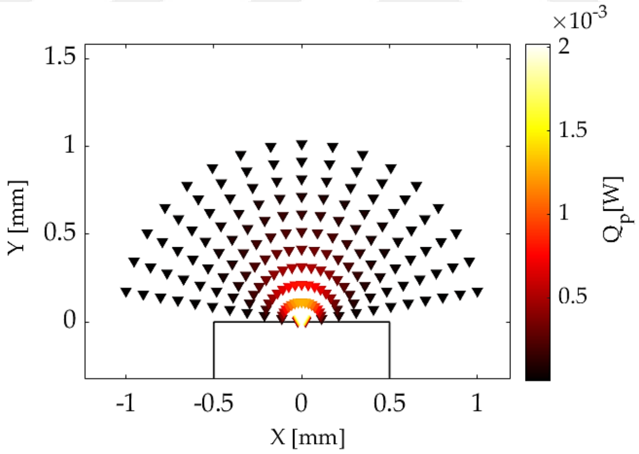

Figure 49: Local phosphor heat generation for particles with diameter of 45 µm due to absorbed irradiance from the LED.

According to the temperature difference analysis between the phosphor particles and the surrounding fluid, the self-heating effect is found to be high enough to be considered in the thermal models when D_p /Q_p is below ~0.5 mm/mW. This is attributed to greater alterations in temperature of particles and high irradiance levels when D_p/Q_p is below this ratio. Since the phosphor encapsulation in the considered configuration is significantly larger than conventional phosphor coating methods, lower phosphor volume density can ensure enough color conversion to achieve white light. Thus, the fraction of the volume of injected phosphor particles to the volume of the mixture domain is in the range of $\phi_p \leq$ 3E-08, and light re-scattering between the particles can be ignored in the case of particle heat generation. However, in the case of a smaller dome, particle-to-particle interaction becomes more prominent, and the re-scattering effect between phosphor particles must be considered as the volumetric density of the phosphor increases [44,83].

Initially, computational results obtained in this study with the DPM method are compared with those from a previous Pc-WLED study conducted by Tamdogan [291]. Boundary conditions given in the previous study are directly adapted for an accurate comparison. Overall, junction temperatures determined by the DPM of the present study with self-heating particles are in good agreement with the experimental data.

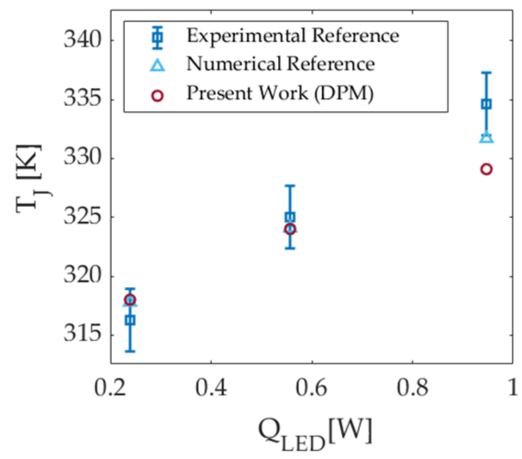

Figure 50: DPM validation with the experimental and numerical results of [291] ($\Delta\delta$= 2.66 K).

Figure 50 shows that the difference between the computationally and experimentally determined junction temperatures is approximately 1 K for relatively low heat generation rates of the LED chip. On the other hand, the difference exceeds 5 K at relatively high rates of heat dissipation. This is due to the fact that the number of particles is not identical in the previous experiments and the current simulations. It is worth mentioning that the effort shown in [291] did not conduct any particle based investigations for immersion cooling of Pc-WLEDs and no information was provided about the particle size and the number. Since it is expected that higher chip powers can lead to increased self-heating of phosphor particles and elevated fluid temperature, the junction temperature of the LED chip raises more with higher number of particles.

The velocity distribution in the fluid domain affects particle distribution and optothermal performance of the package. Therefore, it is important to extract the velocity distributions generated by the natural convection currents before analyzing the self-heating effect of phosphor particles and their impact on fluid flow. As shown in Figure 51, there is a quasi-steady circular motion of dielectric fluid inside the mixture due to the buoyancy driven flow. The temperature of the fluid in the vicinity of the LED chip increases due to the heat generation induced by the LED. Thereafter, fluid starts to accelerate along the vertical direction and impinges on the top inner surface of the LED dome, with an approximate velocity of 1 mm/s. Due to the continuous operation of the chip, heated fluid follows the curvature of the dome while dissipating heat to the surrounding medium until a full circulation is completed. Similar vortex behavior can also be seen in large droplets during dropwise condensation or evaporation as reported in [292]. However, fluid flows at relatively low velocities near the inner surface of the dome due to the no slip condition, while slip condition exists at the wall boundaries in the case of a free droplet.

A close examination of velocity profiles given in Figure 51 shows that the highest fluid velocities are obtained at the middle scale where vertical distance of 1-6 mm from the chip and at the horizontal distance of 0-1.4 mm from the central axis. Since the natural convection flow strongly influences the particle's trajectory (St<<1), they reach higher velocities and spend less time at the aforementioned regions. In addition to natural convection currents, the motion of phosphor particles is also affected by the changes in the flow field due to the self-heating of phosphor particles.

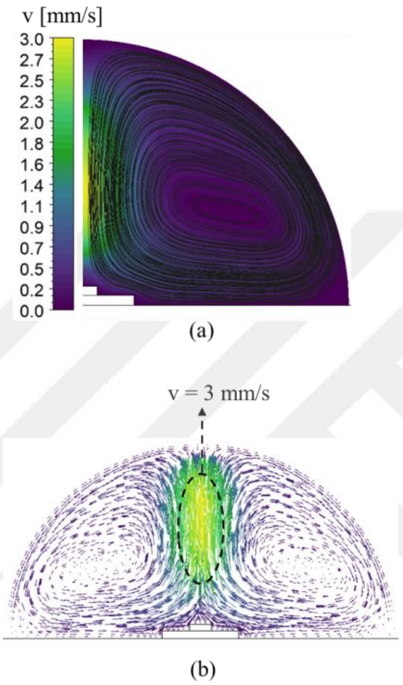

Figure 51: (a) Natural convection flow fields in the mixture domain for the particle diameter of 45 μm. Velocity contours combined with velocity streamlines (Ψ), and (b) Velocity vectors (v).

Temperature distribution within the Pc-LED package is analyzed and depicted in Figure 52. LED chip's junction temperature is calculated to be 355 K. Volume-averaged fluid temperature is found to be 340 K while the highest fluid temperatures are observed in the close vicinity of the chip within a 1 mm^3 region, experiencing a temperature gradient of approximately 5 K/mm.

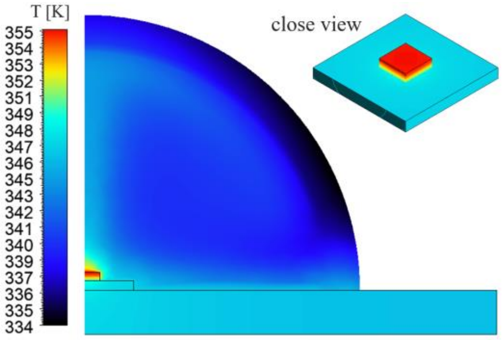

Figure 52: Temperature distribution of the Pc-LED package consisting of phosphor particles with diameter of 45 μm (The rate of heat generation of the LED chip is 1 W, and the maximum chip temperature is 355 K).

As it was mentioned earlier, phosphor particle temperature is one of the most critical parameters that significantly affect the illumination performance of a Pc-LED. Therefore, phosphor temperature change over the fluid temperature in vertical and horizontal directions from the chip surface has been analyzed for various particle diameters and depicted in Figure 44. Maximum phosphor heating effect is recorded for the 45 μm particle located at ~0.05 mm area above the chip. Immersion cooling effectively keeps the highest phosphor temperature below 417 K (which is much lower than the onset quenching temperature of YAG:Ce, ~500 K [293]). Along its trajectory, the temperature of the phosphor particle can decrease by more than 40 K following the departure from the near chip area. When the particle approaches the surface of the dome, thermal equilibrium with the surrounding fluid is observed. Due to the reduced irradiance level, heat generation of the particle in this region is less than 0.01 μW.

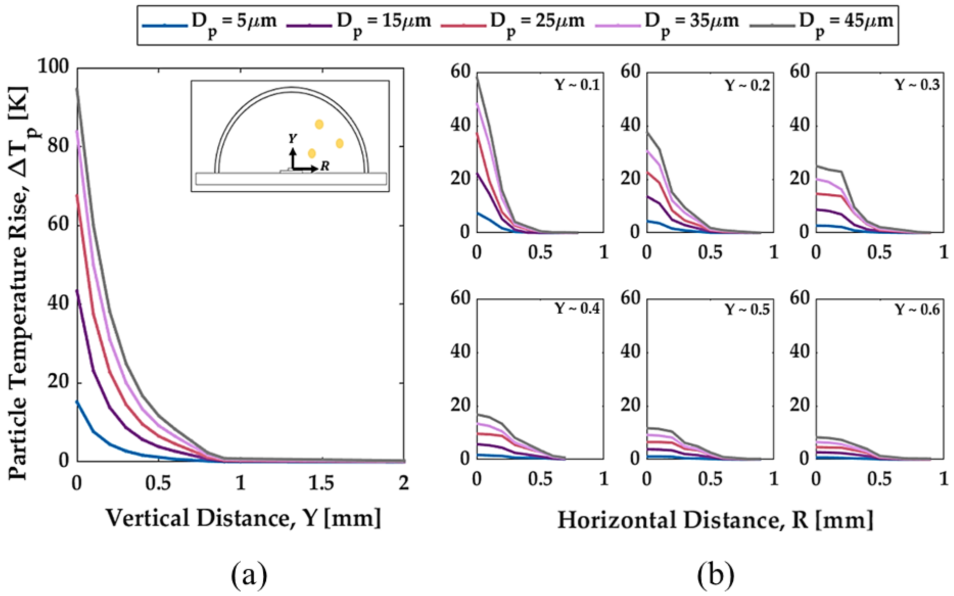

Figure 53: Phosphor temperature rise over the surrounding fluid at (a) vertical and (b) horizontal distance from the center of the chip in the mixture domain. Particle diameter is altered between 5 µm and 45 µm (Y=0 and R=0 represents the middle of the LED surface).

As observed in Figure 53(a), temperature variation is found to be more dramatic in the vertical axis because of the Lambertian emission profile of the LED and significance of the particle-light interaction. Even for the smallest particle diameter case (5 µm), the temperature rise is determined to be in the excess of 15 K in that axis. Furthermore, phosphor temperature increases less as particles move away from the chip in the vertical direction. Overall, it is worth saying that the rise in phosphor temperature is proportional to the diameter of the particle in the vertical direction.

Temperature change along the horizontal direction at various Y coordinates is shown in Figure 53(b). In contrast to the temperature variation in the vertical direction, less abrupt changes in the horizontal direction, up to 0.5 mm away from the center of the chip, can be seen. Except in regions where Y < 0.2 mm, temperature gradients do not exceed 20 K even for the largest particle diameter of 45 µm. Irradiance levels are lower at the sides of the chip, which translates to lower temperature gradients in line with the spatial distribution and intensity of the received light.

Since increased temperatures at the p-n junction inversely affect the optical performance, it is critical to examine the effect of excess heat load introduced by the phosphor particles on the LED chip. Therefore, a Figure of Merit (FOM) is defined to characterize the significance of phosphor temperature rise over the chip temperature.

$$FOM = \frac{\Delta T_p}{\Delta T_{LED}} = \frac{T_p - T_{f,ave}}{T_{LED} - T_{f,ave}} \tag{23}$$

where $T_{f,ave}$, T_p, and T_{LED} denote average fluid temperature inside the mixture domain, phosphor particle temperature, and LED chip temperature, respectively. Figure 54 shows the variation of the FOM and particle KE levels as a function of particle size. Two cases are studied here, namely with and without the self-heating of the particles in order to describe the influence of the phosphor heating. The average phosphor temperatures are recorded when the particle position is in the near scale (i.e within 1 mm from the chip in the vertical and within 0.5 mm from the chip in the horizontal direction). For all cases, the instantaneous T_p and near particle local fluid $T_{f,ave}$ were recorded throughout the particle’s trajectory for the difference of 14.5 K between the volume average fluid and LED temperatures.

As it can be seen from Fig. 54, the temperature rise of the phosphor is higher than the temperature rise of the junction of the chip when the phosphor self-heating is taken into account. When the particle diameter is varied from 5 µm to 45 µm, a more than 3-fold increase in the FOM can be seen. Due to the increased heat transfer area at high heat generation rates, the rate of heat transfer of a 45 µm particle is significantly higher than that of a smaller particle. Depending on the self-heating and employed cooling solution, higher temperature differences are observed with increasing particle size. In contrast, without the self-heating effect, there is no temperature difference between the phosphor particle and the surrounding fluid, thus the FOM becomes zero.

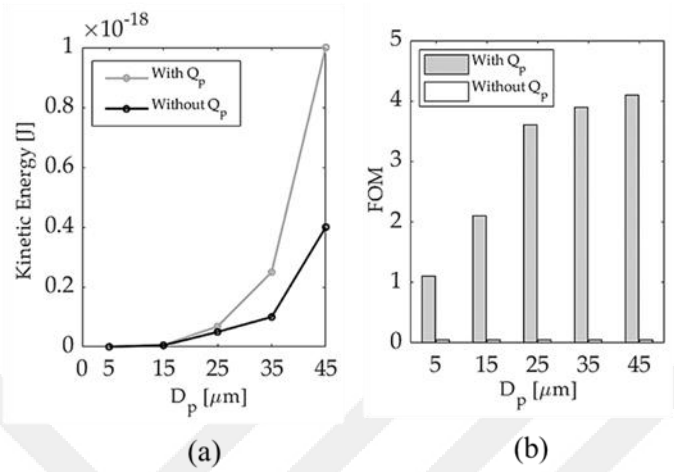

Figure 54: (a) Variation of average particle kinetic energy, and (b) Figure of Merit (FOM) analysis at different particle diameters including the effect of the phosphor heat generation.

Furthermore, an assessment of the change in the particle's KE levels with respect to the light interaction reveals that the average KE is almost invariant for diameters up to 15 μm. The KE of the particles is doubled when the particle diameter is increased from 15 μm to 35 μm. This phenomenon is mainly driven by the increase in the volumetric heat generation of particles with diameters larger than 25 μm. Likewise, there is a substantial increase in the FOM value for particles larger than 15 μm. This issue results in increased velocity of the phosphor particle and the surrounding fluid. To better understand the underlying mechanism, the nature of particle trajectories influenced by the variations of temperature and the KE is analyzed for different particle diameters in the same number of particle injection. It is observed that the particle movement is not always in the same plane of the circulative motion of natural convection currents. The flow field shows three-dimensionality and the velocity values in the third dimension are noticeable. Therefore, phosphor particles can get attracted by different flow loops, depending on the particle's initial position, size, and temperature. This is further investigated with the comparison of trajectories taken by the smallest (5 μm) and the largest (45 μm) diameter particles. As observed in Figure 55(a) for particles having the same initial position, there is a salient difference between the trajectories taken by the smallest and the largest particles in the given time interval ($0 < t < 150$ s in Figure 55).

Depending on the size of particles, noticeable differences can be observed in particle distributions within the fluid domain (see Figure 55). The smallest particles (5 μm) travel in densely populated areas at the inner regions of the flow loop and form a circular eye for a given time interval. In contrast, the largest particles (45 μm) move in a path extending over a wider area and typically stray away from the vortex movement. This phenomenon can be related to blue light irradiation and self-heating effects that alter the flow field and KE levels. High heat generating particles move faster and switch between flow loops at different KE levels. Moreover, when the number of phosphor particles is kept the same, the likelihood of particle-light interaction becomes much less for smaller diameters. As shown in the case of a particle with ID 342, the difference in total distance traveled by different particles in different sizes reaches up to 26.5 mm within a 150 s interval. When analyzed in detail, the most significant change in the fluid velocity is observed between 0 s to 30 s when the phosphor particle is in the high light irradiance region. In fact, in this time interval, the average fluid velocity near the 5 μm particle surface is 0.8 mm/s lower than that of the 45 μm size case. Thus, the average KE of 45 μm particle is 2,000 times larger than the 5 μm particle. As a result, one can conclude that, for the same time interval and number of injections, larger size particle will cover a greater distance which can be in favor of the particle’s coverage probability in exposure to the blue light emission.

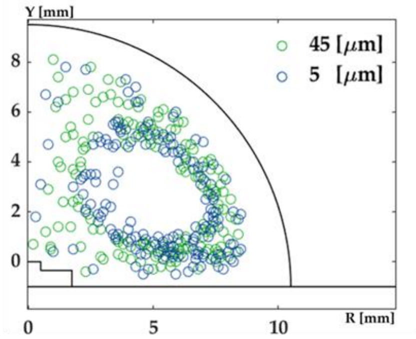

(a)

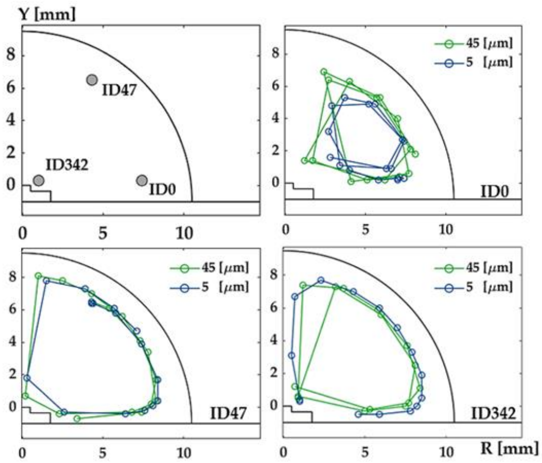

(b)

Figure 55: (a) Comparison of the particle trajectories for 5 μm and 45 μm diameter cases (t=0-150 s, position data recorded at each 10 s, number of shown particles = 11). (b) Individual particle trajectory comparison of 5 μm and 45 μm diameter cases.

In the current analysis, the same number of particles at identical initial positions were injected into the mixture domain to compare the individual particle trajectories of various phosphor sizes. This time, particle to fluid volume fraction ($\phi_p \approx$ 3E-08) is kept constant for each diameter case (See Figure 56) and particle behavior is analyzed in a broader view when amount of heat dissipation from the particles to the mixture domain is the same. Particles' KE levels are analyzed in three distinct regions depending on the significance of particle-light interaction.

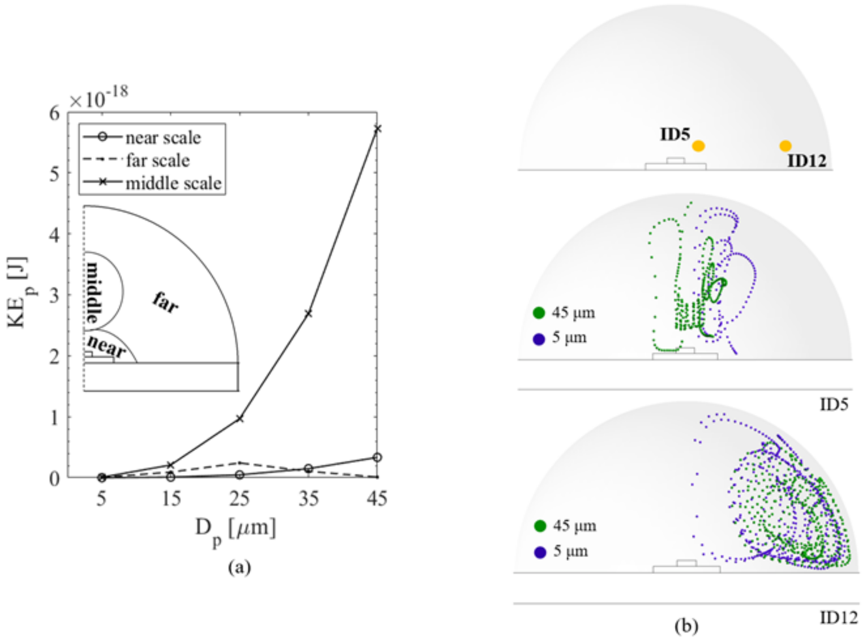

Figure 56: (a) KE change of particles in near, middle and far scales regions. (b) Particle trajectory comparison of 5 μm and 45 μm particle cases are shown. Particle to fluid volume fraction is kept equal for each diameter case for the comparison. The displayed trajectories are in the same x-y plane (t = 0-450 s, position data recorded at each 1s with $\phi_p \approx$ 3E-08).

Similar to the previous analysis, particle velocity and KE levels increase with particle size at near scale regions. Even though the particle volume fraction in the fluid domain is equivalent in each case, it is not possible for highly mobile particles to have the same total heat dissipation at distinct regions. Especially at near scale regions where particle heat generation is high, greater heat loads are still transferred to the fluid phase from larger-sized particles (despite being in fewer numbers to make the particle volume fraction ratio the same for all cases). Thus, larger-sized particles appeared to be faster at high illumination zones when compared with smaller particles in other cases at the same volume fraction ratios.

The highest KE levels of particles are observed at the middle scale, where the maximum fluid velocity is observed. Due to the rapid increase in the magnitude of the convective currents in this region, the variation of particle velocity between different particle diameters is low. Thus, a proportional change is observed in the KE of particles with the increase in particle size and mass. On the other hand, particle velocities start to decrease with particle size at far scale regions where the blue light irradiance is substantially low, and the self-heating effect is insignificant. Moreover, the peak point in the KE levels is reached with the particle diameter of 25 μm in far scale regions where particle heat generation no longer increases velocity. As shown in Figure 56(b), the comparison of two individual particle trajectories supports the aforementioned behaviors. Due to the high irradiation of blue light near and middle scale regions, the path taken by the 45 μm diameter particle is greater that the path taken by 5 μm diameter (ID 5). The opposite of this behavior can be clearly seen when the particle is concentrated in the far scale region (ID 12), where lightweight particles move faster and cover longer distances than the larger particles.

In conclusion, introduced advanced Pc-WLED model enables particle based characterization of YAG:Ce phosphor in an immersion cooled Pc-WLED. Phosphor particle self-heating coupled with the blue light interaction presented that the temperature rise of optical fluid can reach up to 95 K if particles with a diameter of 45 μm and volume fraction of 1.5E-08 travel as close as 0.05 mm above the LED chip surface. Thermal loads introduced to the mixture domain are found to be much lower for the same number of particles with a diameter of 5 μm to 15 μm. Furthermore, extracted particle trajectories shown that the probability of blue light irradiation to smaller particles will be lower for the same number of particles. Specifically, in the near and the middle scale regions, particles with a diameter of >25 μm are shown to have higher mobility and blue light irradiation due to heat loads transferred to the fluid field (%300 increase in FOM). Finally, if the volume fraction of the phosphor particles is kept equal for different particle sizes, lightweight particles are observed to cover greater distances in far scale regions with higher blue light irradiation probability.

4.2 Validation Study

Based on the particle based experimental analysis demonstrated in the Section 3.4, a comparison study was conducted for validation. Particle velocity findings of the black coated LED were compared with the ANSYS Fluent DPM analysis and good agreement was achieved between the experimental and computational results.

For the validation study, the CFD geometry was updated according to the immersion cooled LED packages prepared for the experimental investigations (see Fig. 57(a)). Based on the mesh sensitivity analysis given in Figure 48 at section *4.1.2*, fine meshes were generated with more than 4 million elements (See Figure 57(b)) and simulations were assumed to be grid independent.

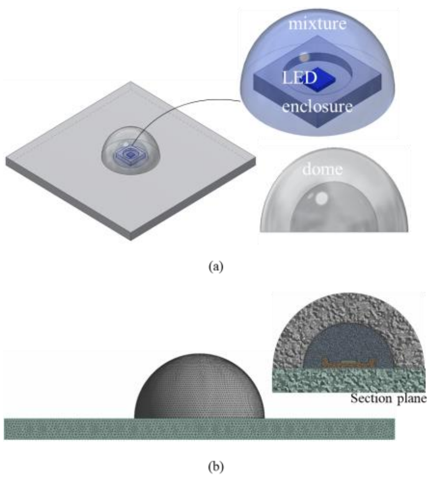

Figure 57: Validation study CFD (a) model geometry and (b) mesh distribution.

Phosphor and fluid properties given in Table 10 were adopted for the analysis. A special UDF was written (see Appendix A.3) to account for the temperature dependent viscosity variation. Moreover, material thermal conductivities of the chip (Si), mount (ceramic), dome (epoxy-glass fiber) and PCB were defined to be 180 W/m-K, 24 W/m-K, 0.17 W/m-K and 105 W/m-K respectively.

In the experimental analysis, bottom side of the LED was attached to a heat sink for effective heat dissipation. In accordance with that bottom part of the PCB was subjected to 80 W/m^2-K convective heat transfer while chip and outside dome temperature was fixed to 100 °C and 40 °C respectively. Consequently, a temperature difference of 60 °C was found matching the velocity profiles obtained from camera measurements (See Figure 58) and maximum viscosity was obtained to be 0.2 Pa.s at the close vicinity of the dome while the minimum viscosity was evaluated to be 0.1 Pa.s near the chip.

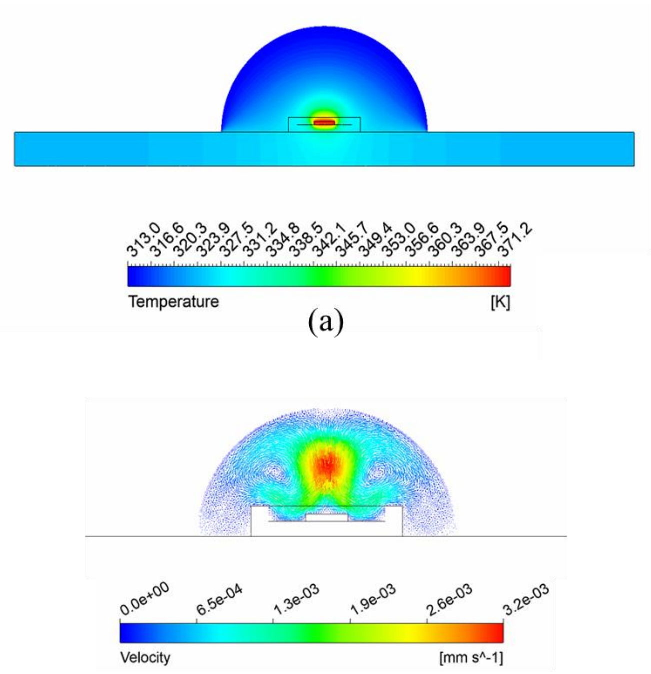

(a)

(b)

Figure 58: (a) Temperature and (b) velocity distribution within the package.

Experimentally obtained particle velocities are belong to the particles near the chip region that moves in the vertical direction from chip to the center of the mixture domain. Therefore, in CFD, particles were injected such that particle movement in vertical direction can be extracted. For the initial case, particle diameter was varied between 5 μm to 13 μm based on the size distribution of the YAG:Ce^{+3} used in the experiments (See Fig.59(b)) and average particle velocity results for each diameter case was found as shown in Figure 59(a).

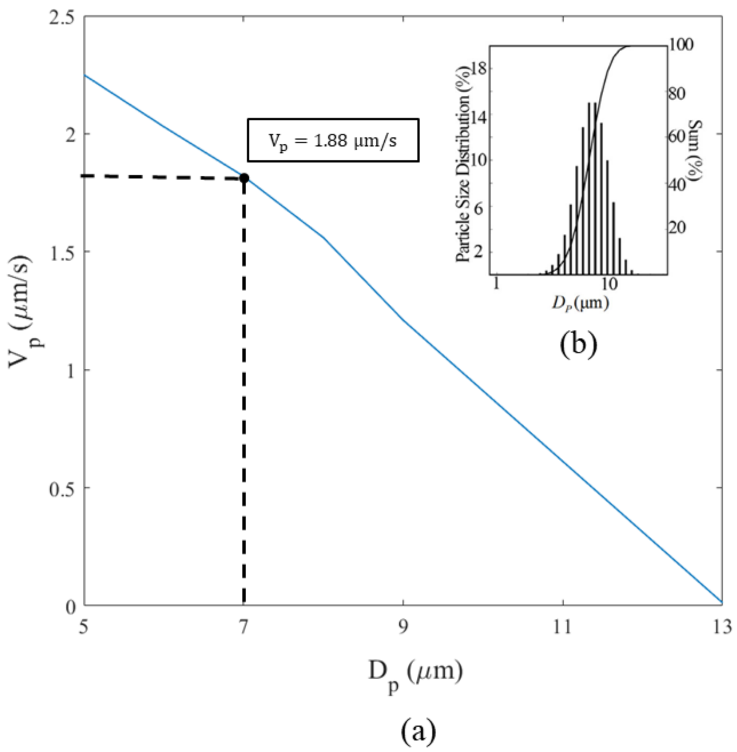

Figure 59: (a) Average particle velocity variation and (b) experimental YAG:Ce^{+3} particle size distribution.

Particle velocities for the black coated case was evaluated to be between 1.54 μm/s and 6.67 μm/s in the experiments. According to average particle velocity results given in Fig. 59(a) and particle size distribution provided by the manufacturer in Fig. 59(b), 7 μm was selected as test case to further comparison. This time particles were uniformly distributed within the package and simulations were run again for detail analysis. Two particles, ID-34 and ID-105, that moves in the vertical direction was identified and their trajectory was reported for 1000 s. Selected particles movements are shown in Figure 60(a) and Figure 60(b) for reference. As a result, obtained particle velocities (Fig. 60(c)) are within the velocity range of experimental evaluations made for particles located at similar regions (Fig. 60(d)).

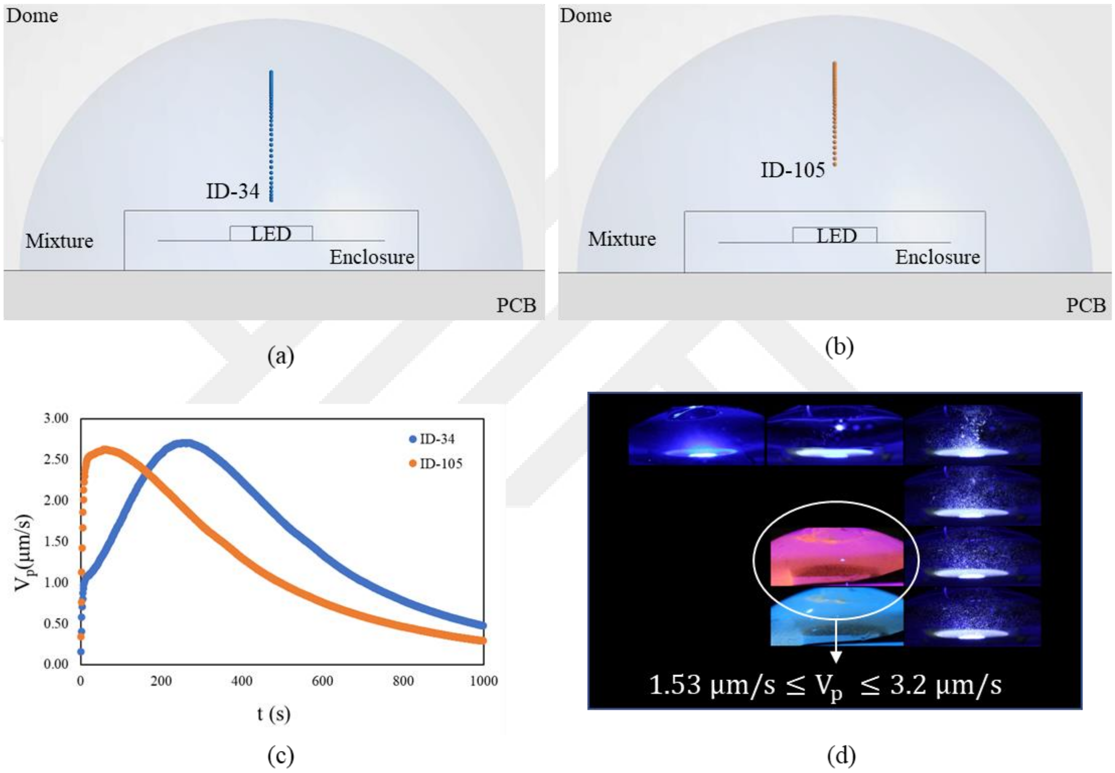

Figure 60: (a)-(b) Selected particles trajectories within the package (c) Particle velocity variations with time. (d) Experimental results.

CHAPTER V

SUMMARY AND CONCLUSIONS

Table 11: Summary of LED T_j measurement methods.

Measurement Method	Measurement Principle	Measurement Location	Advantages	Limitations
TSOP	Spectral Power Distribution	T_j	▪ Good spatial resolution ▪ No contact ▪ Direct indicator of T_j	▪ Requires expensive measurement devices ▪ Requires an unobstructed view of the surface ▪ Complex relation between temperature and the optical parameters
IR Thermography	Radiation	Unclear (Surface, bottom and etc.)	▪ Rapid response ▪ Provides temperature maps ▪ No contact	▪ Limited spatial resolution ▪ Measurement accuracy highly dependent on the ambient conditions and emissivity ▪ Calibration is necessary ▪ May require an unobstructed view of the device
Thermoreflectance	Reflectivity	Interconnections	▪ Good spatial resolution ▪ No contact ▪ Rapid response	▪ Not direct indicator of the T_j ▪ May require an unobstructed view of the device
Raman Spectroscopy	Phonon Frequency	Unclear (Semiconductor, surface and etc.)	▪ Good spatial resolution ▪ No contact (if Raman active particle coatings are not used)	▪ Slow acquisition time ▪ May require an unobstructed view of the device
Liquid Crystal	Hue	Surface	▪ Relatively good spatial resolution ▪ Low cost	▪ Thermal spreading effect disturbs the measurement ▪ Subjective evaluation is necessary ▪ Temperature resolution is limited to the transition temperature of the liquid crystal ▪ Not direct indicator of the T_j
TSEP	Electrical	T_j	▪ Can be used on packaged LED ▪ No contact ▪ Direct indicator of T_j	▪ Measures the average T_j ▪ Prior calibration of the V_f is needed
Thermocouple Thermometry	Seebeck Effect	Surface or Solder Point	▪ Low cost ▪ Readily available ▪ Fast response	▪ Limited resolution ▪ Requires direct contact and therefore an invasive approach ▪ Not direct indicator of the T_j
MNP Thermometry	Magnetic Field	Surface	▪ Promising new approach for temperature measurement of non-transparent objects	▪ Limited temperature accuracy ▪ Not direct indicator of the T_j

A comparative study is conducted to analyze high-power LED devices' transient and dynamic opto-thermal behavior. An accurate and time-efficient forward voltage-based junction temperature monitoring method was presented in slow and uninterrupted heating and cooling controlled experiments. The presented thermal characterization approach was developed by taking the drawbacks of the current conventional experimental junction temperature measurement approaches into account and addressing the issues in non-ideal thermal calibration processes discussed in the literature. For comparison purposes, a detailed review composed of a large number of summaries on junction temperature of LEDs while disadvantages and advantages inherent to each technique based on the findings presented in literature were given as a reference in Table 11.

Experimental findings of the FVM based temperature sensitivity measurements can be summarized as follows:

- Significant linear accuracy at a forward pulse current of 1 mA was observed even at temperatures above 100 °C.

- From 1 to 10 mA pulse currents, acceptable temperature rise in short pulse durations was seen. In contrast, 100 mA pulses, if not performed in 1 ms, resulted in wrong calibrations due to significant temperature rise during the pulse period.

- As the interval between pulses decreased to 10 s, and below, temporal testing with FVM to perform optical and thermal transient analysis showed interruption in the device's natural temperature rise and optical measurements.

- Without immersion cooling, for drive currents of 300 mA to 700 mA, efficiencies higher than 35% cannot be achieved in useful emission power levels due to Auger losses that reduce internal quantum efficiency and interfacial thermal resistances in thermal designs.

Correspondingly, a new cost-effective cooling solution that can directly target chip and phosphor was offered as a viable option to dissipate a vast amount of heat, ensuring a uniform distribution of temperature and removal of local hot spots in high brightness and high power LEDs. Moreover, a technique for preparation of immersion cooled LED packages with dispersed particles was demonstrated and a preliminary experimental setup was built for particle velocimetry measurements of phosphor particles.

Based on the particle based experimental analysis of new transparent millimeter scale passive cooled immersed photoluminescent LED packaging, phosphor particle motion was monitored under different conditions. As a consequence, following conclusions can be made and recommendations can be offered:

- More than 10-fold increase in particle velocity can observed in the presence of LED light.
- The particle inertia, drag and gravity are the primary forces that induces particle motion under buoyancy flow, however, another force named photopheresis was found to have more significance influence over the particle kinetic energy when blue light emission incorporated.
- Although the origins of this photopheresis can not be concluded yet (temperature or accommodation coefficient variaiton), intense photopheresis effect that alters liquid can be reported for micron scale particles immersed in a viscous fluid.

In addition, an opto-thermal coupled numerical model that characterizes the behavior of immersed phosphor particles under natural convection flow was also presented. The proposed dynamic model enables closer examination of the location dependent self-heating of phosphor with light interaction, which can also be used for other SSL devices that utilizes phosphor for white light generation. Various chip heat generation rates, initial particle positions, particle sizes, injection numbers, and boundary conditions were examined within this scope. Particle energy levels, temperatures, and trajectories were recorded, and results were presented. In the preliminary analysis, the mixture domain was divided into three hemispherical regions depending on the dominance of natural convection currents and flow behavior inside the carrier fluid.

Furthermore, in advanced numerical models where particle self-heating effect was considered, the primary focus has been given to the near chip region within a 1 mm^3 where more than 5 K/mm temperature gradient was observed. Particle kinetic energy levels and velocities were closely examined within the near scale for various particle sizes and injection numbers. Based on the DPM modeling approach with locally variable self-heating particles immersed in dielectric fluid, the following findings can be presented to shed light on improving the performance of Pc-WLED devices by controlling the distribution of circulating phosphors at optically and thermally favorable positions:

- The temperature rise of optical fluid in the package can reach up to 95 °C if particles with a diameter of 45 μm and volume fraction of 1.5E-08 travel as close as 0.05 mm above the LED chip surface.

- Due to the Lambertian emission profile of the LED, particle-light interactions were found to be more intense in the vertical. If the particle moves in the close vicinity of the dome, the rate of heat generation of a particle was less than 0.01 μW due to low irradiance levels.

- The numerical analysis results have shown that depending on the particle size and position, individual phosphor particles may follow a different trajectory, and the probability of obtaining blue light emission may differ.

- If the volume fraction of the phosphor particles is kept equal for different particle sizes, lightweight particles were observed to cover greater distances in far scale regions with higher blue light emission probability.

CHAPTER VI

RECOMMENDATIONS FOR FUTURE WORK

Future studies can focus on generalized temperature prediction models that can be developed with machine learning algorithms. Considering the consistent behavior of temperature sensitive optical parameters for blue and phosphor converted LED chips, established estimation models can be based on the temperature response of spectral power distribution, luminance flux, and correlated color temperature of LEDs at nominal current densities.

Moreover, special attention can be given to introducing new cost-effective thermal management methods. The proposed immersion cooling technique can be extended to other solid-state lighting devices. For instance, laser diodes can achieve higher power conversion efficiencies at higher current densities. With the implementation of an efficient active thermal cooling solution and reduction in internal resistances, laser diodes can outperform current LED devices in general high performance lighting applications.

In addition, phosphor particle light interaction, behavior of a thermocapillary flow and photopheresis force effect can be further explored with more advanced microscopic flow tracking techniques, and novel systems can be proposed for control of phosphor particle distribution to realize the full potential of Pc-WLEDs for high brightness illumination and to integrate it to the conventional packaging.

APPENDIX A

A.1 MATLAB Code for Particle Injections

```
% clc;
% clear all;
%
function GeneratFluentParticlesInjectionFile()
last_matrix = [];

%particle initial conditions
diameter=15e-6;   % unit meter
temperature=293; % unit  K
density=997;  % unit: kg/m3
mass_flow =0;
x_vel=0;  % unit m/s
y_vel=0;
z_vel=0;

mrgn = 0.0015;
% mrgn2 = 0.0005;
z_bott_marg = 0.59551*10^(-3); %m, distance between min z of mixture and max z of
chip
center_x = -0.001069181;
center_y = 0;
center_z = 0.00168366 + z_bott_marg + mrgn;
diameter_xyz = 18*10^(-3);


length_x = diameter_xyz/2-mrgn;
length_y = diameter_xyz/2-mrgn;
length_z = diameter_xyz/2-z_bott_marg-2*mrgn;
delta_x = 0.0013; %2 mm distance between each particle in x
delta_y = 0.0013; %2 mm distance between each particle in y
delta_z = 0.0013; %2 mm distance between each particle in z

injectionName='ellipsoidinjection53p25';
id=0;

f=fopen('ellipsoidinjection53p25.inj','w'); % initial introduction field
% fprintf(f,'((x y z u v w temperature diameter mass-flow) %s :ID )',injectionName);
% fprintf(f,'n');

for z = center_z:delta_z:center_z+length_z
for y = center_y-length_y:delta_y:center_y+length_y
for x = center_x-length_x:delta_x:center_x+length_x
matrix = [x y z];
if (x-center_x)^2/(length_x)^2 + (y-center_y)^2/(length_y)^2 + (z-
center_z)^2/(length_z)^2 <= 1
```

```
		last_matrix = vertcat(last_matrix,matrix);
		mass_flow = (1/6.0*pi)*diameter*diameter*diameter*density;
end
end
end
end

last_matrix(1,:)= [];
last_matrix(21,:)= [];
last_matrix(29,:)= [];

for i = 1:length(last_matrix)
		current = last_matrix(i,:);
		fprintf(f,'((%e %e %e %f %f %f %f %f %e) %s : %i
)',current(1),current(3),current(2),x_vel,z_vel,y_vel,diameter,temperature,mass_flow,inj
ectionName,id);
		fprintf(f,'\n');
		id=id+1;

end

disp(id);
disp('particles has been defined');
fclose(f);

scatter3(last_matrix(:,1),last_matrix(:,2),last_matrix(:,3),'MarkerEdgeColor','[0.9290
0.6940 0.1250]','MarkerFaceColor','y')
hold on
xlabel('x','FontSize',15);
ylabel('y','FontSize',15);
zlabel('z','FontSize',15);
% view(0,90)  % XY
% pause
view(0,0)   % XZ
% pause
% view(90,0)  % YZ
hold on
[x ,y ,z ] = sphere;      %# Makes a 21-by-21 point sphere
x = x(11:end,:);       %# Keep top 11 x points
y = y(11:end,:);       %# Keep top 11 y points
z = z(11:end,:);       %# Keep top 11 z points
r = 9*10^(-3);                 %# A radius value
surf(r.*x-0.001069181,r.*y+0,r.*z+0.00168366,'FaceColor','[0 0.5 1]','FaceAlpha',0.1);
%# Plot the surface
axis equal;            %# Make the scaling on the x, y, and z axes equal
hold on

min_x = min(last_matrix(:,1));
max_x = max(last_matrix(:,1));
min_y = min(last_matrix(:,2));
```

```
max_y = max(last_matrix(:,2));
min_z = min(last_matrix(:,3));
max_z = max(last_matrix(:,3));

end
```

A.2 UDF for Particle Temperature

```
#include "udf.h"

#include "dpm.h"

#define CP_PHOSP 590          /*Specific Heat of Phosphor*/

/*Center coordinates*/

#define x_c -0.001069181

#define z_c 0

#define y_c 0.00231667

/* Pr Number *\

#define Pr 412

/* Heat Generation Value *\

#define Q1 3.83E-05

#define Q2 3.78E-05

/* You can add here as much as Q as needed *\

DEFINE_DPM_LAW(particle_heat,tp,ci)

{

/* Get Cell and Thread from Particle Structure */

  cell_t c = TP_CELL(tp);

  Thread *t = TP_CELL_THREAD(tp);

real Re, Nu, h, R, Q


real x = TP_POS(tp)[0];

real y = TP_POS(tp)[1];

real z = TP_POS(tp)[2];
```

```
real r_x = fabs((x)-(x_c));

real r_y = fabs((y)-(y_c));

real r_z = fabs((z)-(z_c));


Re =((C_V(c,t)* TP_DIAM(tp) * TP_RHO(tp))/C_MU_L(c,t));

Nu = (2.0 + 0.66 * sqrt(Re) * pow(Pr, 1.0/3.0))); /* Nusselt Number Correlation to be used *\

h = (Nu * C_K_L(c,t)) / TP_DIAM(tp); /* Heat Transfer Coefficient *\

R = 1/(h*4*M_PI*pow((TP_DIAM(tp)/2), 2));


if(A>r_x && r_x>= B && C >r_z && r_z>=D && E>r_y && r_y>=F)

/* A to L are locations within the fluid domain and should priorly determined based on the computational case and particle diameter *\

{

TP_T(tp) = C_T(c,t)+ Q1*R

}

else if(G >r_x && r_x>=H && I>r_z && r_z>= J && K >r_y && r_y>= L)

{

TP_T(tp) = C_T(c,t) + Q2*R;

}

/* You can add here else if as much as required *\

/* The effect of heat generation should be identified priorly to decide on the particle location limits *\

else

{

 TP_T(tp) = C_T(c,t); /* Based on the location of interest all other particle's temperature can be set to fluid temperature *\

}

}

DEFINE_DPM_SOURCE(dpm_source, c, t, S, strength, tp)
```

```
{
S->energy = TP_MASS(tp)*CP_PHOSP*(TP_T(tp)-C_T(c,t)); /* Add a source term to the energy equation *\
}
```

A.3 UDF for Temperature Dependent Fluid Viscosity

```
#include "udf.h"
 DEFINE_PROPERTY(cell_viscosity,c,t)
 {
   real mu_lam;
   real temp = C_T(c,t); /* Cell Temperature *\
   mu_lam =exp(-6.96+1760/temp); /* Temperature Dependent Viscosity *\
return mu_lam;
}
```

APPENDIX B

B.1 Uncertainty Analysis of Temperature Measurements

Uncertainty evaluations of the junction temperature measurements can be conducted by accounting for the accuracy and resolution of the devices of EVATHERM systems and calculating the standard deviations in each repeated measurement.

The uncertainties accompanied by the measurement instrument is known as Bias error (B) or systematic error [294]. The formulation given in Equation 24 can be used to calculate the bias error based on the data provided by the device or system manufacturer. In the equation, R represents the resolution while A stands for the accuracy of the device. It should be noted that calibration of the instruments can reduce the uncertainty, but bias error accompanied with the measurement can not be eliminated.

$$B = \pm[(0.5R)^2 + (A)^2]^{0.5} \tag{24}$$

Table 12: Bias error evaluation for the T_j measurements.

Equipment (Variable)	Resolution	Accuracy	Bias Error
Sourcemeter (V_f)	0.00001	0.001375	± 0.001375009
Sourcemeter ($I_{f,p}$)	0.00002	0.006	± 0.006000008
Sourcemeter (I_f)	0.02	1.9	± 1.900026316
Sourcemeter (t_c and t_p)	0.001	0.005	± 0.005024938
Thermocouple (T_j)	0.1	1	± 1.001249220
Oven System (T_j)	-	0.5	± 0.5
Computer (T_j)	0.1	0.015	± 0.052201533

Since the instruments of the EVATHERM system comes with calibration certificates, resolution and accuracy values provided by the manufacturer are summarized in Table 12 and correspondingly used to calculate the total bias error with 95% confidence interval. Precision error (P) calculations are based on the mean standard deviation (σ_x) of the measured data and t-distribution (Eq.25 and Eq.26). Statical fluctuations that arise from the repeated measurements are accounted at this stage and evaluations are made considering the total number of measurements (n) and the measurement outcome (x).

$$\sigma_x = \frac{\left[\frac{\sum_{i=1}^{n}(x_i - x_{ave})^2}{n-1}\right]^{0.5}}{\sqrt{n}} \tag{25}$$

$$P = t_{(n-1)}\sigma_x \tag{26}$$

Precision calculations should be made for each dependent variable individually. If an experimental variable is used in the calculations of a group of measurement data, then the precision error accompanied with each group of data must be determined prior to final precision error evaluation [295]. A similar approach should also be used for the bias error evaluations. Following that, both bias and precision errors are combined to find the absolute uncertainty value for the measurement (see Equation 27).

$$U = \pm[B^2 + P^2]^{0.5} \tag{27}$$

B.2 Uncertainty Analysis of Optical Measurements

For the optical measurements conducted utilizing an integrating sphere system, uncertainty calculations of the spectrometer, reference lamp, and power supplies are made based on the certifications issued by the accredited institutions, reference documents provided by the manufacturers, and compound and extended uncertainty evaluations. In addition, environmental variations in the lab during the measurements are accounted for by making the arithmetic mean standard deviation (Eq. 25) calculations for the repeated measurements. For all the uncertainty comp, rectangle (uniform) or normal distribution is considered. These probability distributions reveal frequency of the measurement interval and are calculated with the following formulations:

$$\text{Rectangular: } u(x_i) = \frac{c_i}{\sqrt{3}} \quad (28)$$

$$\text{Normal: } u(x_i) = \frac{c_i}{d} \quad (29)$$

Where $u(x_i)$ is the standard measurement uncertainty, c_i is the reference uncertainty obtained from the data sheets for the equipment, and d is the convergence factor.

Table 13: Optical measurement uncertainties.

Reference Device or Related Uncertainty Components	Given or Expected Data	Distribution Type	Standard Measurement Uncertainty	Sensitivity Constant	Uncertainty Constant	Variant
Spectrometer (Wavelength Calibration)	0.7	Normal	0.35	1	0.35	0.1225
SCL 1400 Lamp	1.0	Normal	0.5	1	0.5	0.25
LPS 150 Power Supply (Direct Voltage)	0.005	Normal	0.0025	1	0.0025	0,00000625
LPS 150 Power Supply (Direct Current)	0.005	Normal	0.0025	1	0.0025	0,00000625
LPS 100 Power Supply (Direct Voltage)	0.005	Normal	0.0025	1	0.0025	0,00000625
LPS 100 Power Supply (Direct Current)	0.005	Normal	0.0025	1	0.0025	0,00000625
Agilent Power Supply (AC Voltage)	0.06	Normal	0.03	1	0.03	0,0009
Agilent Power Supply (Frequency)	0.01	Normal	0.005	1	0.005	0,000025
SCL 1400 Lamp Lifetime Uncertainty Constant Spectrometer	3,2332E-05	Rectangle	1,8667E-05	1	1,8667E-05	3,4844E-10
Spectrometer Non-linearity Uncertainty Constant	0,06	Normal	0.03	1	0.03	0.0009
Spectrometer Light Leakage Uncertainty Constant	0.05	Rectangle	0,02886751	1	0.02886751	0,00083333
Spectrometer Drift Based Uncertainty Sphere	0.05	Normal	0.025	1	0.025	0,000625
Sphere Space Absorptivity Uncertainty Constant	0.5	Normal	0.25	1	0.25	0.0625
Sphere Non-uniformity Uncertainty Constant	0.2	Normal	0.1	1	0.1	0.01
Method Based Uncertainty						
Temperature Based Uncertainty	0,77558493	Rectangle	0,44778417	1	0,44778417	0,20051066
Air Velocity Based Uncertainty	0	Rectangle	0	1	0	0

Based on the measurement type (Luminous flux, CCT, and CRI) the following uncertainty results are obtained.

Table 14: Luminous flux (Lm) measurement uncertainty.

	Given or Expected Data	Distribution Type	Standard Measurement Uncertainty	Sensitivity Constant	Uncertainty Constant	Variant
Experiment Repeatability Based Uncertainty	2,51197134	Normal	1,25598567	1	1,25598567	1.5775
						Total: 2.61
Overall Measurement Uncertainty:	**1.62**					
Expanded Measurement Uncertainty	**3.23**					

Table 15: CCT measurements uncertainty.

		Given or Expected Data	Distribution Type	Standard Measurement Uncertainty	Sensitivity Constant	Uncertainty Constant
Experiment Repeatability Based Uncertainty	3.46	Normal	1,73	1	1,73	2.9929
						Total: 9.02
Overall Measurement Uncertainty:	**3.02**					
Expanded Measurement Uncertainty	**6.01**					

Table 16: CRI measurements uncertainty.

		Given or Expected Data	Distribution Type	Standard Measurement Uncertainty	Sensitivity Constant	Uncertainty Constant
Experiment Repeatability Based Uncertainty	2,51197134	Normal	1,25598567	1	1,25598567	1.5775
						Total: 2.61
Overall Measurement Uncertainty:	**1.62**					
Expanded Measurement Uncertainty:	**3.23**					

APPENDIX C

Thermal and Optical Characterization of White and Blue Multi-Chip LED Light Engines

A clear understanding of thermal characteristics for LEDs is at the center of attention for lighting industry. Especially accurate evaluation of the junction temperature of various light engines is the subject matter for last two decades. Nonetheless, viability of the priorly offered solutions is still an argument and only a few of them are practical enough for the extensive practices. Therefore, in this research, utilization of a new multi-LED chip junction temperature measurement technique is studied through thermal characterization of a commercially available MR16 solid-state light lamp.

MR16 LED lamps are mainly composed of several LEDs (in this study 3 LEDs) a MR lens array, metal core printed circuit board (MCPCB) substrate, physical frame with attached heatsink, and driver. Internal reflection (TIR) and multifaceted reflector (MR) enables optical control by collimating the light coming from the LED to create a concentrated beam of light. Since three relatively high-power LEDs are embedded to a compact design criterion and are enclosed by a MR lens, effective thermal management is necessary for their reliable performance.

C.1 Forward Voltage Method Multi-Chip Temperature Measurements

For the experimental preparation, optical cap of the MR16 was disassembled, and lens was removed from the package (see Figure 61(a)). To control each LED individually, connection wires were soldered to the LED terminals using WXR3 Weller soldering station with 200μm soldering tip (see Figure 48(b)). Soldered connection wires are shown under microscope in Figure 48(c).

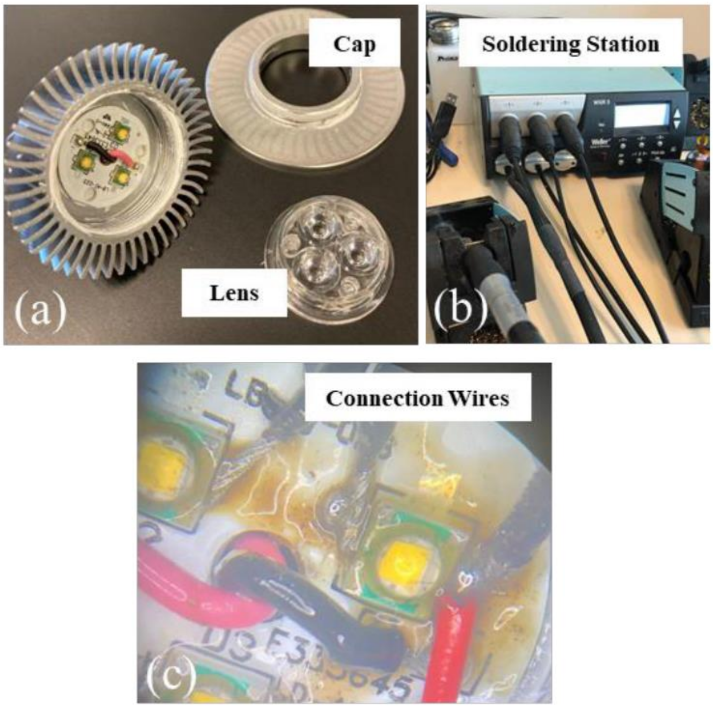

Figure 61: Soldering process of individual connection wires to multi-chip MR16 LED.

Forward voltage change method is employed using EVAtherm junction temperature measurement system. Test system with MR16 placed inside is shown in Figure 62. Similar to the previous FVM thermal characterization investigations presented in this thesis, temperature adjustable oven system (see Figure 62(a)) is used to alter chip temperature while providing isothermal condition. As two T-type thermocouples inside the over record temperature variations, after reaching state at a specified temperatures for 5 minutes, a small pulse current (1 mA for 1 ms) with negligible heat generation effect is applied to each LED and corresponding FV values are recorded.

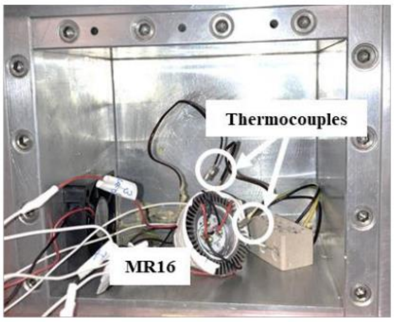

(a)

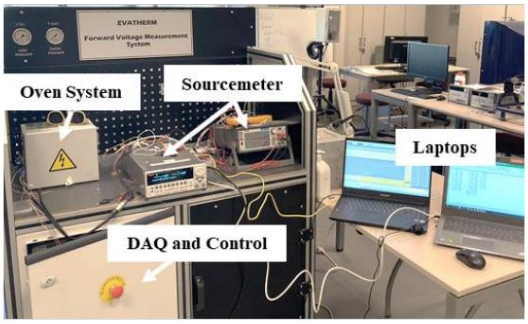

(b)

Figure 62: (a) Inside view of the oven and (b) forward voltage measurement system.

In the second part of the experimental analysis (Test phase) FV readings of the LEDs at the actual MR16 operating conditions are conducted to determine the T_j. Different from FVM approach for single chip devices, the PCB is connected to the first channel of sourcemeter and one LED is connected to the second channel for temperature measurement of multi-LED MR16 lamp. Using the first channel, electric circuit of the MR16 is powered with 8.21V (actual working condition) and all three LEDs are lightened up. It should be mentioned that this voltage value is forced by the driver board implemented by the manufacturer, and the aim is to limit the main forward voltage of the LEDs reaching to this value or lower. Next, first channel is switched off for 1ms and simultaneously second channel is used to pulse the selected LED with 1mA for 1ms and forward voltage values are recorded. This process is performed separately for each LED of MR16 and test phase is conducted in different time intervals. This way temperature variation of LEDs after running the MR16 at room temperature until reaching steady state can be recorded.

C.2 Infrared (IR) Thermography Measurements

For the thermal imaging measurements, MR16 is placed under a cooled mid-wave FLIR SC5000 IR camera with a wavelength range of 2.5 to 1.5µm, and a resolution of 640x512. To not alter the time dependent behavior of the MR16 LED, IR camera is calibrated with FV measurement results and calibration variables obtained accordingly. First, PCB is powered for 5, 10 and 15-minute time intervals and test phase are applied to the third LED as explained in the FV measurements and corresponding junction temperature at each time step is evaluated. Transient FV measurement results and transient IR thermography results are matched, and calibration parameters are determined from the best fit data. After calibration of IR camera, time dependent behavior of LEDs in MR16 are evaluated in different time scales. Experimental setup for the IR thermography measurements are shown in Figure 63.

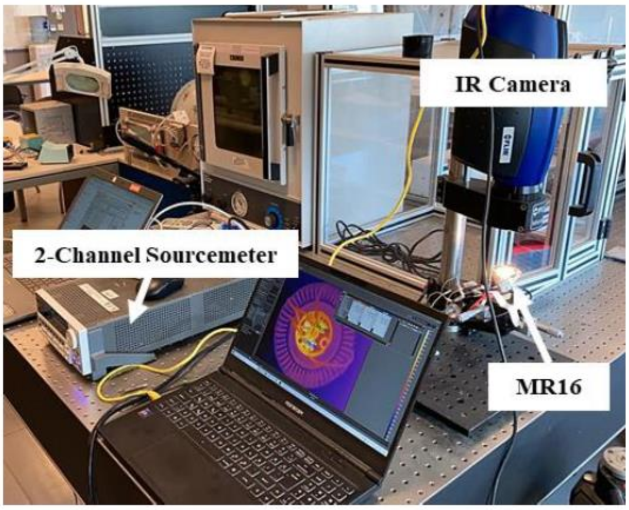

Figure 63: IR Camera and two channel forward voltage measurement experimental setup.

C.3 Optical Measurements

A further experimental study has been performed to determine the optical characteristics of the MR16 lamp. LabSphere Illumia Plus 610 brand integrating sphere system is used for the measurement (see Figure 64). The device contains a CDS-610 model detector and 2-meter diameter sphere which was painted with reflective coating with emissivity over 0.98. First, calibration of the system is made under pre-defined limits, using a reference lamp with known optical parameters. After that for the actual measurement, MR16 LED is positioned at center of the sphere on top of a holder with low thermal conductivity (0.2 W/m-K). Total radiant flux of the MR16 multi-LED is measured and the spectral distribution of the MR16 LED is formed. As a result, two different peak wavelengths are observed in the spectral distribution graph (see Figure 65). 450 nm is from blue light coming from the chip and 650 nm is for the white light after phosphor conversion. Total optical power of the multi-chip MR16 LED is measured as 0.695W.

Figure 64: Integrating sphere system with MR16 positioned at the center.

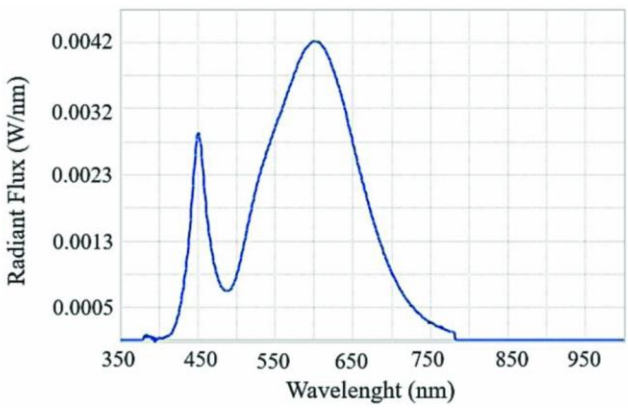

Figure 65: Spectral distribution of MR16 LED at operating condition.

Further experimental data of flux, maximum intensity, CRI, CCT, and view angle of single LED and MR16 are provided in Table 17. As it can be seen from table, implemented TIR lens in the MR16 resulted in ray collimation that increases max intensity significantly, however 19% of flux is reduced due to the optical losses in the process.

Table 17: Optical properties of the Multi-LED MR16 lamp.

Parameter	Value
Flux of Single LED (lm)	80.6
Flux of MR16 (lm)	195
CRI	81.33
CCT (K)	3044.3
Max intensity of single LED without TIR lens (cd)	29.96
Max intensity of MR16 (cd)	1513
View Angle (°)	15

C.4 Results and Discussions

A linear relationship between Vf-Tj is shown in Figure 66. Calibration equations were derived for each LED (see Eq.30). Constant parameter "A" for LED1-2-3 is found to be -0.001319, -0.001397, -0.001350 and constant parameter "B" is calculated as 2.519, 2.505 and 2.513 respectively. For junction temperatures between 20 °C-100 °C the forward voltage change interval is found to be between 2.38-2.49 V. Using this relation one can calculate the junction temperature at the actual operating conditions by measuring the forward voltage.

$$V_f = -AT_j + B \tag{30}$$

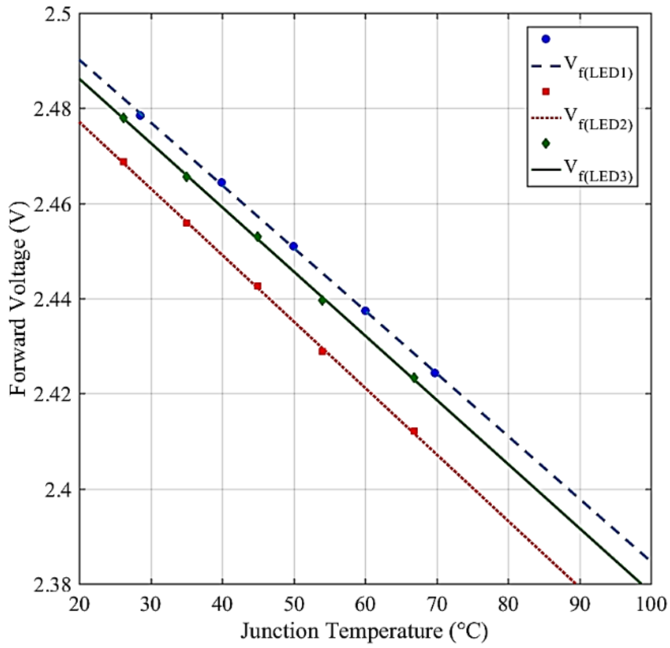

Figure 66: Variation of T_j with V_f.

Time depending junction temperature characterization of LEDs using IR and FV method from initial time to reaching the steady state is presented in Figure 67. Since the FV characterization in multi-chip configuration requires turning off LEDs, even though for fraction of seconds, it can affect the time dependent thermal behavior of the device.

Thus, only three verification FV measurements have been made in 300, 550 and 900s after powering the MR16 to check the accuracy of IR thermography. Verifications are performed for one LED only.

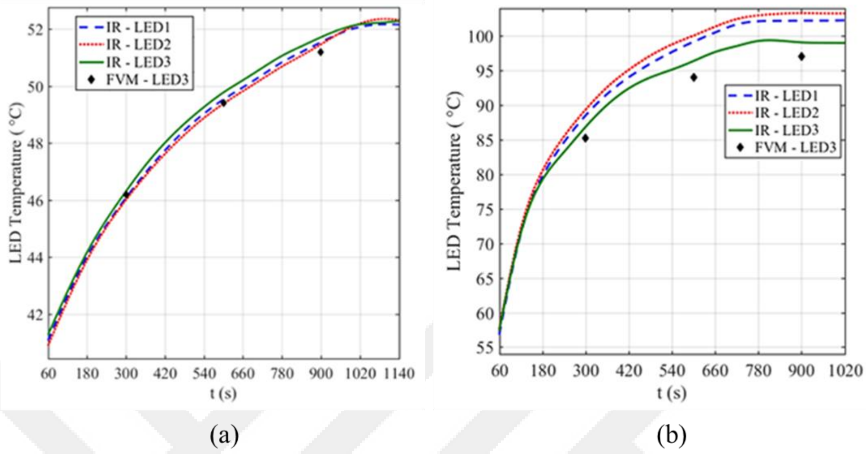

Figure 67: Variation of LED surface and junction temperatures with time calibrated IR thermography with forward voltage method of MR16 LED (a) with heat sink (b) without heatsink.

As it can be seen in Figure 67(a) for the case that heat sink was attached to the device, LEDs presented similar thermal response and negligible difference between FV and IR results can be seen, indicating the successful calibration of IR camera. Removing the heatsink from the MR16 resulted in significant temperature rise of the chips, shown in Figure 67(b). This issue indicates the importance of having suitable heat transfer mechanism in where LEDs are closely spaced in a shared board. Without heatsink junction temperature can reach up to 97 °C while with the heat sink this value reduces down to 53 °C. Moreover, it can be seen that steady state is reached in shorter time due to inclusion of smaller mass in comparison to the previous case. An order of increase can be seen in the junction temperature due to removal of heatsink.

A closer look at Figure 67, one can also conclude that FVM introduced herein can also be used for the time dependent temperature characterization of multi-chip devices when there is no fluctuation in electrical performance of LED. This method can be utilized for multi-chip systems with 20 s interval without altering the steady performance of the chips since 1 ms power off time scale would not result in noticeable thermal change in steady temperature increase of the chip.

To conclude, findings of this research has shown that accurate junction temperature estimation of multi-LED systems with FVM relies on individual handling of each LED within the system. Since the measured forward voltages are different for the three LEDs, average temperature assumptions for the MR16 LED system is not a sufficient method to determine the T_j. According to the results presented, proposed FVM based multi-LED Tj measurement method is suitable for thermal performance assessment of complex multi-LED light engines including the commercially available LED lamps.

REFERENCES

[1] K. S. Brown et al., “Fire as an engineering tool of early modern humans,” Science, vol. 325, no. 5942, pp. 859–862, 2009.

[2] S. R. James et al., “Hominid use of fire in the Lower and Middle Pleistocene: A review of the evidence [and comments and replies],” Curr. Anthropol., vol. 30, no. 1, pp. 1–26, 1989.

[3] Pyne, S. J., 2019, *Fire: A Brief History*, University of Washington Press.

[4] DiLaura, D., 2008, “A Brief History of Lighting,” Opt. Photonics News, **19**(9), pp. 22–28.

[5] Shivelbusch, W., 1989, *The Industrialization of Light in the Nineteenth Century*, University of Californai Press.

[6] Bowers, B., and Anastas, P., 1998, *Lengthening the Day: A History of Lighting Technology*, Oxford University Press Oxford.

[7] “The Historical Evolution of Lighting.” stouchlighting.com. https://www.stouchlighting.com/blog/the-historical-evolution-of-lighting (accessed March 1, 2022).

[8] “The Secret History of ‘Bonfire.” merriam-webster.com. https://www.merriam-webster.com/words-at-play/the-secret-history-of-bonfire (accessed March 1, 2022).

[9] S. Weigand, “Cresset Giving Light” pixels.com. https://pixels.com/featured/cresset-giving-light-sally-weigand.html (accessed March 1, 2022)

[10] “History of Candles-Development and History of Candle Making.” historyoflighting.net. http://www.historyoflighting.net/lighting-history/history-of-candles/ (accessed March 1, 2022).

[11] “The History of the Light Bulb.” delmarfans.com. https://www.delmarfans.com/educate/basics/who-invented-light-bulbs/ (accessed March 1, 2022).

[12] Schubert, E. F., and Kim, J. K., 2005, “Solid-State Light Sources Getting Smart,” Science, **308**(5726), pp. 1274–1278.

[13] Chen, K., and Murray, W. A., 1980, “Energy, Incandescent Lighting, and 100 Years,” IEEE Trans. Ind. Appl., **IA-16**(3), pp. 413–419.

[14] Widagdo, S., 2006, “Incandescent Light Bulb: Product Design and Innovation,” Ind. Eng. Chem. Res., **45**(25), pp. 8231–8233.

[15] Rubin, M. B., 2010, “The Development of the Mercury Lamp,” Bull. Hist. Chem., **35**(2), p. 105.

[16] Schubert, E. F., 2006, *Light-Emitting Diodes*.

[17] S. Yurchuk, O. Rabinovich, and S. Didenko, “LED and Phototransistor Simulation.” intechopen.com. https://www.intechopen.com/chapters/55943 (accessed March 10, 2022)

[18] Novikov, M. A., 2004, “Oleg Vladimirovich Losev: Pioneer of Semiconductor Electronics (Celebrating One Hundred Years since His Birth),” Phys. Solid State, **46**(1),

pp. 1–4.

[19] Lossev, O. V, 1928, “CII. Luminous Carborundum Detector and Detection Effect and Oscillations with Crystals,” London, Edinburgh, Dublin Philos. Mag. J. Sci., **6**(39), pp. 1024–1044.

[20] “Invention History of Light Emitting Diode (LED).” circuitstoday.com. https://www.circuitstoday.com/invention-history-of-light-emitting-diode-led (accessed March 11, 2022).

[21] Okon, T. M., and Biard, J. R., 2015, “The First Practical LED,” Edison Tech Cent., **9**.

[22] Humphreys, C. J., 2008, “Solid-State Lighting,” MRS Bull., **33**(4), pp. 459–470.

[23] 2012, “LED Inventor Nick Holonyak Reflects on Discovery 50 Years Later,” LED Prof.

[24] D. A. Steigerwald et al., “Illumination with solid state lighting technology,” IEEE J. Sel. Top. Quantum Electron., vol. 8, no. 2, pp. 310–320, 2002, doi: 10.1109/2944.999186.

[25] Perry, T. S., 1995, “M. George Craford [Biography],” IEEE Spectr., **32**(2), pp. 52–55.

[26] Shur, M. S., and Zukauskas, R., 2005, “Solid-State Lighting: Toward Superior Illumination,” Proc. IEEE, **93**(10), pp. 1691–1703.

[27] Akasaki, I., 2007, “Key Inventions in the History of Nitride-Based Blue LED and LD,” J. Cryst. Growth, **300**(1), pp. 2–10.

[28] O. Graydon et al., 2007, “Haitz’s Law,” Nat. Photonics, **1**(1).

[29] “2014 Nobel Prize in Physics.” nobelprize.org. https://www.nobelprize.org/ (accessed March 20, 2022).

[30] Y. Narukawa et al., “Ultra-High Efficiency White Light Emitting Diodes,” Jpn. J. Appl. Phys., vol. 45, no. No. 41, pp. L1084–L1086, 2006, doi: 10.1143/jjap.45.l1084.

[31] Rossow, M., 2016, “Introduction to Solid-State Lighting (LEDs) Credit: 3 PDH Introduction to Solid-State Lighting (LED) Technology,” (877).

[32] Inc. Navigant Consulting, 2014, “Energy Savings Forecast of Solid-State Lighting in General Illumination Applications,” U.S. Dep. Energy Rep., (December), pp. 2013–2014.

[33] Kim, J., and Schubert, E. F., 2008, “Transcending the Replacement Paradigm of Solid-State Lighting,” Opt. Express, **16**, pp. 21835–21842.

[34] “Working Principle of Light Emitting Diode.” electrical4u.com. https://www.electrical4u.com/working-principle-of-light-emitting-diode/ (accessed March 27, 2022)

[35] Pierret, R. F., 1996, *Semiconductor Device Fundamentals*, Pearson Education India.

[36] Liu, S., and Luo, X., 2011, *LED Packaging for Lighting Applications: Design, Manufacturing, and Testing*, John Wiley & Sons.

[37] Odoh, E. O., and Njapba, A. S., 2015, “A Review of Semiconductor Quantum Well Devices,” Adv Phys Theor Appl, **46**, pp. 26–33.

[38] Mohammad, S. N., and Morkoç, H., 1996, “Progress and Prospects of Group-III Nitride Semiconductors,” Prog. quantum Electron., **20**(5–6), pp. 361–525.

[39] N. Bardsley et al., 2014, “Solid-State Lighting Research and Development Multi-Year Program Plan,” US Dep. Energy.

[40] Liu, Z., 2008, “New Approach for 1w High Output LED Package Using 3D Lead Frame,” *Solid State Lighting and Solar Energy Technologies*, SPIE, pp. 161–167.

[41] Kennedy, D. P., 1960, “Spreading Resistance in Cylindrical Semiconductor Devices,” J. Appl. Phys., **31**(8), pp. 1490–1497.

[42] M. Razavi et al., 2016, “Review of Advances in Thermal Spreading Resistance Problems,” J. Thermophys. Heat Transf., **30**(4), pp. 863–879.

[43] S. Nishiura et al., 2011, “Properties of Transparent Ce: YAG Ceramic Phosphors for White LED,” Opt. Mater. (Amst)., **33**(5), pp. 688–691.

[44] Azarifar, M., Cengiz, C., and Arik, M., 2020, “Particle Based Investigation of Self-Heating Effect of Phosphor Particles in Phosphor Converted Light Emitting Diodes,” J. Lumin., **231**, p. 117782.

[45] Luo, X., Fu, X., Chen, F., and Zheng, H., 2013, “Phosphor Self-Heating in Phosphor Converted Light Emitting Diode Packaging,” Int. J. Heat Mass Transf., **58**(1–2), pp. 276–281.

[46] J. Hwang et al., 2010, “Study on the Effect of the Relative Position of the Phosphor Layer in the LED Package on the High Power LED Lifetime,” Phys. Status Solidi Curr. Top. Solid State Phys., **7**(7–8), pp. 2157–2161.

[47] E. Kim et al., 2016, “Effective Heat Dissipation from Color-Converting Plates in High-Power White Light Emitting Diodes by Transparent Graphene Wrapping,” ACS Nano, **10**(1), pp. 238–245.

[48] Y. Li et al., “Review of High Power Phosphor-Converted Light-Emitting Diodes,” 2019 16th China Int. Forum Solid State Light. 2019 Int. Forum Wide Bandgap Semicond. China (SSLChina IFWS), pp. 111–115.

[49] A. Alexeev et al., 2019, “Multiple Heat Source Thermal Modeling and Transient Analysis of LEDs,” energies, **12**(10), p. 1860.

[50] Azarifar, M., Cengiz, C., and Arik, M., 2021, “Optical and Thermal Analysis of Secondary Optics in Light Emitting Diodes ’ Packaging : Analysis of Optical and Thermal Analysis of Secondary Optics in Light Emitting Diodes ’ Packaging : Analysis of MR16 Lamp,” *Journal of Physics: Conference Series*.

[51] P. Liu et al., 2022, “Development of LED Package Heat Dissipation Research,” Micromachines, **13**(2), p. 229.

[52] Liu, S., and Luo, X., 2011, *LED Packaging for Lighting Applications*.

[53] S. W. R. Lee et al., 2016, “Effect of Substrate Dimensions and Boundary Conditions on the Heat Spreading of LED Package,” *2016 International Conference on Electronics Packaging (ICEP)*, IEEE, pp. 52–56.

[54] “XLamp® XT-E LEDs.” cree-led.com. https://cree-led.com/media/documents/XLampXTE.pdf (accessed April 2, 2022).

[55] B. Ren et al., 2020, “Layered Boron Nitride Enabling High-Performance AlGaN/GaN High Electron Mobility Transistor,” J. Alloys Compd., **829**, p. 154542.

[56] J. C. Gerbedoen et al., 2009, “AlGaN/GaN MISHEMT with HBN as Gate Dielectric,” Diam. Relat. Mater., **18**(5–8), pp. 1039–1042.

[57] T. Nguyen et al., 2013, “Fabrication and Characterization of BN/AlGaN/GaN Metal-insulator-semiconductor Heterojunction Field-effect Transistors with Sputtering-deposited BN Gate Dielectric,” Phys. status solidi, **10**(11), pp. 1401–1404.

[58] Muzychka, Y. S., Culham, J. R., and Yovanovich, M. M., 2003, “Thermal Spreading Resistance of Eccentric Heat Sources on Rectangular Flux Channels,” J. Electron. Packag., **125**(2), pp. 178–185.

[59] Azarifar, M., and Donmezer, N., 2017, “A Multiscale Analytical Correction Technique for Two-Dimensional Thermal Models of AlGaN/GaN HEMTs,” Microelectron. Reliab., **74**, pp. 82–87.

[60] Z. Cheng et al., 2022, “Perspective on Thermal Conductance across Heterogeneously Integrated Interfaces for Wide and Ultrawide Bandgap Electronics,” Appl. Phys. Lett., **120**(3), p. 30501.

[61] X. Luo et al., 2016, “Heat and Fluid Flow in High-Power LED Packaging and Applications,” Prog. Energy Combust. Sci., **56**, pp. 1–32.

[62] M. H. Chang et al., 2012, “Light Emitting Diodes Reliability Review,” Microelectron. Reliab., **52**(5), pp. 762–782.

[63] Rahman, F., George, A. F., and Drinkard, R., 2015, “Short-and Long-Term Reliability Studies of Broadband Phosphor-Converted Red, Green, and White Light-Emitting Diodes,” IEEE Trans. Device Mater. Reliab., **16**(1), pp. 1–8.

[64] Z. Chen et al., 2011, “Reliability Test and Failure Analysis of High Power LED Packages,” J. Semicond., **32**(1), p. 14007.

[65] R. H. Horng et al., 2012, “Failure Modes and Effects Analysis for High-Power GaN-Based Light-Emitting Diodes Package Technology,” Microelectron. Reliab., **52**(5), pp. 818–821.

[66] Van Driel, W. D., Fan, X. J., and Zhang, G. Q., 2017, *Solid State Lighting Reliability Part 2*, Springer.

[67] S. C. Yang et al., 2010, “Failure and Degradation Mechanisms of High-Power White Light Emitting Diodes,” Microelectron. Reliab., **50**(7), pp. 959–964.

[68] N. Narendran et al., 2004, “Solid-State Lighting: Failure Analysis of White LEDs,” J. Cryst. Growth, **268**(3), pp. 449–456.

[69] Weng, C.-J., 2009, “Advanced Thermal Enhancement and Management of LED Packages,” Int. Commun. Heat Mass Transf., **36**(3), pp. 245–248.

[70] Pust, P., Schmidt, P. J., and Schnick, W., 2015, “A Revolution in Lighting,” Nat. Mater., **14**(5), pp. 454–458.

[71] Rahman, T., Raza, S., Saeed, M., and Jameel, S., 2019, “An Emerging White LED Technology and Associated Thermal Issues – A Review,” J. Appl. Emerg. Sci., **09**(02), pp. 106–120.

[72] Xia, Z., and Liu, Q., 2016, “Progress in Discovery and Structural Design of Color Conversion Phosphors for LEDs,” Prog. Mater. Sci., **84**, pp. 59–117.

[73] R. Mueller-Mach et al., 2002, "High-Power Phosphor-Converted Light-Emitting Diodes Based on III-Nitrides," IEEE J. Sel. Top. Quantum Electron., **8**(2), pp. 339–345.

[74] J. K. Kim et al., 2005, "Strongly Enhanced Phosphor Efficiency in GaInN White Light-Emitting Diodes Using Remote Phosphor Configuration and Diffuse Reflector Cup," Jpn. J. Appl. Phys., **44**(21), pp. 649–651.

[75] H. Rao et al., 2013, "An Improved Slurry Method of Self-Adaptive Phosphor Coating for White Pc-LED Packaging," IEEE/OSA J. Disp. Technol., **9**(6), pp. 453–458.

[76] C. Sommer et al., 2010, "A Comprehensive Study on the Parameters Effecting Color Conversion in Phosphor Converted White Light Emitting Diodes," *Proc. SPIE 7784, Tenth International Conference on Solid State Lighting*, San Diego, California.

[77] Arik, M., and Hsing, M., 2003, "Effects of Localized Heat Generations Due To the Color Conversion In," *ASME International Electronic Packaging Technical Conference and Exhibition*, Maui, Hawaii, pp. 1–9.

[78] X. Luo et al., 2013, "Phosphor Self-Heating in Phosphor Converted Light Emitting Diode Packaging," Int. J. Heat Mass Transf., **58**(1), pp. 276–281.

[79] J. Qiao et al., 2019, "Recent Advances in Solid-State LED Phosphors with Thermally Stable Luminescence," J. Rare Earths, **37**(6), pp. 565–572.

[80] B. Yan et al., 2013, "Influence of Phosphor Configuration on Thermal Performance of High Power White LED Array," *International Symposium on Advanced Packaging Materials*, IEEE, pp. 274–289.

[81] M. Arik et al., 2004, "Thermal Management of LEDs: Package to System," *Third International Conference on Solid State Lighting*, SPIE, pp. 64–75.

[82] Hu, R., Ã, X. L., and Zheng, H., 2012, "Hotspot Location Shift in the High-Power Phosphor-Converted White Light-Emitting Diode Packages Hotspot Location Shift in the High-Power Phosphor-Converted White Light-Emitting Diode Packages," Jpn. J. Appl. Phys., **51**.

[83] J. Nicolics et al., 2018, "Analysis of the Local Temperature Distribution in Color Conversion Elements of Phosphor Converted Light-Emitting Diodes," Int. J. Heat Mass Transf., **116**, pp. 1096–1107.

[84] Ma, Y., and Luo, X., 2019, "Two-Dimensional Axisymmetric Opto-Thermal Phosphor Modeling Based on Fluorescent Radiative Transfer Equation," J. Lumin., **214**, p. 116589.

[85] Varshni, Y. P., 1967, "Temperature Dependence of the Energy Gap in Semiconductors," Physica, **34**(1), pp. 149–154.

[86] Ashdown, I., and Salsbury, M., 2007, "Peak Wavelength Shifts and Opponent Color Theory," Seventh Int. Conf. Solid State Light., **6669**, p. 66690C.

[87] Y. Xi et al., 2005, "Junction and Carrier Temperature Measurements in Deep-Ultraviolet Light-Emitting Diodes Using Three Different Methods," Appl. Phys. Lett., **86**(3), pp. 1–3.

[88] Arik, M., Royce, C., and Kulkarni, K. S., 2014, "Developing a Standard Measurement and Calculation Procedure for High Brightness LED Junction Temperature," (1).

[89] Y. Xi et al., 2005, "Junction Temperature in Ultraviolet Light-Emitting Diodes,"

Japanese J. Appl. Physics, Part 1 Regul. Pap. Short Notes Rev. Pap., **44**(10), pp. 7260–7266.

[90] Hong, E., and Narendran, N., 2004, “A Method for Projecting Useful Life of LED Lighting Systems,” Third Int. Conf. Solid State Light., **5187**, p. 93.

[91] Wu, H. H., Lin, K. H., and Lin, S. T., 2012, “A Study on the Heat Dissipation of High Power Multi-Chip COB LEDs,” Microelectronics J., **43**(4), pp. 280–287.

[92] Shin, M. W., and Jang, S. H., 2012, “Thermal Analysis of High Power LED Packages under the Alternating Current Operation,” Solid. State. Electron., **68**, pp. 48–50.

[93] Jayawardena, A., Liu, Y. W., and Narendran, N., 2013, “Analysis of Three Different Junction Temperature Estimation Methods for AC LEDs,” Solid. State. Electron., **86**, pp. 11–16.

[94] David, A., Young, N. G., Lund, C., and Craven, M. D., 2019, “Review—The Physics of Recombinations in III-Nitride Emitters,” ECS J. Solid State Sci. Technol., **9**(1), p. 16021.

[95] Y. Lin et al., 2012, “Study of Temperature Sensitive Optical Parameters and Junction Temperature Determination of Light-Emitting Diodes,” Appl. Phys. Lett., **100**(202108).

[96] T. Wang et al., 1998, “Photoluminescence Investigation of InGaN/GaN Single Quantum Well and Multiple Quantum Wells,” Appl. Phys. Lett., **73**(24), pp. 3571–3573.

[97] Wang, Y., Pan, M., and Li, T., 2014, “Comprehensive Study of Internal Quantum Efficiency of High-Brightness GaN-Based Light-Emitting Diodes by Temperature-Dependent Electroluminescence Method,” Light. Diodes Mater. Devices, Appl. Solid State Light. XVIII, **9003**, p. 90030D.

[98] R. Hao et al., 2021, “Effects of Growth Temperature Change in Quantum Well on Luminescence Performance and Optical Spectrum,” Optik (Stuttg)., **235**(January), p. 166606.

[99] J. Li et al., 2021, “Carrier Dynamics in InGaN/GaN-Based Green LED under Different Excitation Sources,” Crystals, **11**(9).

[100] T. Takeuchi et al., 1997, “Quantum-Confined Stark Effect Due to Piezoelectric Fields in GaInN Strained Quantum Wells,” Jpn. J. Appl. Phys., **36**(Part 2, No. 4A), pp. L382–L385.

[101] J. Kim et al., 2019, “Effects of Carrier Leakage on Photoluminescence Properties of GaN-Based Light-Emitting Diodes at Room Temperature,” Curr. Opt. Photonics, **3**(2), pp. 164–171.

[102] N. C. Chen et al., 2009, “Spectral Shape and Broadening of Emission from AlGaInP Light-Emitting Diodes Spectral Shape and Broadening of Emission from AlGaInP Light-Emitting,” J. Appl. Phys., **106**(074514).

[103] Bernie Siegal, 2006, “Practical Considerations in High Power LED Junction Temperature Measurements,” p. 32.

[104] S. Chhajed et al., 2005, “Influence of Junction Temperature on Chromaticity and Color-Rendering Properties of Trichromatic White-Light Sources Based on Light-Emitting Diodes,” J. Appl. Phys., **97**(5).

[105] S. Chhajed et al., 2005, “Junction Temperature in Light-Emitting Diodes Assessed by

Different Methods," Light. Diodes Res. Manuf. Appl. IX, **5739**, p. 16.

[106] Chen, K., and Narendran, N., 2013, "Estimating the Average Junction Temperature of AlGaInP LED Arrays by Spectral Analysis," Microelectron. Reliab., **53**(5), pp. 701–705.

[107] Tamura, T., Setomoto, T., and Taguchi, T., 2000, "Illumination Characteristics of Lighting Array Using 10 Candela-Class White LEDs under AC 100 V Operation," J. Lumin., **87**, pp. 1180–1182.

[108] Chen, H., Tan, S., and Hui, S. Y., 2014, "Color Variation Reduction of GaN-Based White Light-Emitting Diodes Via Peak-Wavelength Stabilization," IEEE Trans. Power Electron., **29**(7), pp. 3709–3719.

[109] Gu, Y., and Narendran, N., 2004, "A Noncontact Method for Determining Junction Temperature of Phosphor-Converted White LEDs," Third Int. Conf. Solid State Light., **5187**, p. 107.

[110] T. Yang et al., 2018, "Noncontact and Instant Detection of Phosphor Temperature in Phosphor-Converted White LEDs," Sci. Rep., **8**(1).

[111] J. Jin et al., 2019, "A Microscopic Hyperspectral-Based Centroid Wavelength Method for Measuring Two-Dimensional Junction Temperature Distribution of LEDs," IEEE Electron Device Lett., **40**(4), pp. 506–509.

[112] Y. Feng et al., 2021, "Thermal Characteristics of InGaN-Based Green Micro-LEDs," AIP Adv., **11**(4).

[113] D. Priante et al., 2018, "Diode Junction Temperature in Ultraviolet AlGaN Quantum-Disks-in-Nanowires," J. Appl. Phys., **124**(1), p. 15702.

[114] Kölzer, J., Oesterschulze, E., and Deboy, G., 1996, "Thermal Imaging and Measurement Techniques for Electronic Materials and Devices," Microelectron. Eng., **31**(1), pp. 251–270.

[115] Cengiz, C., Azarifar, M., and Arık, M., 2021, "Thermal and Optical Characterization of White and Blue Multi-Chip LED Light Engines," *InterSociety Conference on Thermal and Thermomechanical Phenomena in Electronic Systems, ITHERM*, IEEE, pp. 285–293.

[116] J. Christofferson et al., 2008, "Microscale and Nanoscale Thermal Characterization Techniques," J. Electron. Packag., **130**(4).

[117] J. Altet et al., 2006, "Dynamic Surface Temperature Measurements in ICs," Proc. IEEE, **94**(8), pp. 1519–1533.

[118] Cutolo, A., 1998, "Selected Contactless Optoelectronic Measurements for Electronic Applications," Rev. Sci. Instrum., **69**(2), pp. 337–360.

[119] Tessier, G., Hole, S., and Fournier, D., 2001, "Quantitative Thermal Imaging by Synchronous Thermoreflectance with Optimized Illumination Wavelengths," Appl. Phys. Lett., **78**(16), pp. 2267–2269.

[120] Dilhaire, S., Grauby, S., and Claeys, W., 2004, "Calibration Procedure for Temperature Measurements by Thermoreflectance under High Magnification Conditions," Appl. Phys. Lett., **84**(5), pp. 822–824.

[121] L. R. De Freitas et al., 2005, "Sensitivity Enhancement in Thermoreflectance Microscopy of Semiconductor Devices Using Suitable Probe Wavelengths," J. Appl.

Phys., **98**(6), p. 63508.

[122] Vollmer, M., and Möllmann, K. P., 2017, *Infrared Thermal Imaging: Fundamentals, Research and Applications,* John Wiley & Sons.

[123] Corfa, A., Gasse, A., Bernabé, S., and Ribot, H., 2010, “Analytical and FEM Simulations of the Thermal Spreading Effect in LED Modules and IR Thermography Validation,” 11th Int. Conf. Therm. Mech. Multi-Physics Simulation, Exp. Microelectron. Microsystems, EuroSimE 2010.

[124] Jang, H., Lee, J. H., Byon, C., and Lee, B. J., 2018, “Innovative Analytic and Experimental Methods for Thermal Management of SMD-Type LED Chips,” Int. J. Heat Mass Transf., **124**, pp. 36–45.

[125] Z. Z. Chen et al., 2007, “Junction Temperature and Reliability of High-Power Flip-Chip Light Emitting Diodes,” Mater. Sci. Semicond. Process., **10**(4–5), pp. 206–210.

[126] K. S. Chang et al., 2012, “Precise Temperature Mapping of GaN-Based LEDs by Quantitative Infrared Micro-Thermography,” Sensors, **12**(4), pp. 4648–4660.

[127] Mashkov, P., Pencheva, T., and Gyoch, B., 2010, “LEDs’ Thermal Management Aided by Infrared Thermography,” 2010 Int. Symp. Adv. Packag. Mater. Microtech, APM ’10, (3), pp. 68–73.

[128] M. Tao et al., 2012, “Effect of Die Attach Adhesive Defects on the Junction Temperature Uniformity of LED Chips,” Proc. IEEE/CPMT Int. Electron. Manuf. Technol. Symp.

[129] Andonova, A., Kim, N., and Vakrilov, N., 2016, “Estimation the Amount of Heat Generated by LEDs under Different Operating Conditions,” Elektron. ir Elektrotechnika, **22**(2), pp. 49–53.

[130] D. Lee et al., 2018, “A Study on the Measurement and Prediction of LED Junction Temperature,” Int. J. Heat Mass Transf., **127**, pp. 1243–1252.

[131] Yung, K. C., Liem, H., and Choy, H. S., 2013, “Heat Dissipation Performance of a High-Brightness LED Package Assembly Using High-Thermal Conductivity Filler,” Appl. Opt., **52**(35), pp. 8484–8493.

[132] M. Kim et al., 2015, “Microscale Thermometry: A Review,” Microelectron. Eng., **148**, pp. 129–142.

[133] P. R. N. Childs et al., 2000, “Review of Temperature Measurement,” Rev. Sci. Instrum., **2959**.

[134] Cheng, H. C., Lin, J. Y., and Chen, W. H., 2012, “On the Thermal Characterization of an RGB LED-Based White Light Module,” Appl. Therm. Eng., **38**, pp. 105–116.

[135] Ozluk, B., Muslu, A. M., and Arik, M., 2019, “A Comparative Study for the Junction Temperature of Green Light-Emitting Diodes,” IEEE Trans. Components, Packag. Manuf. Technol., **9**(10), pp. 2024–2035.

[136] A. E. Chernyakov et al., 2013, “Experimental and Theoretical Study of Electrical, Thermal, and Optical Characteristics of InGaN/GaN High-power Flip-chip LEDs,” Phys. status solidi, **210**(3), pp. 466–469.

[137] Aladov, A., Chernyakov, A., and Zakgeim, A., 2019, “Infrared Micro-Thermography of High-Power AlInGaN LEDs Using High Emissivity (Black) in IR and Transparent in the

Visible Spectral Region Coating," Quant. Infrared Thermogr. J., **16**(2), pp. 172–180.

[138] Katra, I., Blumberg, D. G., Lavee, H., and Sarah, P., 2007, "Topsoil Moisture Patterns on Arid Hillsides – Micro-Scale Mapping by Thermal Infrared Images," J. Hydrol., **334**(3), pp. 359–367.

[139] C. H. Oxley et al., 2011, "Probe Propels IR Thermal Microscopy to a New Level."

[140] Webb, P. W., 1991, "Thermal Imaging of Electronic Devices with Low Surface Emissivity," IEE Proc. G (Circuits, Devices Syst., **138**(3), pp. 390–400.

[141] Watson, K., 1992, "Two-Temperature Method for Measuring Emissivity," Remote Sens. Environ., **42**(2), pp. 117–121.

[142] K. Hollstein et al., 2022, "Developing a Micro-Thermography System for Thermal Characterization of LED Packages," Microelectron. Eng., **254**, p. 111694.

[143] M. Vellvehi et al., 2011, "Irradiance-Based Emissivity Correction in Infrared Thermography for Electronic Applications," Rev. Sci. Instrum., **82**(11), p. 114901.

[144] Brandt, R., Bird, C., and Neuer, G., 2008, "Emissivity Reference Paints for High Temperature Applications," Measurement, **41**(7), pp. 731–736.

[145] R. H. Hopper et al., 2010, "Use of Carbon Micro-Particles for Improved Infrared Temperature Measurement of CMOS MEMS Devices," Meas. Sci. Technol., **21**(4), p. 45107.

[146] A. Sarua et al., 2006, "Integrated Micro-Raman/Infrared Thermography Probe for Monitoring of Self-Heating in AlGaN/GaN Transistor Structures," IEEE Trans. Electron Devices, **53**(10), pp. 2438–2447.

[147] Vollmer, M., and Möllman, K. P., 2017, *Infrared Thermal Imaging: Fundamentals, Research and Applications*.

[148] M. Welna et al., 2012, "Transparency of GaN Substrates in the Mid-infrared Spectral Range," Cryst. Res. Technol., **47**(3), pp. 347–350.

[149] C. Rongier et al., 2022, "Infrared Thermography Applied to the Validation of Thermal Simulation of High Luminance LED Used in Automotive Front Lighting," Infrared Phys. Technol., **120**, p. 103980.

[150] Muslu, A. M., Ozluk, B., and Arik, M., 2021, "An Investigation Into the Optothermal Behavior of a High Power Red Light Emitting Diode : Impact of an Optical Path," J. Electron. Packag. Trans. ASME, **143**, p. 011007.

[151] M. Farzaneh et al., 2009, "CCD-Based Thermoreflectance Microscopy: Principles and Applications," J. Phys. D. Appl. Phys., **42**(14).

[152] Ju, Y. S., and Goodson, K. E., 1997, "Thermal Mapping of Interconnects Subjected to Brief Electrical Stresses," IEEE Electron Device Lett., **18**(11), pp. 512–514.

[153] Bahk, J., and Shakouri, A., 2019, "Ultra-Fast Thermoreflectance Imaging for Electronic, Optoelectronic, and Thermal Devices," *2019 IEEE BiCMOS and Compound Semiconductor Integrated Circuits and Technology Symposium (BCICTS)*, pp. 1–7.

[154] Ju, Y. S., and Goodson, K. E., 1997, "Short-Timescale Thermal Mapping of Interconnects," *1997 IEEE International Reliability Physics Symposium Proceedings. 35th Annual*, IEEE, pp. 320–324.

[155] H. Kempkens et al., 1990, “Measurements of Electrode Temperature Evolution by Laser Light Reflection,” J. Appl. Phys., **67**(8), pp. 3618–3624.

[156] Claeys, W., Dilhaire, S., and Quintard, V., 1994, “Laser Probing of Thermal Behaviour of Electronic Components and Its Application in Quality and Reliability Testing,” Microelectron. Eng., **24**(1–4), pp. 411–420.

[157] W. Claeys et al., 1993, “Thermoreflectance Optical Test Probe for the Measurement of Current-induced Temperature Changes in Microelectronic Components,” Qual. Reliab. Eng. Int., **9**(4), pp. 303–308.

[158] Burzo, M. G., Komarov, P. L., and Raad, P. E., 2003, “Thermal Transport Properties of Gold-Covered Thin-Film Silicon Dioxide,” IEEE Trans. Components Packag. Technol., **26**(1), pp. 80–88.

[159] L. Rossi et al., 2006, “Thermal Mapping of Power Devices with a Completely Automated Thermoreflectance Measurement System,” *2006 Ph. D. Research in Microelectronics and Electronics*, IEEE, pp. 41–44.

[160] Matatagui, E., Thompson, A. G., and Cardona, M., 1968, “Thermoreflectance in Semiconductors,” Phys. Rev., **176**(3), p. 950.

[161] Summers, J. A., and Hudgings, J. A., 2009, “Confocal Thermoreflectance for Spatially Resolved Surface Thermography of Transparent LEDs,” *2009 Conference on Lasers and Electro-Optics and 2009 Conference on Quantum Electronics and Laser Science Conference*, pp. 1–2.

[162] Ling, J. H. L., and Tay, A. A. O., 2014, “Measurement of LED Junction Temperature Using Thermoreflectance Thermography,” Proc. Electron. Packag. Technol. Conf. EPTC, pp. 1482–1485.

[163] Y. Xiao et al., 2017, “Determining Junction Temperature of LEDs by the Relative Reflected Intensity of the Incident Exciting Light,” IEEE Trans. Electron Devices, **64**, pp. 2257–2260.

[164] Kendig, D., Yazawa, K., and Shakouri, A., 2011, “Thermal Imaging of Encapsulated LEDs,” *2011 27th Annual IEEE Semiconductor Thermal Measurement and Management Symposium*, pp. 310–313.

[165] G. Xiao et al., 2021, “Two-Dimensional Transient Temperature Distribution Measurement of GaN Light-Emitting Diode Using High Speed Camera,” IEEE J. Electron Devices Soc., **9**, pp. 663–666.

[166] Zheng, D. G., Shin, D. S., and Shim, J. I., 2021, “Measuring the Surface Temperature of Light-Emitting Diodes by Thermoreflectance,” Jpn. J. Appl. Phys., **60**(5).

[167] Azarifar, M., Cengiz, C., and Arik, M., 2022, “Thermal and Optical Performance Characterization of Bare and Phosphor Converted LEDs through Package Level Immersion Cooling,” Int. J. Heat Mass Transf., **189**, p. 122607.

[168] M. Kuball et al., 2003, “Measurement of Temperature Distribution in Multifinger AlGaN/GaN Heterostructure Field-Effect Transistors Using Micro-Raman Spectroscopy,” Appl. Phys. Lett., **82**(1), pp. 124–126.

[169] M. Kuball et al., 2007, “Time-Resolved Temperature Measurement of AlGaN/GaN Electronic Devices Using Micro-Raman Spectroscopy,” IEEE Electron Device Lett., **28**(2), pp. 86–89.

[170] Das, R. S., and Agrawal, Y. K., 2011, "Raman Spectroscopy: Recent Advancements, Techniques and Applications," Vib. Spectrosc., **57**(2), pp. 163–176.

[171] J. B. Cui et al., 1998, "Noncontact Temperature Measurements of Diamond by Raman Scattering Spectroscopy," J. Appl. Phys., **83**(12), pp. 7929–7933.

[172] G. Pavlidis et al., 2017, "Characterization of AlGaN/GaN HEMTs Using Gate Resistance Thermometry," IEEE Trans. Electron Devices, **64**(1), pp. 78–83.

[173] T. Batten et al., 2010, "Temperature Analysis of AlGaN/GaN Based Devices Using Photoluminescence Spectroscopy: Challenges and Comparison to Raman Thermography," J. Appl. Phys., **107**(7).

[174] A. Sarua et al., 2007, "Thermal Boundary Resistance Between GaN and Substrate in AlGaN/GaN Electronic Devices," IEEE Trans. Electron Devices, **54**(12), pp. 3152–3158.

[175] I. Calizo et al., 2007, "Temperature Dependence of the Raman Spectra of Graphene and Graphene Multilayers," Nano Lett., **7**(9), pp. 2645–2649.

[176] A. Chitnis et al., 2002, "Self-Heating Effects at High Pump Currents in Deep Ultraviolet Light-Emitting Diodes at 324 Nm," Appl. Phys. Lett., **81**(18), pp. 3491–3493.

[177] V. Schwegler et al., 1999, "Ohmic Heating of InGaN LEDs during Operation : Determination of the Junction Temperature and Its Influence on Device Performance," Phys. Status Solidi, **176**(1), pp. 783–786.

[178] M. S. Liu et al., 1999, "Temperature Dependence of Raman Scattering in Single Crystal GaN Films," Appl. Phys. Lett., **74**(21), pp. 3125–3127.

[179] E. Alarcón-Lladó et al., 2010, "Temperature Rise in InGaN/GaN Vertical Light Emitting Diode on Copper Transferred from Silicon Probed by Raman Scattering," J. Appl. Phys., **108**(11), p. 114501.

[180] H. Tsuji et al., 2008, "Temperature Measurements of Organic Light-Emitting Diodes by Stokes and Anti-Stokes Raman Scattering," Jpn. J. Appl. Phys., **47**(4R), p. 2171.

[181] J. Senawiratne et al., 2008, "Junction Temperature Measurements and Thermal Modeling of GaInN/GaN Quantum Well Light-Emitting Diodes," J. Electron. Mater., **37**(5), pp. 607–610.

[182] E. Tamdogan et al., 2018, "A Comparative Study on the Junction Temperature Measurements of LEDs with Raman Spectroscopy, Microinfrared (IR) Imaging, and Forward Voltage Methods," IEEE Trans. Components, Packag. Manuf. Technol., **8**(11), pp. 1914–1922.

[183] T. Beechem et al., 2007, "Simultaneous Mapping of Temperature and Stress in Microdevices Using Micro-Raman Spectroscopy," Rev. Sci. Instrum., **78**(6).

[184] Y. Wang et al., 2010, "In Situ Temperature Measurement of GaN-Based Ultraviolet Light-Emitting Diodes by Micro-Raman Spectroscopy," J. Electron. Mater., **39**(11), pp. 2448–2451.

[185] Ohsaka, T., 1980, "Temperature Dependence of the Raman Spectrum in Anatase Tio2," J. Phys. Soc. Japan, **48**(5), pp. 1661–1668.

[186] N. Lundt et al., 2013, "High Spatial Resolution Raman Thermometry Analysis of TiO2 Microparticles," Rev. Sci. Instrum., **84**(10).

[187] Beechem, T., and Graham, S., 2007, “Temperature Measurement of Microdevices Using Thermoreflectance and Raman Thermometry,” *BioNanoFluidic MEMS*, Springer, NewYork, pp. 153–174.

[188] Natarajan, S., Habtemichael, Y., and Graham, S., 2013, “A Comparative Study of Thermal Metrology Techniques for Ultraviolet Light Emitting Diodes,” J. Heat Transfer, **135**(9), p. 91201.

[189] M. Horiuchi et al., 2015, “Development of Junction Temperature Estimation System for Light-Emitting LED Using Pulsed-Laser Raman Scattering,” J. Solid State Light., **2**(1), p. 7.

[190] Cooper, T. E., Field, R. J., and Meyer, J. F., 1975, “Liquid Crystal Thermography and Its Application to the Study of Convective Heat Transfer,” J. Heat Transfer, **97**(3), pp. 442–450.

[191] Collings, P. J., 2002, *Liquid Crystals: Nature’s Delicate Phase of Matter*.

[192] Azar, K., Benson, J. R., and Manno, V. P., 1991, “Liquid Crystal Imaging for Temperature Measurement of Electronic Devices,” Proc. - IEEE Semicond. Therm. Temp. Meas. Symp., pp. 23–33.

[193] Farina, D. J., 1995, “Making Surface Temperature Measurements Using Liquid Crystal Thermography,” Electron. Cool., **1**(2), pp. 10–15.

[194] N. Abdullah et al., 2010, “The Basics and Issues of Thermochromic Liquid Crystal Calibrations,” Exp. Therm. Fluid Sci., **34**(8), pp. 1089–1121.

[195] Lee, C. C., and Park, J., 2004, “Temperature Measurement of Visible Light-Emitting Diodes Using Nematic Liquid Crystal Thermography With Laser Illumination,” IEEE Photonics Technol. Lett., **16**(7), pp. 1706–1708.

[196] W. J. Hwang et al., 2004, “Determination of Junction Temperature and Thermal Resistance in the GaN-Based LEDs Using Direct Temperature Measurement,” Phys. Status Solidi, **1**(10), pp. 2429–2432.

[197] Blackburn, D. L., 2004, “Temperature Measurements of Semiconductor Devices - a Review,” *Twentieth Annual IEEE Semiconductor Thermal Measurement and Management Symposium (IEEE Cat. No.04CH37545)*, pp. 70–80.

[198] Muslu, A. M., and Arik, M., 2019, “Impact of Electronics over Localized Hot Spots in Multi-Chip White LED Light Engines,” Intersoc. Conf. Therm. Thermomechanical Phenom. Electron. Syst. ITHERM, **2019-May**, pp. 31–39.

[199] H. L. Ke et al., 2016, “Junction Temperature Estimation for LED Lamp with Forward Voltage Method,” 2016 17th Int. Conf. Therm. Mech. Multi-Physics Simul. Exp. Microelectron. Microsystems, EuroSimE 2016, **1**(3888), pp. 2–5.

[200] Roscam Abbing, F. D., and Pertijs, M. A. P., 2011, “Light-Emitting Diode Junction-Temperature Sensing Using Differential Voltage/Current Measurements,” Proc. IEEE Sensors, pp. 861–864.

[201] Muslu, A. M., Ozluk, B., and Arik, M., 2017, “Impact of Junction Temperature Over Forward Voltage Drop for Red, Blue and Green High Power Light Emitting Diode Chips,” *16th Intersociety Conference on Thermal and Thermomechanical Phenomena in Electronic Systems*, IEEE, Orlando, FL.

[202] D. Iero et al., 2021, “A Technique for Improving the Precision of the Direct

Measurement of Junction Temperature in Power Light-Emitting Diodes," Sensors, **21**(9).

[203] P. Perlin et al., 1996, "Low-temperature Study of Current and Electroluminescence in InGaN/AlGaN/GaN Double-heterostructure Blue Light-emitting Diodes," Appl. Phys. Lett., **69**(12), pp. 1680–1682.

[204] A. Keppens et al., 2008, "High Power Light-Emitting Diode Junction Temperature Determination from Current-Voltage Characteristics," J. Appl. Phys., **104**(9).

[205] Xi, Y., and Schub, 2004, "Junction-Temperature Measurement In GaN UV Light-Emitting Diodes Using The Diode Forward Voltage," Int. J. High Speed Electron. Syst., **14**(3), pp. 708–713.

[206] F. Jiang et al., 2007, "Research on the Junction-Temperature Characteristic of GaN Light-Emitting Diodes on Si Substrate," J. Lumin., **122–123**, pp. 693–695.

[207] D. Meyaard et al., 2013, "Analysis of the Temperature Dependence of the Forward Voltage Characteristics of GaInN Light-Emitting Diodes," Appl. Phys. Lett., **103**(12), p. 121103.

[208] Onwukaeme, C., Choi, W. J., and Ryu, H. Y., 2021, "Accurate Determination of Junction Temperature in a GaN-Based Blue Light-Emitting Diode Using Nonlinear Voltage-Temperature Relation."

[209] Hantos, G., Hegedüs, J., and Poppe, A., 2018, "Different Questions of Today's LED Thermal Testing Procedures," *2018 34th Thermal Measurement, Modeling & Management Symposium (SEMI-THERM)*, pp. 63–70.

[210] Kim, D. S., and Han, B., 2016, "Effect of Junction Temperature on Heat Dissipation of High Power Light Emitting Diodes," J. Appl. Phys., **119**(12), p. 125104.

[211] M. Meneghini et al., 2020, "Thermal Droop in III-Nitride Based Light-Emitting Diodes: Physical Origin and Perspectives," J. Appl. Phys., **127**(21).

[212] D. P. Han et al., 2020, "Identifying the Cause of Thermal Droop in GaInN-Based LEDs by Carrier- and Thermo-Dynamics Analysis," Sci. Rep., **10**(1), p. 17433.

[213] I. E. Titkov et al., 2014, "Temperature-Dependent Internal Quantum Efficiency of Blue High-Brightness Light-Emitting Diodes," IEEE J. Quantum Electron., **50**(11), pp. 911–920.

[214] L. Zhao et al., 2018, "Temperature-Dependent Efficiency Droop in GaN-Based Blue LEDs," IEEE Electron Device Lett., **39**(4), pp. 528–531.

[215] Lee, H. K., Yu, J. S., and Lee, Y. T., 2010, "Thermal Analysis and Characterization of the Effect of Substrate Thinning on the Peformances of GaN-based Light Emitting Diodes," Phys. status solidi, **207**(6), pp. 1497–1504.

[216] Oh, S. J., and Cho, J., 2017, "Junction Temperature Rise Due to Self-Heating Effects in GaInN Blue Light-Emitting Diodes," Thin Solid Films, **641**, pp. 8–11.

[217] "T3Ster Thermal Transient Tester, Technical Information, Mentor Graphics." flotrend.com.tw. https://www.flotrend.com.tw/files/f-pid/t3ster/2013/T3Ster_b.pdf (accessed April 15, 2022).

[218] Standard, J., "Implementation of the Electrical Test Method for the Measurement of Real Thermal Resistance and Impedance of Light-Emitting Diodes with Exposed Cooling," JESD51-51.

[219] Association, E. I., 1995, “Integrated Circuit Thermal Measurement Method–Electrical Test Method,” EIA/JEDEC Stand. JESD51-1.

[220] JESD51, J. S., 2010, “Transient Dual Interface Test Method for the Measurement of the Thermal Resistance Junction-To-Case of Semiconductor Devices with Heat Flow through a Single Path,” JEDEC Solid State Technol. Assoc.

[221] K. S. Yang et al., 2013, “An Experimental Study on the Heat Dissipation of LED Lighting Module Using Metal/Carbon Foam,” Int. Commun. Heat Mass Transf., **48**, pp. 73–79.

[222] K. S. Yang et al., 2015, “A Novel Flat Polymer Heat Pipe with Thermal via for Cooling Electronic Devices,” Energy Convers. Manag., **100**, pp. 37–44.

[223] Liu, D., Yang, H., and Yang, P., 2014, “Experimental and Numerical Approach on Junction Temperature of High-Power LED,” Microelectron. Reliab., **54**(5), pp. 926–931.

[224] Yang, L., Wei, B., and Zhang, J., 2012, “Transient Thermal Characterization of Organic Light-Emitting Diodes,” Semicond. Sci. Technol., **27**(10), p. 105011.

[225] K. Keränen et al., 2015, “Roll-to-Roll Printed and Assembled Large Area LED Lighting Element,” Int. J. Adv. Manuf. Technol., **81**(1), pp. 529–536.

[226] M. E. Raypah et al., 2016, “Estimation of Luminous Flux and Luminous Efficacy of Low-Power SMD LED as a Function of Injection Current and Ambient Temperature,” IEEE Trans. Electron Devices, **63**(7), pp. 2790–2795.

[227] Poppe, A., Molnár, G., and Temesvölgyi, T., 2010, “Temperature Dependent Thermal Resistance in Power LED Assemblies and a Way to Cope with It,” *2010 26th Annual IEEE Semiconductor Thermal Measurement and Management Symposium (SEMI-THERM)*, pp. 283–288.

[228] B. Shieh et al., 2019, “Empirical Modeling and Measurement of the Pulsed Junction Temperature of VCSEL,” *2019 20th International Conference on Electronic Packaging Technology(ICEPT)*, pp. 1–4.

[229] G. Martin et al., 2016, “Delphi4LED-from Measurements to Standardized Multi-Domain Compact Models of Light Emitting Diodes (LED),” Electron. Cool., **22**(12), pp. 20–23.

[230] H. Choi et al., 2021, “Precise Measurement of Junction Temperature by Thermal Analysis of Light-Emitting Diode Operated at High Environmental Temperature,” Microelectron. Eng., **235**, p. 111451.

[231] Y. Liu et al., 2010, “Estimating the Junction Temperature of AC LEDs,” *Tenth International Conference on Solid State Lighting*, International Society for Optics and Photonics, p. 778409.

[232] H. Zhu et al., 2017, “A Bipolar-Pulse Voltage Method for Junction Temperature Measurement of Alternating Current Light-Emitting Diodes,” IEEE Trans. Electron Devices, **64**(5), pp. 2326–2329.

[233] Yao, R., Zhang, D., Zou, B., and Xu, J., 2016, “Junction Temperature Measurement of Alternating Current Light-Emitting-Diode by Threshold Voltage Method,” Front. Optoelectron., **9**(4), pp. 555–559.

[234] S. Lin et al., 2013, “Determining Junction Temperature in InGaN Light-Emitting Diodes Using Low Forward Currents,” IEEE Trans. Electron Devices, **60**(11), pp. 3775–3779.

[235] B. Wu et al., 2013, “Junction-Temperature Determination in InGaN Light-Emitting Diodes Using Reverse Current Method,” IEEE Trans. Electron Devices, **60**(1), pp. 241–245.

[236] Pollock, D. D., 1991, *Thermocouples: Theory and Properties*, CRC Press.

[237] “Solder-Point Temperature Measurement of Cree XLamp LEDs. ” cree.com. https://cree-led.com/media/documents/Solder_Point_Temp.pdf (accessed April 20, 2022)

[238] “Temperature Measurement with Thermocouples.” osram.com. https://dammedia.osram.info/media/resource/hires/osram-dam 3822798/The%20thermal%20measurement%20point%20of%20LEDs.pdf (accessed April 20, 2022)

[239] Jung, E. D., and Lee, Y. L., 2015, “Development of a Heat Dissipating LED Headlamp with Silicone Lens to Replace Halogen Bulbs in Used Cars,” Appl. Therm. Eng., **86**, pp. 143–150.

[240] Song, B. M., Han, B., and Lee, J. H., 2013, “Optimum Design Domain of LED-Based Solid State Lighting Considering Cost, Energy Consumption and Reliability,” Microelectron. Reliab., **53**(3), pp. 435–442.

[241] R. Faranda et al., 2012, “Refrigerating Liquid Prototype for LED’s Thermal Management,” Appl. Therm. Eng., **48**, pp. 155–163.

[242] A., R., C., R. K., and V.P., C., 2021, “Experimental Analysis on Estimating Junction Temperature and Service Life of High Power LED Array,” Microelectron. Reliab., **120**(May 2020), p. 114121.

[243] S. Sadat, S et al., 2010, “Nanoscale Thermometry Using Point Contact Thermocouples,” Nano Lett., **10**(7), pp. 2613–2617.

[244] Lee, J., and Kotov, N. A., 2007, “Thermometer Design at the Nanoscale,” Nano Today, **2**(1), pp. 48–51.

[245] D. Chu et al., 2003, “Transient Temperature Measurements of Resist Heating Using Nanothermocouples,” J. Vac. Sci. Technol. B Microelectron. Nanom. Struct. Process. Meas. Phenom., **21**(6), pp. 2985–2989.

[246] Shih, F., Tsou, C., and Fang, W., 2021, “A Monolithic Micromachined Thermocouple Probe With Electroplating Nickel for Micro-LED Inspection,” J. Microelectromechanical Syst.

[247] H. Choi et al., 2019, “Integrated Microsensor for Precise, Real-Time Measurement of Junction Temperature of Surface-Mounted Light-Emitting Diode,” Sensors Actuators A Phys., **298**, p. 111578.

[248] Fu, X., and Luo, X., 2013, “Can Thermocouple Measure Surface Temperature of Light Emitting Diode Module Accurately?,” Int. J. Heat Mass Transf., **65**, pp. 199–202.

[249] J. Zhong et al., 2013, “Magnetic Nanoparticle Temperature Estimation Using AC Magnetic Filed,” *2013 International Workshop on Magnetic Particle Imaging (IWMPI)*, p. 1.

[250] Weaver, J. B., Rauwerdink, A. M., and Hansen, E. W., 2009, “Magnetic Nanoparticle Temperature Estimation,” Med. Phys., **36**(5), pp. 1822–1829.

[251] J. Zhong et al., 2012, “A Noninvasive, Remote and Precise Method for Temperature and Concentration Estimation Using Magnetic Nanoparticles,” Nanotechnology, **23**(7), p. 75703.

[252] Xu, W., Liu, W., and Zhang, P., 2016, “Nanosecond-Resolved Temperature Measurements Using Magnetic Nanoparticles,” Rev. Sci. Instrum., **87**(5), p. 54902.

[253] J. Zhong et al., 2014, “A New Approach for Highly Accurate, Remote Temperature Probing Using Magnetic Nanoparticles,” Sci. Rep., **4**(1), p. 6338.

[254] R. Hu et al., 2015, “Noninvasively Probing the Light-Emitting Diode Temperature by Magnetic Nanoparticles,” J. Appl. Phys., **118**(12), p. 124501.

[255] “Illumia Plus 600/610.” labsphere.com. https://www.labsphere.com/labsphere-products-solutions/light-metrology/illumia-plus-systems/illumia-plus-600-610/ (accessed April 20, 2022)

[256] F. P. Incropera et al., 1996, *Fundamentals of Heat and Mass Transfer*, Wiley New York.

[257] Harima, H., 2002, “Properties of GaN and Related Compounds Studied by Means of Raman Scattering,” J. Phys. Condens. Matter, **14**(38), p. R967.

[258] D. S. Meyaard et al., 2011, “On the Temperature Dependence of Electron Leakage from the Active Region of GaInN/GaN Light-Emitting Diodes,” Appl. Phys. Lett., **99**(4), p. 41112.

[259] Bulashevich, K. A., Ramm, M. S., and Karpov, S. Y., 2009, “Assessment of Various LED Structure Designs for High-current Operation,” Phys. status solidi c, **6**(S2), pp. S804–S806.

[260] Kahvecioglu, H. I., Tamdogan, E., and Arik, M., 2018, “Investigation of Combined Optical and Thermal Effects on Phosphor Converted Light-Emitting Diodes with Liquid Immersion Cooling,” Opt. Eng., **57**(05).

[261] “S-7200.” avantorsciences.com. https://www.avantorsciences.com/assetsvc/asset/en_US/id/29020202/contents (accessed April 20, 2022)

[262] J. Vatteville et al., 2009, “Starting Laminar Plumes: Comparison of Laboratory and Numerical Modeling,” Geochemistry, Geophys. Geosystems, **10**(12).

[263] “Phosphor Information Leaflet.” fh-muenster.de. https://www.fh-muenster.de/ciw/downloads/personal/juestel/juestel/pisa_vis/Phosphor_Information_Leaflet_L-G1-04-Ce_Y3Al5O12-Ce_.pdf (accessed April 20, 2022)

[264] F. M. Muñoz-Pérez et al., 2020, “Steady-State 3D Trapping and Manipulation of Microbubbles Using Thermocapillary,” Front. Phys., p. 467.

[265] K. Gupta et al., 2020, “Laser-Driven Marangoni Flow and Vortex Formation in a Liquid Droplet,” Phys. Fluids, **32**(12), p. 121701.

[266] Ashkin, A., 1970, “Atomic-Beam Deflection by Resonance-Radiation Pressure,” Phys. Rev. Lett., **25**(19), p. 1321.

[267] Kumar, G. R., 2018, “The 2018 Nobel Prize in Physics,” Curr. Sci., **115**(10), pp. 1844–1848.

[268] Malai, N. V, 2006, “Effect of Motion of the Medium on the Photophoresis of Hot

Hydrosol Particles," Fluid Dyn., **41**(6), pp. 984–991.

[269] Y. Zhang et al., 2019, "Optical Attraction of Strongly Absorbing Particles in Liquids," Opt. Express, **27**(9), pp. 12414–12423.

[270] Arik, M., Utturkar, Y., and Weaver, S., 2010, "Immersion Cooling of Light Emitting Diodes," *12th IEEE Intersociety Conference on Thermal and Thermomechanical Phenomena in Electronic Systems*, IEEE, Las Vegas.

[271] Tamdogan, E., and Arik, M., 2015, "Natural Convection Immersion Cooling with Enhanced Optical Performance of Light-Emitting Diode Systems," J. Electron. Packag. Trans. ASME, **137**(4), p. 041006.

[272] Effendi, N. S., and Kim, K. J., 2017, "Orientation Effects on Natural Convective Performance of Hybrid Fin Heat Sinks," Appl. Therm. Eng., **123**, pp. 527–536.

[273] Garoosi, F., Shakibaeinia, A., and Bagheri, G., 2015, "Eulerian–Lagrangian Modeling of Solid Particle Behavior in a Square Cavity with Several Pairs of Heaters and Coolers Inside," Powder Technol., **280**, pp. 239–255.

[274] Bhattad, A., Sarkar, J., and Ghosh, P., 2018, "Discrete Phase Numerical Model and Experimental Study of Hybrid Nanofluid Heat Transfer and Pressure Drop in Plate Heat Exchanger," Int. Commun. Heat Mass Transf., **91**, pp. 262–273.

[275] Chiacchio, F., Manca, O., and Nardini, S., 2007, "Numerical Investigation of Forced Convection of Nanofluids in Circular Tubes," *Heat Transfer Summer Conference*, pp. 839–848.

[276] Eslamian, M., and Saghir, M. Z., 2013, "Novel Thermophoretic Particle Separators: Numerical Analysis and Simulation," Appl. Therm. Eng., **59**(1), pp. 527–534.

[277] Kharoua, N., AlShehhi, M., and Khezzar, L., 2015, "Prediction of Black Powder Distribution in Junctions Using the Discrete Phase Model," Powder Technol., **286**, pp. 202–211.

[278] Xu, A., Tao, S., Shi, L., and Xi, H.-D., 2020, "Transport and Deposition of Dilute Microparticles in Turbulent Thermal Convection," Phys. Fluids, **32**(8), p. 83301.

[279] de Vicente, J., and Ramírez, J., 2007, "Effect of Friction between Particles in the Dynamic Response of Model Magnetic Structures," J. Colloid Interface Sci., **316**(2), pp. 867–876.

[280] K. Nandy et al., 2008, "Analytical Model for the Magnetophoretic Capture of Magnetic Microspheres in Microfluidic Devices," J. Magn. Magn. Mater., **320**(7), pp. 1398–1405.

[281] T. Sera et al., 2015, "Numerical Simulation of Airflow and Microparticle Deposition in a Synchrotron Micro-CT-Based Pulmonary Acinus Model," Comput. Methods Biomech. Biomed. Engin., **18**(13), pp. 1427–1435.

[282] Davis, R. H., 1992, "Modeling of Fouling of Crossflow Microfiltration Membranes," Sep. Purif. methods, **21**(2), pp. 75–126.

[283] Morsi, S. A., and Alexander, A. J., 1972, "An Investigation of Particle Trajectories in Two-Phase Flow Systems," J. Fluid Mech., **55**(02), pp. 193–208.

[284] Haider, A., and Levenspiel, O., 1989, "Drag Coefficient and Terminal Velocity of Spherical and Nonspherical Particles," Powder Technol., **58**(1), pp. 63–70.

[285] Elghobashi, S., 1994, "On Predicting Particle-Laden Turbulent Flows *," Appl. Sci. Res., **52**, pp. 309–329.

[286] S. Cloete et al., 2010, "Evaluation of a Lagrangian Discrete Phase Modeling Approach for Resolving Cluster Formation in CFB Risers," *7th International Conference on Multiphase Flow*, Tampa, FL.

[287] Arik, M., 2015, "Effect of Chip and Bonding Defects on the Junction Temperatures of High-Brightness Light-Emitting Diodes," Opt. Eng., **44**(11), p. 111305.

[288] Fujimura, K., and Kunugi, T., 1994, "Natural Convection in a Hemispherical Enclosure Heated from Below," **37**(Ii), pp. 1605–1617.

[289] Ranz, W. E., and Marshall, W., 1952, "Evaporation from Drops, Part I," Chem. Eng. Prog., **48**(3), pp. 141–146.

[290] Ranz, W. E., and Marshall, W., 1952, "Evaporation from Drops, Part II," Chem. Eng. Prog., **48**(4), pp. 173–180.

[291] Tamdoğan, E., 2017, "Immersion Cooling of Suspended and Coated Nano-Phosphor Particles for Extending the Limits of Optical Extraction of Light Emitting Diodes," Ozyegin University.

[292] Z. Xu et al., 2018, "Multiscale Dynamic Growth and Energy Transport of Droplets during Condensation," Langmuir, **34**(30), pp. 9085–9095.

[293] Bachmann, V., Ronda, C., and Meijerink, A., 2009, "Temperature Quenching of Yellow Ce3+ Luminescence in YAG:Ce," Chem. Mater., **126**(9), pp. 2077–2084.

[294] Figliola, R. S., and Beasley, D. E., 2001, "Theory and Design for Mechanical Measurements."

[295] Moffat, R. J., 1988, "Describing the Uncertainties in Experimental Results," Exp. Therm. fluid Sci., **1**(1), pp. 3–17.

LIST OF PUBLICATIONS

No	Title	Conference /Journal Name	Status	Date
1	Light Aided Millimetric Bubble Trapping	Nature Communications	Submitted	2022
2	Machine Learning for Junction Temperature Prediction of High Power WLEDs	Micromachines	Under Progress	2022
3	High Brightness Illumination Based on Laser Light Diffusion With Mie Scattering	ASME International Electronic Packaging Technical Conference and Exhibition (InterPACK 2022)	Accepted	2022
4	A Critical Review on the Junction Temperature Measurement of Light Emitting Diodes	ECS Solid State Lighting and Technology	Under Review	2022
5	Discrete Phase Analysis of Self Heating Particles Over An Immersion Liquid Cooled High Power Blue LED with Suspended Phosphor Particles	Journal of Heat Transfer	Under Review	2022
6	Dynamic Analysis of Temperature Sensitivity of LEDs and Laser Diodes	Journal of Applied Physics	Under Progress	2022
7	Package Level Immersion Cooling for Light Emitting Diodes	Journal of Heat and Mass Transfer	Published	2022
8	Optical And Thermal Analysis of Secondary Optics In Light Emitting Diodes' Packaging: Analysis Of MR16 Lamp	8th International Conference on Heat Transfer, Fluid Mechanics and Thermodynamics (Eurotherm)	Published	2021
9	Thermal and Optical Characterization of White and Blue Multi-Chip LED Light Engines	20th IEEE Intersociety Conference on Thermal and Thermomechanical Phenomena in Electronic Systems (ITherm)	Published	2021
10	Package Level Thermal Analysis of White Light-emitting Diodes Based on Local Phosphor Particle Opto-thermal Behavior	LED Professional, May/June 2021	Published	2021
11	Particle based investigation of self-heating effect of phosphor particles in phosphor converted light emitting diodes	Journal of Luminescence	Published	2021
12	Enhanced Thermal Performance of High Flux LED Systems with Two-Phase Immersion Cooling	19th IEEE Intersociety Conference on Thermal and Thermomechanical Phenomena in Electronic Systems (ITherm)	Published	2020

VITA

Ceren Cengiz **Research Areas** Thermal characterization of high-flux LED and LD systems. CFD and experimental analysis for two phase cooling of immersed Pc-WLEDs. Particle based investigations of phosphor to improve optothermal performance of LEDs and LDs. **M.Sc.** Ozyegin University, 2022 **B. Sc. Graduate** Ozyegin University, 2019	*Ceren Cengiz obtained her B.Sc. in Mechanical Engineering from Ozyegin University in 2019. Currently, she is pursuing the M.Sc. degree at Ozyegin University, focusing on thermal management and performance improvements of photonic devices.* *During her studies, she used experimental, theoretical, and computational research methods actively in Energy and Optical Laboratories. She was funded as a research assistant by the Scientific and Technological Research Council of Turkey (TÜBİTAK) under the contract number of 121F134. In addition to research assistantship, she worked as teaching assistant for Heat Transfer, Advanced Heat Transfer, Thermodynamics and Thermal System Design Courses at Ozyegin University.* *At the end of her study, 6 journals (2 published, 3 under review, 1 submitted), 4 conference (3 published, 1 accepted) papers, 1 article for LED Professional Review and 1 patent (pending) have been served to the literature.*